An elastic-plastic interface constitutive model for combined normal and shear loading: application to adhesively bonded joints

by

Mary Catherine Cookson

B.S. Mechanical Engineering
University of Maine (2004)

Submitted to the Department of Mechanical Engineering
in partial fulfillment of the requirements for the degree of

Master of Science

at the

Massachusetts Institute of Technology

September 2010

Author .....
Department of Mechanical Engineering
July 27, 2010

Certified by .....
Lallit Anand
Professor of Mechanical Engineering
Thesis Supervisor

Accepted by .....
David E. Hardt
Chairman, Department Committee on Graduate Students

This work is sponsored by the Department of the Air Force under Air Force contract #FA8721-05-0002. Opinions, interpretations, conclusions and recommendations are those of the author and are not necessarily endorsed by the United States Government.

An elastic-plastic interface constitutive model for combined normal and shear loading: application to adhesively bonded joints

by
Mary Catherine Cookson

Submitted to the Department of Mechanical Engineering
on July 27, 2010, in partial fulfillment of the
requirements for the degree of
Master of Science

Abstract

The behavior of mechanical adhesive interfaces when subjected to a variety of separation and slide loading modes, strain rates, and thermal conditions are of interest in many technical areas. An elastic-plastic constitutive model for adhesive interfaces subjected to combined normal and shear loading has been developed and numerically implemented in a finite element software package. The traction-separation behavior is defined for the normal and shear mechanisms and a displacement jump angle is found to drive the behavior of the initial strength values, as well as the critical and failure displacement jumps of the separate mechanisms that are used to define the model. A set of calibration experiments are performed to fully define an aluminum/adhesive/aluminum system subjected to five different combined loading angles. Tension and shear tests on the aluminum/adhesive/aluminum system at three different rates are used to determine the sensitivity of the adhesive interface to strain rate. The capability of the constitutive model is then explored for the geometry of bonded curvilinear blocks at different loading angles and for a notched four point bend geometry. In addition, a rate dependent elastic-plastic interface constitutive model for combined normal and shear loading is presented, and an initial calibration of inelastic strain rate sensitivity parameters are found.

Thesis Supervisor: Lallit Anand
Title: Professor of Mechanical Engineering

Acknowledgments

I would like to acknowledge my research advisor Professor Lallit Anand for his guidance throughout my studies. Thank you to the MIT Impact and Crash Worthiness Laboratory, specifically Professor Wierzbicki, Carey Walters and Allison Beese for their assistance and generosity in allowing me to conduct my calibration experiments on their biaxial testing apparatus. I would like to acknowledge Professor Boyce's research laboratory for the use of their Zwick testing machine and Pierce Hayward for overall laboratory assistance and instruction. Many thanks to Ray Hardin for his help in all areas and the many things he does to make the experience at MIT better for all solid mechanics students. Also, thank you to the entire MIT Mechanical Engineering graduate office, specifically Leslie Regan, Joan Kravit, Una Sheehan, and Marie Pommet. Thank you to my officemates, Matteo Salvetti and Deepti Tewari, for their help and company. Final technical and personal thanks to my fellow graduate students: Shawn Chester, David Henann, Kaspar Loeffel, Vikas Srivastava, and Claudio Di Leo. Thank you for helping me along my way, but more importantly for your friendship.

My degree studies would not have been possible without the fellowship provided by the MIT Lincoln Laboratory Scholars Program. Specifically, I would like to thank Dr. William Keicher, Ken Estabrook, Susan Abert, and all other LSP committee members and administrators; Dr. Bob Davis and Dr. Steve Forman for their scholars program recommendations; and Dr. Michael Languirand, Dr. Jeffery Mendenhall, and Mark Padula for their support and encouragement throughout. I need to acknowledge all the help I've received from former LSP members Dr. Jeffrey Palmer and Brian Julian, and colleagues Anne Grover Vogel and Saunak Shah. Thank you to John Sultana for his mentorship and for challenging me further. I am also in deep debt to my great mentor and friend Ken Wreghitt for his weekly check in, constant support, and genuine interest in any problems I faced throughout my research.

Personally, I want to acknowledge all my friends and my very large family. Thank you to my siblings and their families: Megan, David, Lyla, Michelle, Moe, Monica, and Marc. Thank you for the support you've given me the last couple of years with all the emails and phone calls; I know you've been with me. An enormous thank you is reserved for my parents, Marc and Martha Girard, for their loving support. To my father for his example in perseverance and truth, and to my mother for her instruction in belief, her inspiration, and uncompromising love. And finally, I can only "begin" to thank my husband, Jason, for all his sacrifices. I am confident this thesis would never have been finished without him, nor would I ever have had the courage to start this journey. Thank you for helping me to carry on.

Contents

List of Figures

List of Tables

Chapter 1

Introduction

The breadth and depth of the influence of interface mechanics can not be underestimated. Mechanical interfaces are seen in a variety of areas and at a variety of scales: biological applications at the boundaries of naturally occurring composite structures such as nacre, in ancient methods of brick and mortar construction, and at grain boundaries of polycrystalline materials with grain sizes of 100 nm. The scope can be narrowed to mechanical adhesive interfaces that are seen in a variety of current technical applications. For example, printed circuit boards are populated with electronic components that are often adhesively bonded and soldered in place as a method of attachment. Structural joints in the automotive, aeronautical, and aerospace applications commonly employ adhesive interfaces to bridge the gap between a composite or a polymeric material and a metallic material. The behavior of the adhesive interface when subjected to combined normal and shear loading, as well as the rate dependent behavior of the adhesive interface is of great importance.

The failure of adhesives has been treated for many years as a fracture mechanics problem, beginning with the development of the cohesive zone model by Barenblatt [1]. This model is a simplified version of Dugdale's [2] strip yield model developed for elastic fracture in thin metal sheets, and descriptions of these models can be found in a literature review in Appendix A. The interface traction-separation relation of the cohesive zone model includes a cohesive strength material property and a cohesive work-to-fracture property. Crack initiation and progression occurs by the decay of interface tractions. The cohesive zone model does not need macroscopic fracture criteria of $K_I = K_{IC}$ or $J_I = J_{IC}$, based on elastic or elastic-plastic analysis, because the traction-separation relation contains material strength, toughness, crack nucleation and propagation parameters.

There are very few interface models that apply the cohesive zone model to capture the elastic, as well as the inelastic response of the interface. This is done by Tvergaard and Hutchinson [3, 4] and Su et al. [5], who both in addition to incorporating inelastic behavior define constitutive models that combine the deformation in the shear and normal mechanisms in a simplification. The framework of Su et al. is limited to a rate independent constitutive

model and the experimental calibration of their work is limited only to pure normal and pure shear testing. There is a need to continue to develop a constitutive model that includes elastic and inelastic behavior of the adhesive subjected to combined loading conditions based on a comprehensive experimental approach, as well as investigating possible forms of a rate dependent constitutive model.

An elastic-plastic interface constitutive model for combined normal and shear loading and its application to adhesively bonded joints is presented in the current study. This work is unique in truly attempting to quantify the combined normal and shear loading response of an adhesive interface through a series of combined loading experiments. A traction-separation law is used to describe the adhesive interfacial behavior with a calculated displacement jump angle defining specific constitutive functions for the initial strength in the normal and shear mechanisms, as well as the critical displacement jumps used to define the model. In addition, a rate dependent elastic-plastic constitutive model for combined normal and shear loading is presented, which utilizes a power law model to capture the rate dependent behavior of the polymeric adhesive.

First, a battery of experiments performed for an adhesive interface subjected to different applied angles of normal and shear loading through the use of a biaxial testing apparatus are described in Chapter 2. The butt joint specimen preparation procedure is described in detail. In addition, details of the biaxial testing apparatus employed to execute the experiments are included. Finally, the results of the experiments are presented.

The rate independent constitutive model of the current study for an interface subjected to combined normal and shear loading is presented in Chapter 3. A traction-separation behavior is defined for the two individual loading mechanism and a displacement jump angle is found to drive the behavior of the initial strength values, as well as the critical and failure displacement jumps of the separate mechanisms that are used to define the model. The phenomenological material parameters required for the calibration of the constitutive model are also discussed and defined.

Using the results of the experiments on adhesively bonded joints, the interface constitutive model is tuned in Chapter 4. The details of the material parameters required for specific forms of the combined loading constitutive equations are presented. Furthermore, the constitutive model is implemented in a user subroutine within ABAQUS/Explicit, a commercially available finite element package.

The application of the adhesive interface phenomenological constitutive model is explored in Chapter 5. A curvilinear block geometry is monotonically loaded at two different applied angles to explore the key areas of the study. The macroscopic load versus displacement jump for the two different applied angles of combined loading have been successfully predicted. Also, a small scale notched four point bend geometry is examined, and the experimental results and numerical predictions are presented and discussed. The vertical load-vertical displacement of the notched four point bend specimen under a constant displacement rate has been fairly well predicted.

In addition, a rate dependent constitutive model for an interface subjected to combined loading is presented in Chapter 6. The rate dependent power law model parameters are

found for the experimental results of the adhesive joints tested at three rates each in the normal direction and the shear direction (Chapter 7).

Lastly, a brief summary of findings and recommended future work is presented in Chapter 8.

Chapter 2

Experiments on Adhesive Joints

In order to understand the behavior of the adhesive interface subjected to combined normal and shear loading, a method must be found to experimentally apply such loading. A biaxial testing apparatus with a horizontal and vertical actuator is chosen, as it will provide the ideal testing method for this requirement. The following section includes the experimental procedure and details of the experiments that were performed to understand the behavior of the adhesive interface subjected to combined normal and shear loading. In addition, experiments are performed on the adhesive interface in the normal and shear configurations at various rates. The specimen preparation details are described first, followed by the details of the testing apparatus, and finally a presentation of the experimental results.

2.1 Biaxial Specimen Preparation

The biaxial testing apparatus requires rectangular cross section butt joints to be used. The specimen is comprised of two adherends joined by a layer of adhesive. A schematic of the specimen can be seen in Figure 2-1, and the process to prepare the adherends and the adhesive are described below in Section 2.1.1 and Section 2.1.2. The adherends and adhesive are then cured and prepared for testing, which is documented in Section 2.1.3 and Section 2.1.4.

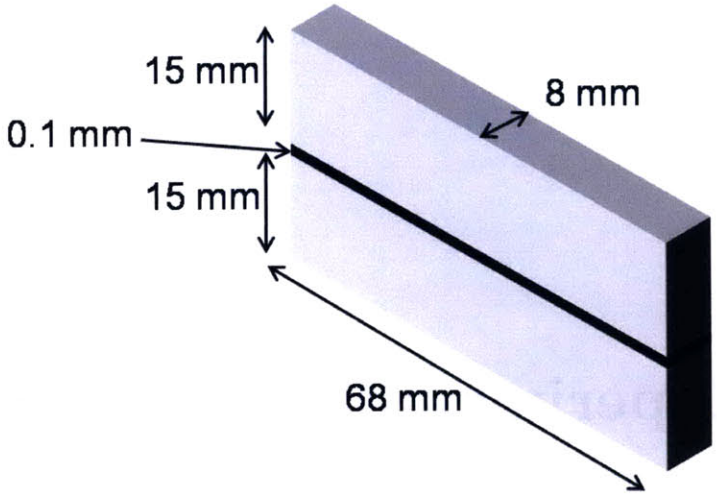

Figure 2-1: Graphic of prepared specimen

2.1.1 Adherend Preparation

The two adherends are fabricated from bare 6061-T6 Aluminum: 68 mm long, 15 mm wide, and 8 mm thick. They are machined with sharp corners to achieve a good alignment during bonding.

A photo of a prepared biaxial specimen used for calibration experiments can be seen in Figure 2-2.

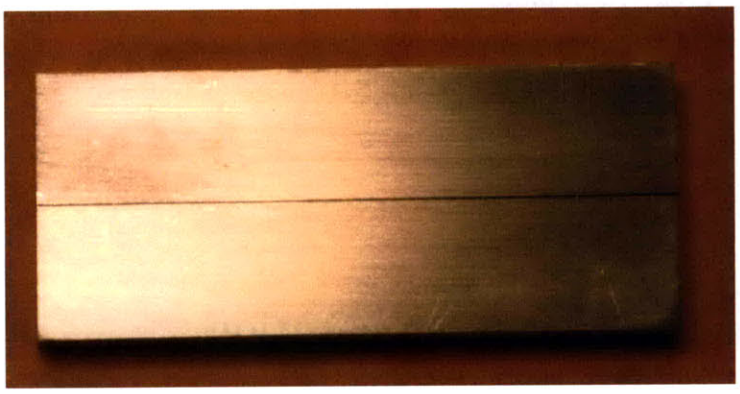

Figure 2-2: Photo of specimen after excess epoxy removal

Per the manufacturers recommendation [6] and ASTM D2651-01 [7], the surface area for bonding (68 mm x 8 mm) on each adherend is abraded by hand with 240 grit emery paper in a random pattern. The adherends are rinsed with water and dried. Length, width, and

height measurements are taken with a digital caliper and recorded. The adherends are then repeatedly wiped with acetone and high absorbency, low particle generating, composite clean room wipes until no residue appears on the wipe itself. Isopropyl alcohol is then used to clean all sides of the adherends. It is important to clean first with the acetone solvent to degrease the material and then the isopropyl alcohol to finalize. It is also important to allow the isopropyl alcohol to fully vaporize (approximately 15 minutes) from the aluminum before attempting to apply any adhesive.

In order to establish the chosen bond thickness of 0.1 mm (0.004 inch), two wires of that diameter are chosen for insertion into the bond. These wires are first wiped with isopropyl alcohol and then taped in place approximately 8 mm from each end of the lower adherend. The wires are taped on the front side of the specimen and bent over onto the bonding surface. The remaining end is trimmed with a razor to allow for a flush back surface to be used for alignment during curing. Next the adhesive is prepared for bonding.

2.1.2 Adhesive Preparation

The chosen epoxy paste adhesive, Hysol®EA 9361, is a two part component adhesive, and the manufacturers recommended mix ratio of 100 parts by weight of Part A to 140 parts of Part B is used [8]. The two components of the adhesive were stored and mixed at room temperature throughout all experiments. A mixed batch is prepared to yield 5 grams total, which produces more than what is required to build two cured specimens while allowing for a large enough volume to ensure a good mixing ratio. Once completely mixed, the adhesive is degassed in a vacuum chamber according to the following procedure: vacuum pulled 2 minutes, vacuum broken, vacuum pulled 2 minutes, vacuum broken, vacuum pulled 10 minutes, vacuum broken. Air bubbles are commonly introduced into the adhesive during the mixing process and degassing helps to decrease the number of entrapped air bubbles creating a more homogenous bond.

The prepared adhesive is then applied to both clean adherends with a metal spatula. The adherends are then placed on their sides (68 mm x 15 mm side) within a steel machinist clamp. They are aligned to each other via the bottom surface of the clamp and an external vertical registering block. A photo of a clamped specimen can be seen in Figure 2-3.

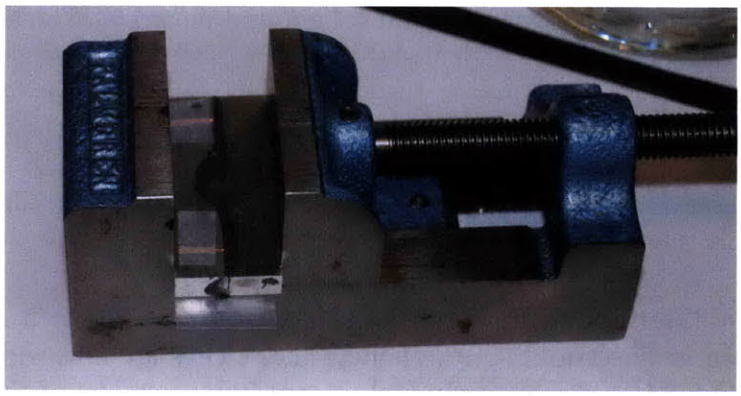

Figure 2-3: Photo of butt joint specimen in bonding clamp

In order to preload the bond and ensure the bond line is being repeatedly established, an experimentally found load of 20 N is applied to the handle of the clamp. The specimen is now ready to be cured.

2.1.3 Specimen Curing and Finishing

The aligned and clamped specimens are placed in an oven for heat curing. Per manufacturing directions, the Hysol ®EA 9361 room temperature cure of 5 to 7 days can be accelerated with a 1 hour cure at 82°C. The specimens are heat cured in a Fisher Isotemp Vacuum Oven, Model 281. After a full hour at 82°C, the oven is turned off and allowed to return to room temperature without forced cooling.

After the specimens are cooled, they are removed from the oven and the clamps are removed. A photo of the specimen at this stage can be seen in Figure 2-4. All excess epoxy on the outer surfaces of the bonded specimens is removed, first with a razor blade, and then with 240 grit emory paper. A picture of a cleaned specimen ready for testing can be seen in Figure 2-2.

Figure 2-4: Photo of specimen after epoxy cure

Length, width, and height measurements of the clean specimens are again taken with a digital caliper. In addition, photos of the bond line through a microscope are taken. These photos are taken to ensure the bond line thickness is established with the inserted wire and that the edges of the specimen are as uniform as possible. An example photo of the embedded wire within the bond, taken under 20X magnification, can be seen in Figure 2-5.

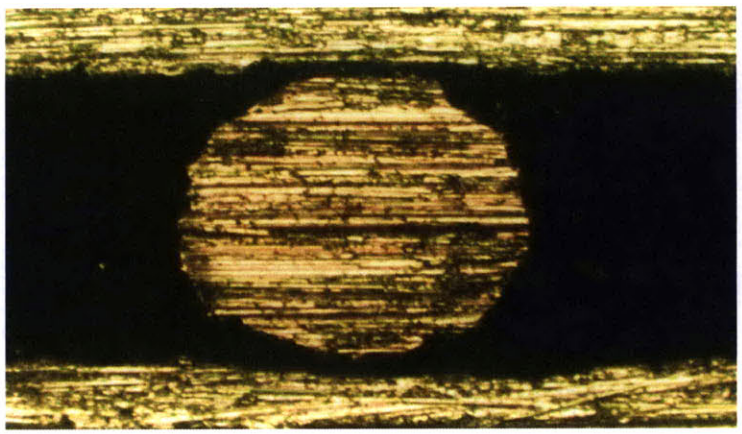

Figure 2-5: Magnified (20X) photo of epoxy bond line with embedded wire

2.1.4 Specimen Preparation for Digital Image Correlation

The last step of preparing the specimens for testing is to apply a spray paint pattern that will be used by the Digital Image Correlation system detailed in Section 2.2.2.

A pattern of black dots on a white background is applied to the area of the specimens that is viewable to the camera. The area of the specimen (approximately 68 mm x 10.1 mm) that will be within the upper and lower grips of the biaxial testing apparatus are taped off.

White matte spray paint is applied to the area, allowed to dry, and then a black matte spray paint is used to create a random black pattern, as seen in Figure 2-6.

Figure 2-6: Specimen spray paint pattern

The specimens are now ready to be tested, and a description of the biaxial testing apparatus and the experimental procedure are described in the next section.

2.2 Experimental Procedure

Displacement controlled experiments are performed on the butt-joint specimens in a variety of applied angles. The following section details the hardware and software used in the execution of testing.

2.2.1 Biaxial Testing Apparatus

A dual actuator hydraulic testing machine [9], courtesy of the Impact and Crashworthiness Test Laboratory at MIT, allows for the determination of the adhesive behavior when subjected to combined loading. Figure 2-7 contains a schematic of the system used.

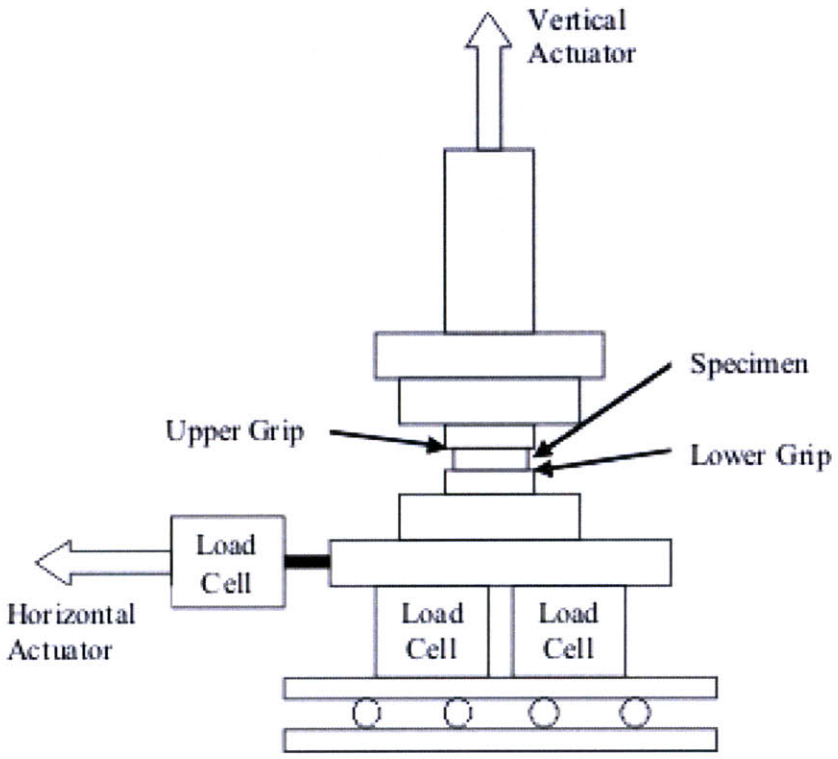

Figure 2-7: Schematic of biaxial testing apparatus

The dual actuator machine consists of a vertical actuator with two 100 kN load cells and a horizontal actuator with a 50 kN load cell. The lower grip of the machine sits on a low friction sliding table that allows for the horizontal movement of the lower assembly. This sliding table is attached to a rod which is then connected to the horizontal actuator through the 50 kN load cell. The specimens are held in the biaxial testing apparatus by an upper and a lower clamp grip. Each clamp grip has four M10 bolts to apply an appropriate gripping pressure on each side of the specimen, which are tightened to 80 Nm with a calibrated torque wrench. The grips had previously been fabricated from high-carbon/high-chromium steel, a photo of which can be seen in Figure 2-8.

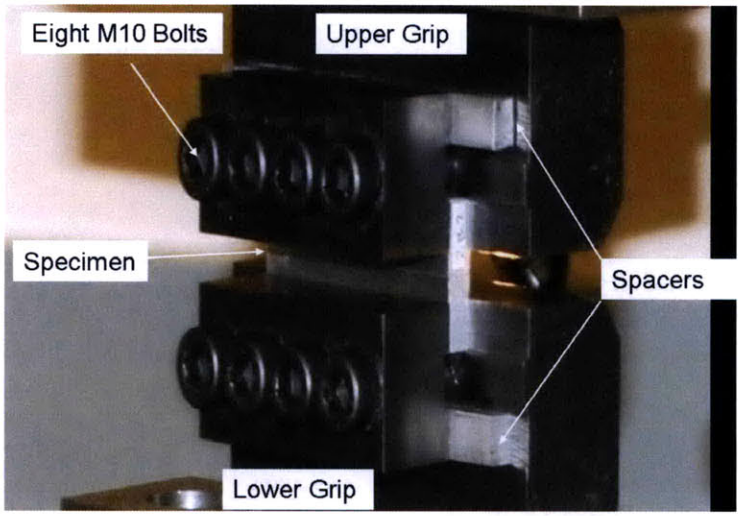

Figure 2-8: Photo of biaxial testing apparatus grips

The hydraulic system can be load and/or displacement controlled and this is achieved with control software (Fast Track, Instron) that allows for the collection of load data as well as actuator displacement data. The method for collection of displacement data for the specimen along the bond line is detailed below in Section 2.2.2.

2.2.2 Optical Displacement Measurement

The displacements across the adhesive interface are measured using a digital image correlation (DIC) system (Correlated Solutions, West Columbia, SC). The digital image camera (QImaging, Retiga 1300i, Fast 1394, with Nikon Nikkor Lens) is positioned on a tripod approximately 0.5 m away. The tripod and camera are leveled and the axis of the camera lens is positioned to be as perpendicular as possible to the flat surface of the gauge section to be photographed. Two fiber-optic lights are positioned to illuminate the gauge area to be captured by the DIC. These testing components can be seen in Figure 2-9 and Figure 2-10.

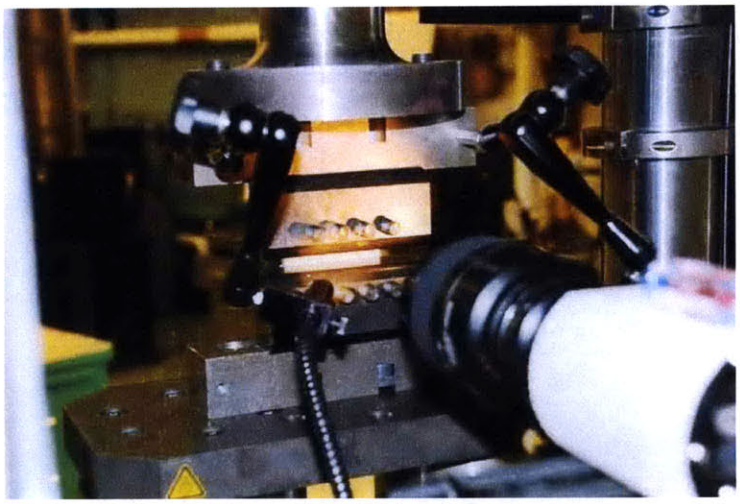

Figure 2-9: Setup of digital image correlation system: camera view

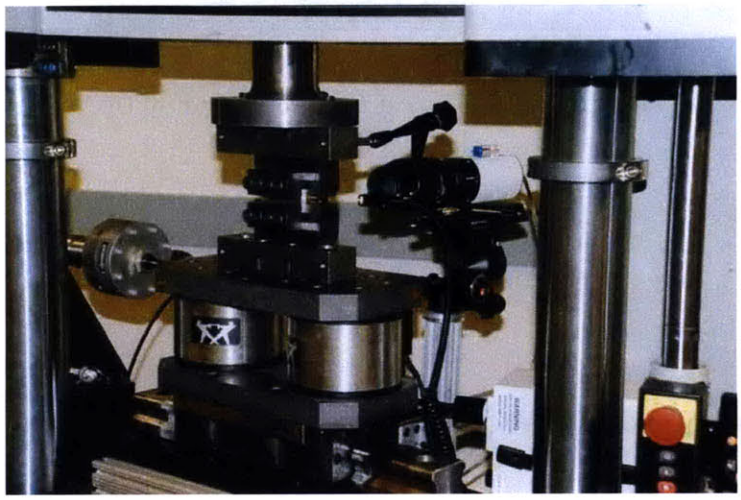

Figure 2-10: Setup of digital image correlation system: operator view

The number of captured images can be varied for any given experiment, but for the experiments described in this chapter a single frame was taken every second. Each digital image is 1300 x 1030 pixels resolution, where the edge length of one pixel is approximately equal to 10 microns. The software Vic-2d (version 4.2) uses a cubic B-spline interpolation algorithm to track the movement of the grayscale within any selected pixel over the course of time, and several points on both the top and bottom of the interface are selected. An extensometer can be drawn across the interface and the algorithm will track the pixel position

of the selected point over the spectrum of "deformed" photos taken. A typical image that is processed by the digital image correlation software can be seen in Figure 2-11.

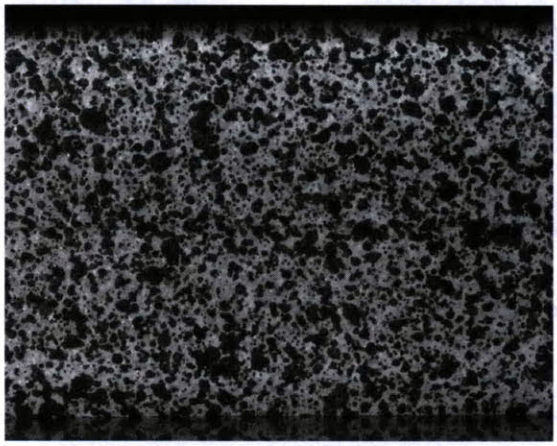

Figure 2-11: Typical image captured by DIC

2.2.3 Experimental Test Matrix

Experiments are performed to understand the behavior of the adhesive interface when subjected to combined loading conditions. Any combination of normal and shear loading on the interface are bounded by the pure loading case of each mode. Normal loading of the interface is achieved with a tensile experiment within the biaxial testing apparatus at a nominal displacement rate of 1 x 10^{-3} mm/s. Secondly, pure and simple shear experiments are performed at the same nominal rate of 1 x 10^{-3} mm/s. Experiments are then performed on a variety of combined loading angles at the interface. The applied angle, θ_A, is calculated as the arc tangent of the ratio of the velocity in the vertical direction at the upper grip to the velocity in the horizontal direction at the lower grip. A schematic of the applied angle is shown in Figure 2-12.

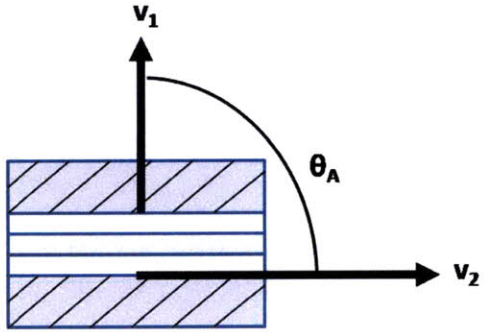

Figure 2-12: Applied angle definition

The nominal applied displacement rates are the rates that were programmed into the controller for all experiments. The actual displacement rates of the specimen at a points right at the upper and lower grip were found from the digital image correlation data. There is some lag in each actuator that provides for the discrepancy. The nominal applied angle (and displacement rates) and the actual applied angle (and displacement rates) are given in Table 2.1. To be clear, the actual applied combined loading angles tested are 7.0°, 10.6°, 22.0°, 34.9°, and 50.4°.

Table 2.1: Combined loading test matrix

Nominal Applied Angle	Nominal Rate (mm/s)	Actual Rate (mm/s)	Actual Applied Angle
10°	$v_1 = 0.174 \times 10^{-3}$ $v_2 = 0.985 \times 10^{-3}$	$v_1 = 0.916 \times 10^{-4}$ $v_2 = 0.743 \times 10^{-3}$	7.0°
15°	$v_1 = 0.259 \times 10^{-3}$ $v_2 = 0.966 \times 10^{-3}$	$v_1 = 0.136 \times 10^{-3}$ $v_2 = 0.728 \times 10^{-3}$	10.6°
30°	$v_1 = 0.5 \times 10^{-3}$ $v_2 = 0.866 \times 10^{-3}$	$v_1 = 0.263 \times 10^{-3}$ $v_2 = 0.653 \times 10^{-3}$	22.0°
45°	$v_1 = 0.707 \times 10^{-3}$ $v_2 = 0.707 \times 10^{-3}$	$v_1 = 0.372 \times 10^{-3}$ $v_2 = 0.533 \times 10^{-3}$	34.9°
60°	$v_1 = 0.866 \times 10^{-3}$ $v_2 = 0.5 \times 10^{-3}$	$v_1 = 0.456 \times 10^{-3}$ $v_2 = 0.377 \times 10^{-3}$	50.4°

The investigation of the response of the adhesive interface subjected to various applied angles will provide traction-separation curves for both the normal and shear mechanisms for each angle.

To understand the rate dependent behavior of the adhesive, tension and simple shear tests are performed for three different rates. The nominal and actual displacement rates tested are shown in Table 2.2 and Table 2.3.

Table 2.2: Rate dependent test matrix: normal loading rates

Nominal Rate (mm/s)	Actual Rate (mm/s)
1×10^{-4}	0.584×10^{-4}
1×10^{-3}	0.527×10^{-3}
1×10^{-2}	0.571×10^{-2}

Table 2.3: Rate dependent test matrix: shear loading rates

Nominal Rate (mm/s)	Actual Rate (mm/s)
1×10^{-3}	0.754×10^{-3}
1×10^{-2}	0.698×10^{-2}
1×10^{-1}	0.717×10^{-1}

2.3 Results of Combined Normal and Shear Loading

The experimental results of the combined normal and shear loading testing is provided in this section. The baseline normal and simple shear experimental results at the nominal displacement rate of 1×10^{-3} mm/s are presented first. Next, the results of all combined loading cases (Table 2.1) are shown. Finally, the normal loading (Table 2.2) and shear loading (Table 2.3) rate dependent results are presented. Note that at least three specimens were tested for each case.

2.3.1 Results of Normal Loading of Adhesive Interface

After the specimen and test preparations, described in Sections 2.1 and 2.2.1 are complete, we perform our experiments. A nominal displacement rate of 1×10^{-3} mm/s is given to the vertical actuator of the biaxial testing apparatus and the displacement is held on the

lower grip. As mentioned previously, this nominal controller displacement rate equates to a displacement rate of 0.527 x 10^{-3} mm/s at the upper grip.

The traction-separation response of the adhesive tested in the normal direction at a rate of 0.527 x 10^{-3} mm/s for three specimens can be seen in Figure 2-13. Note that for this separation rate, a specimen takes approximately 2 minutes to fail. The abscissa of the plot is the normal displacement jump, $\delta^{(1)}$, which experimentally is equal to the vertical displacement of the upper block right above the adhesive minus the vertical displacement of the lower block right below the adhesive. The ordinate of the plot is equal to the normal stress, t_N, which is experimentally equal to the vertical load divided by the adhesive area of approximately 68 mm x 8 mm.

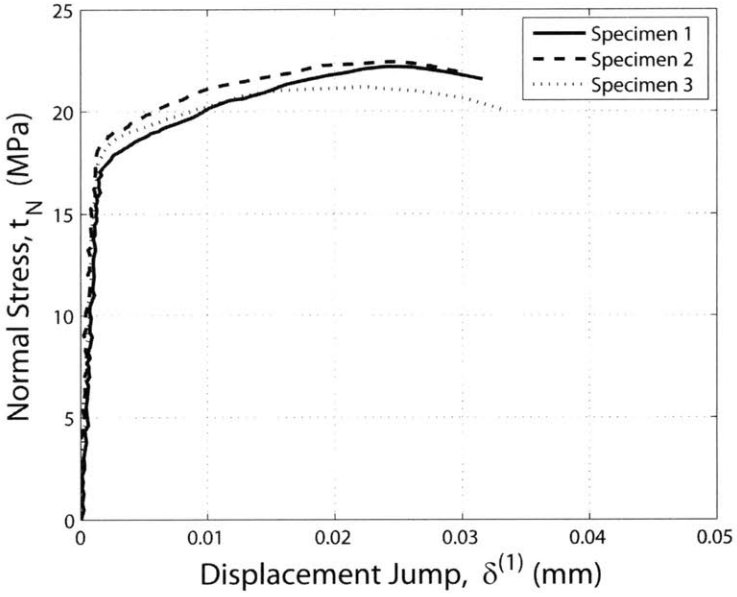

Figure 2-13: Traction-separation behavior of adhesive tested in normal direction

Notice the adhesive is elastic until approximately 18 MPa, at which point it becomes plastic, reaching a peak strength of about 22 MPa. The adhesive then softens slightly and fails suddenly in tension. After failure, adhesive remains on both the upper and lower adherends, which indicates a failure within the adhesive as opposed to a cohesive or bonding failure at the aluminum interface.

2.3.2 Results of Shear Loading of Adhesive Interface

The results of the experiments in pure shear and simple shear are discussed in this section.

Simple Shear

The simple shear experiment is performed by specifying a nominal displacement rate to the horizontal actuator of 1 x 10^{-3} mm/s. From experiments, however it was determined to be an applied displacement rate at the lower grip of 0.754 x 10^{-3} mm/s. The vertical actuator is held fixed in position, while the horizontal actuator moves the lower adherend only (the upper adherend is held fixed in position).

The traction-separation response of the adhesive tested in simple shear at a rate of 0.754 x 10^{-3} mm/s for three specimens can be seen in Figure 2-14. For this case each specimen takes approximately 12 minutes to fail. The abscissa of Figure 2-14 is the shear displacement jump, $\delta^{(2)}$, which experimentally is equal to the horizontal displacement of the lower adherend at the adhesive interface minus the horizontal displacement of the upper adherend at the adhesive interface. The ordinate of Figure 2-14 is equal to the shear stress, $\bar{\tau}$, which is experimentally equal to the horizontal load divided by the adhesive area of approximately 68 mm x 8 mm.

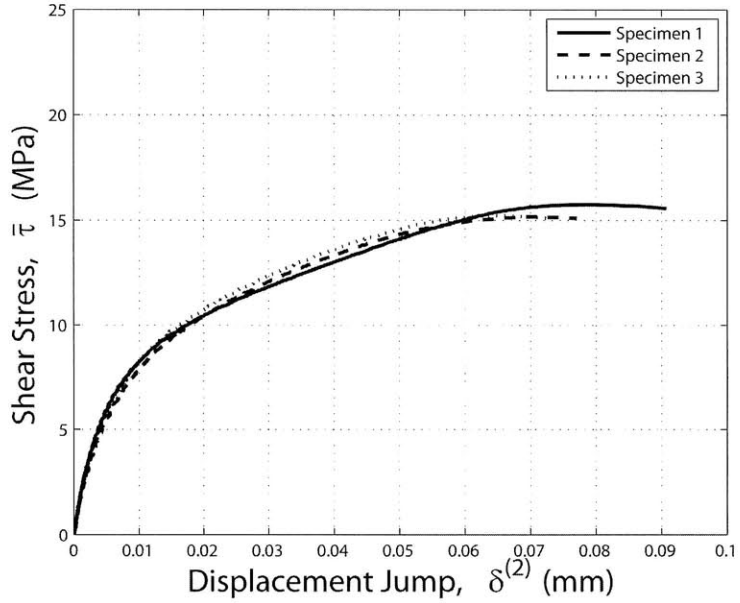

Figure 2-14: Traction-separation behavior of adhesive tested in simple shear

The simple shear traction-separation curve indicates a very low yield strength of approximately 1-2 MPa before the adhesive starts to noticeably harden. The adhesive hardens to approximately 15 MPa, before a small amount of softening occurs and the interface fails. Again, the mode of failure detected in this experiment is found to be a very sudden loss of strength and the horizontal load drops quickly to zero.

Pure Shear

The pure shear test is performed by specifying a nominal displacement rate to the horizontal actuator of 1 x 10^{-3} mm/s. From experiments, it was determined to be an actual applied displacement rate of 0.754 x 10^{-3} mm/s at the lower grip. Again, the horizontal actuator moves the lower adherend only, while keeping the total vertical force equal to zero. The pure shear experiment is performed to compare directly to the simple shear response of the adhesive. The traction-separation behavior of the adhesive in pure shear for three different specimens is shown in Figure 2-15.

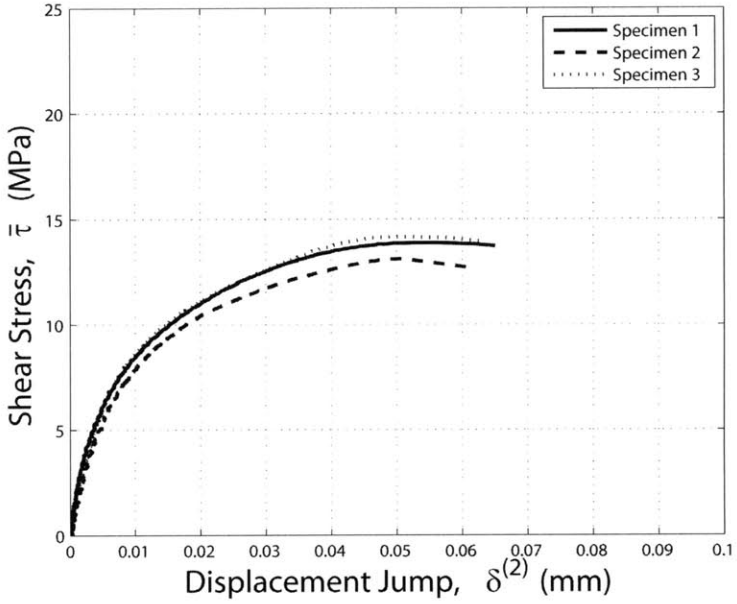

Figure 2-15: Traction-separation behavior of adhesive tested in pure shear

Notice that the shear strength found in both the pure shear experiment and simple shear experiment are nearly identical at about 14 MPa. Here however, that the failure of the adhesive occurs around 0.06 mm compared to the 0.08 mm seen in the simple shear experiment. The simple shear results will be used for the calibration of the combined loading model of the adhesive. All combined loading experiments were performed using displacement control.

2.3.3 Results of Combined Loading of Adhesive Interface

The results of all the combined loading experiments are contained within this section, and as previously mentioned all load cases were tested on at least three specimens. The results of the three specimens, prepared per Section 2.1, are shown for the five applied angles. The normal traction-separation and the shear traction-separation response of each experiment

listed in Table 2.1 are presented below. The actual applied angles that were tested were 7.0°, 10.6°, 22.0°, 34.9°, and 50.4°.

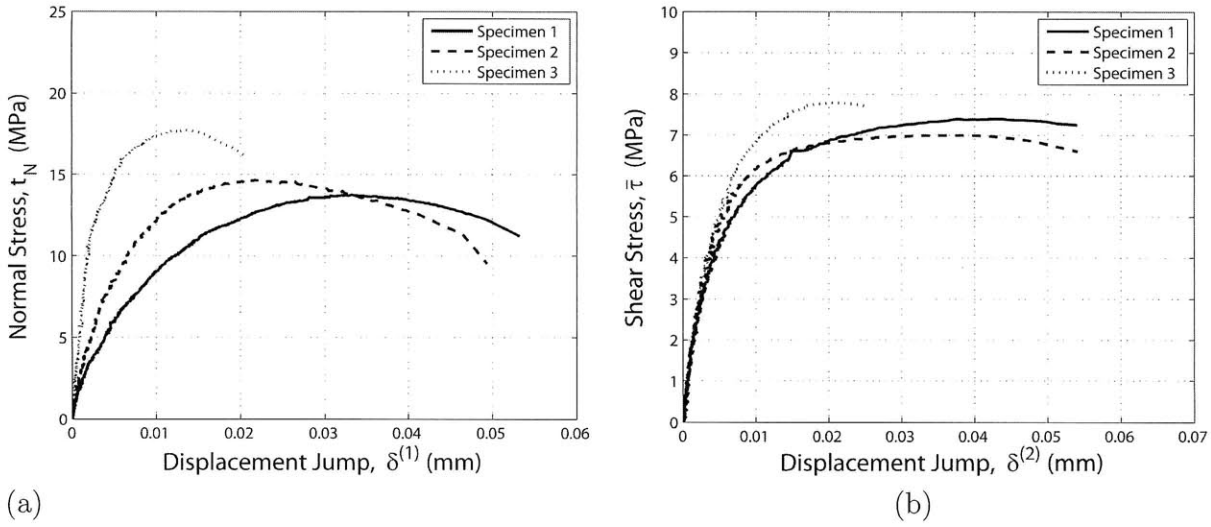

Figure 2-16: Traction-separation behavior of adhesive tested at 7.0° (a) normal and (b) shear

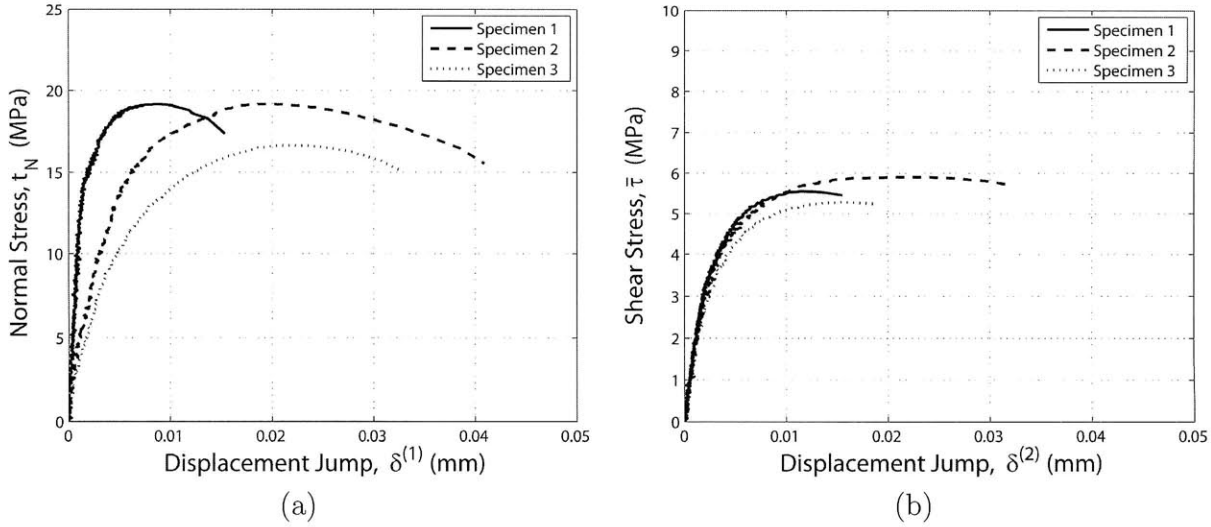

Figure 2-17: Traction-separation behavior of adhesive tested at 10.6° (a) normal and (b) shear

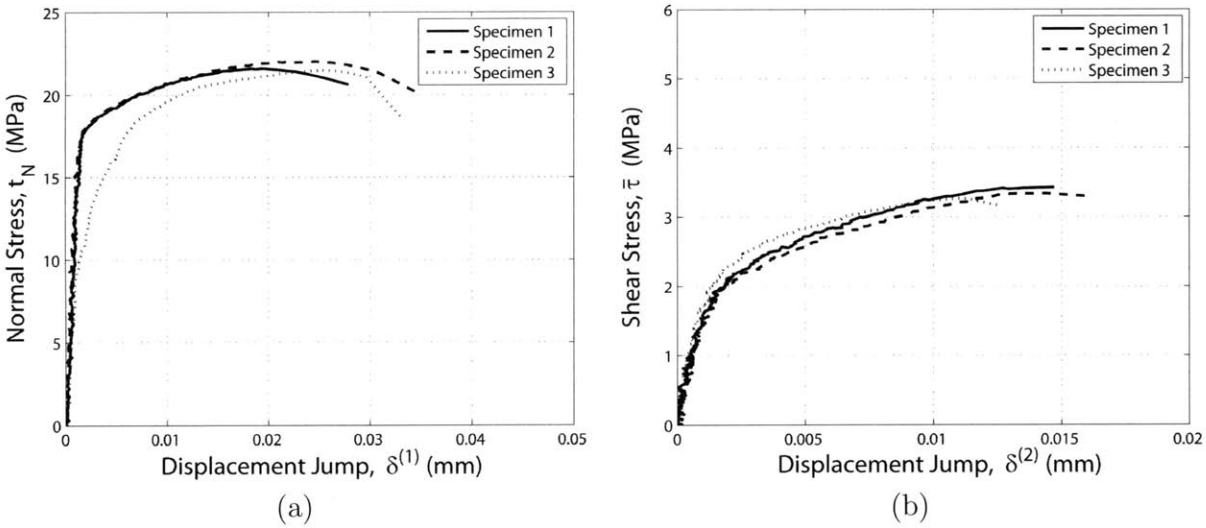

Figure 2-18: Traction-separation behavior of adhesive tested at 22.0° (a) normal and (b) shear

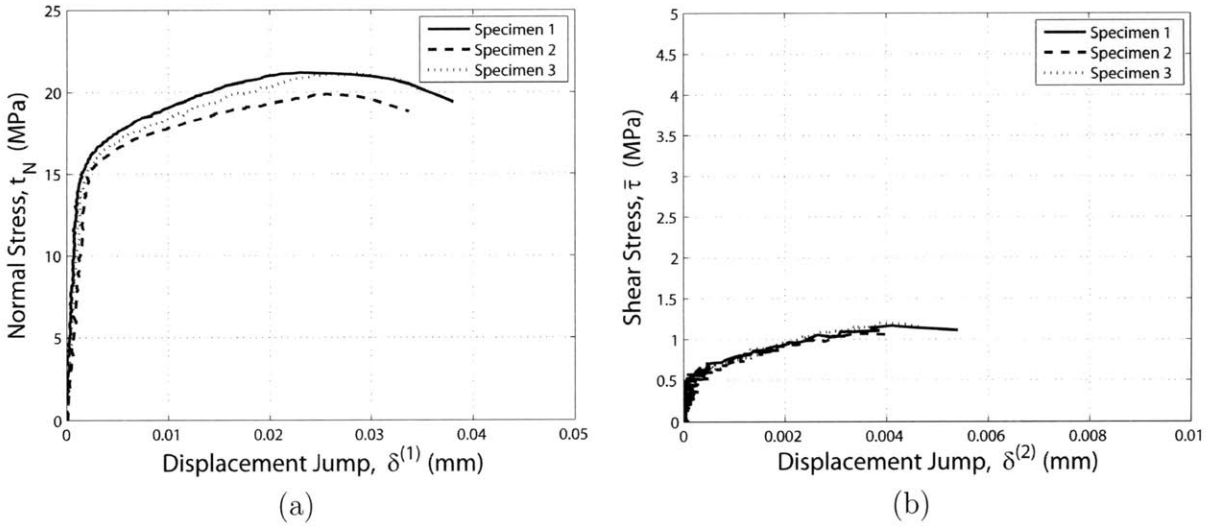

Figure 2-19: Traction-separation behavior of adhesive tested at 34.9° (a) normal and (b) shear

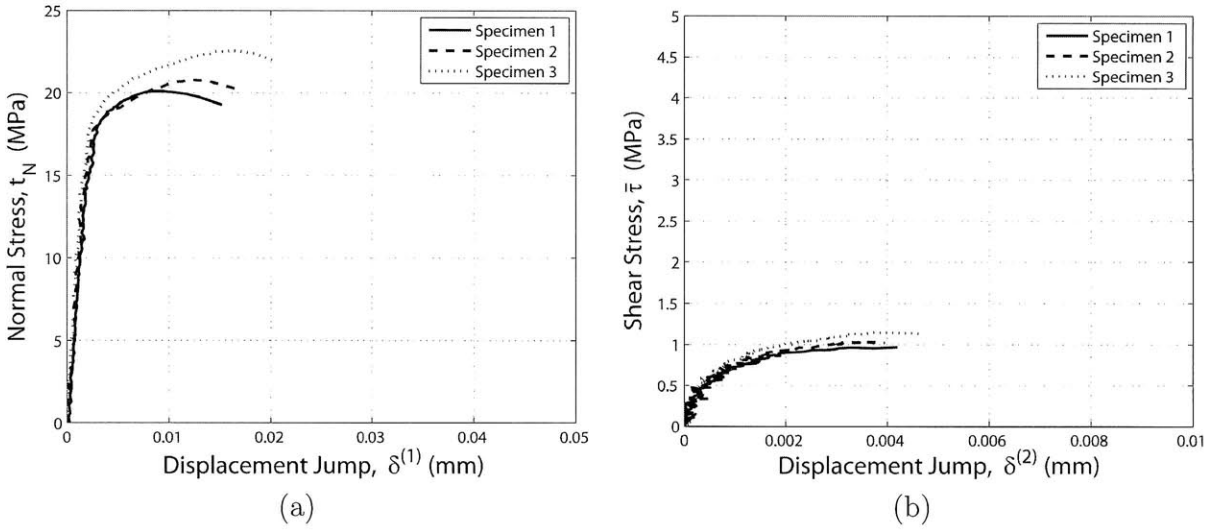

Figure 2-20: Traction-separation behavior of adhesive tested at 50.4° (a) normal and (b) shear

From these results one can see that the experimental spread in the traction-separation response for the multiple specimens tested increased as the applied angle decreased. In other words, there is more variability in the normal and shear traction-separation response of the three specimens shown for the 7.0° and 10.6° cases than the three specimens tested at 34.9° and 50.4°.

The results of the testing indicated that as the applied angle increased, the shear strength of the adhesive decreased. For example, an average peak shear strength of about 7 MPa can be seen for the 7.0° applied angle, while an average peak shear strength of about 1 MPa can be seen for the 50.4° applied angle experiment. Also, as applied angle increased, the failure shear displacement jump decreased. For example, the average failure displacement jump in shear for the 7.0° applied angle is about 0.05 mm, while an average failure displacement jump of only 0.004 mm can be seen for the 50.4° applied angle. In addition, the normal strength of the adhesive is approximately equal to 22 MPa for the applied angles of 22.0°, 34.9°, and 50.4° and it starts to noticeably decrease for the smaller applied angles of 7.0° and 10.6°.

2.4 Results of Rate Dependent Behavior of Adhesive Interface

As mentioned in Section 2.2.3, the normal and simple shear testing of the adhesive interface at different rates has been completed and described below. Rate dependent tests are performed using the biaxial testing apparatus and using the same specimen and test preparation described in Section 2.1 and Section 2.2.1.

2.4.1 Normal Rate Dependent Behavior

The adhesive has been tested in the normal direction at three rates: 0.584 x 10^{-4} mm/s, 0.527 x 10^{-3} mm/s, and 0.571 x 10^{-2} mm/s, where each rate is approximately one magnitude apart. The traction-separation response of the adhesive subjected to normal loading at three different rates can be seen in Figure 2-21. Notice that the peak normal strength increases by approximately 23 percent with each magnitude increase in rate: 17 MPa, 22 MPa, and 27 MPa. It is also important to note the dependence on rate seen in the critical (and failure) displacement jump. The value of critical displacement jump increases by approximately 45 percent with each magnitude increase in rate: 0.013 mm, 0.027 mm, and 0.038 mm.

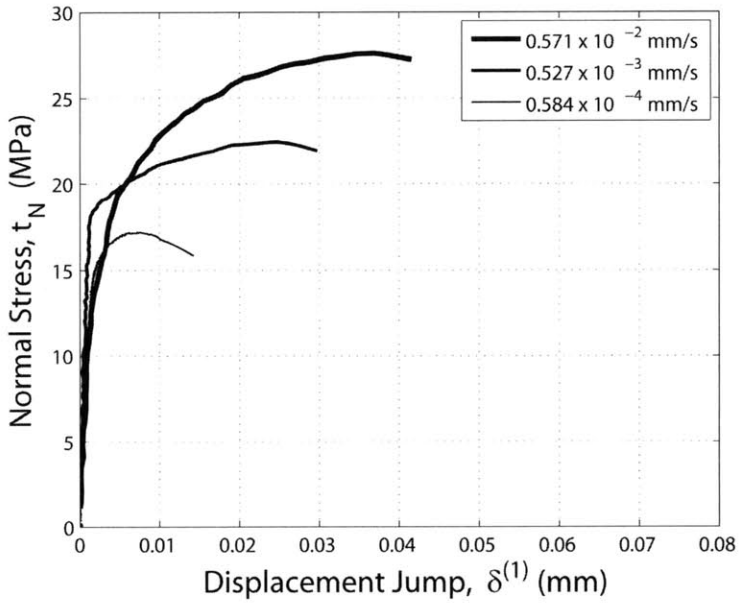

Figure 2-21: Rate dependent traction-separation behavior of adhesive tested in normal direction

2.4.2 Shear Rate Dependent Behavior

Finally, the adhesive has been tested in the tangential or shear direction at three rates: 0.754 x 10^{-3} mm/s, 0.698 x 10^{-2} mm/s, and 0.717 x 10^{-1} mm/s, where each rate again is approximately one magnitude apart. The traction-separation response of the adhesive subjected to shear loading at three different rates can be seen in Figure 2-22. Note that the peak shear strength increases by approximately 27 percent with each magnitude increase in rate: 15 MPa, 19 MPa, and 23 MPa. The critical displacement jump in the shear direction, however, did not exhibit any significant rate dependency.

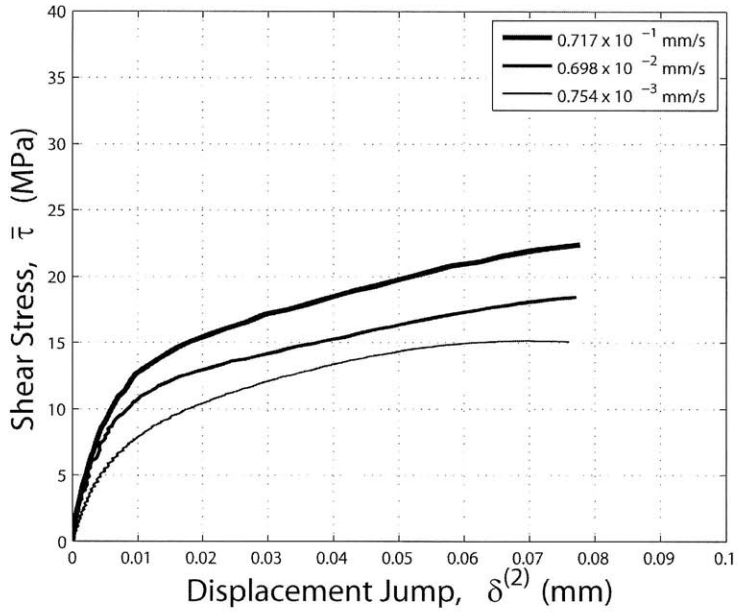

Figure 2-22: Rate dependent traction-separation behavior of adhesive tested in shear direction

2.5 Chapter Summary

This section has presented the key details of the experimental procedure and specimen preparations that are taken in order to gather a large data set of experimental results for an adhesive interface subjected to combined normal and shear loading. In addition, the experimental results of the adhesive interface tested at three rates in the normal direction and three rates in the shear direction were presented.

The behavior of adhesive interfaces holds many opportunities to develop appropriate test measures, calibrate cohesive parameters, and to build in the area of numerical capabilities. The current study presented herein attempts to better understand the behavior of an adhesive interface subjected to combined loading of opening and sliding mechanisms. The continuum-level phenomenological rate independent interface constitutive model of the current study is outlined in Chapter 3 and will incorporate the behavior of the adhesive subjected to combined normal and shear loading through separate plastic displacement jumps of the two separate mechanisms. A rate dependent phenomenological interface constitutive model is presented in Chapter 6 which will account for the combined loading as well as the rate dependent behavior often seen in polymeric adhesives.

Chapter 3

Rate Independent Interface Constitutive Model

The following chapter details the rate independent interface constitutive model used for the current study. It draws from the elastic-plastic model of Su et al.[5], with a key difference being in the calculation of the displacement jump angle at the interface to account for combined normal and shear loading.

3.1 Interface Definitions

Our adhesive system is comprised of two bodies $\mathcal{B}^+$ and $\mathcal{B}^-$ separated by an interface $\mathcal{I}$ illustrated in Figure 3-1.

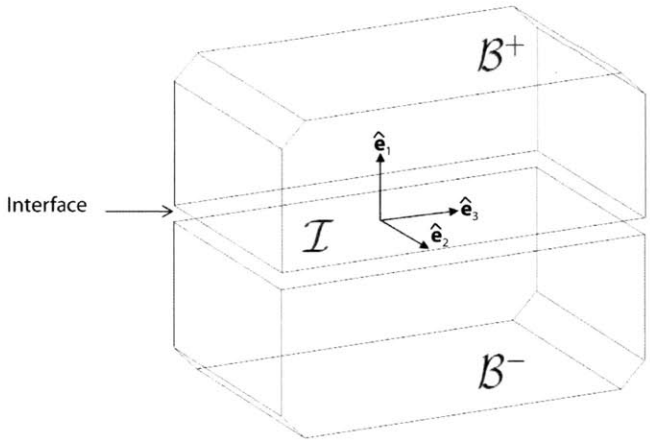

Figure 3-1: Illustration of adhesive system

Let $\{\hat{\mathbf{e}}_1, \hat{\mathbf{e}}_2, \hat{\mathbf{e}}_3\}$ be an orthonormal triad, with $\hat{\mathbf{e}}_1$ aligned with the normal $\mathbf{n}$ to the interface, and $\{\hat{\mathbf{e}}_2, \hat{\mathbf{e}}_3\}$ in the tangent plane at the point of the interface under consideration.

At the point under consideration, we let $\boldsymbol{\delta} = \mathbf{u}^+ - \mathbf{u}^-$ denote the displacement jump across the interface as the difference between the displacement of a point on the interface of the upper body, $\mathcal{B}^+$, and a point on the interface of the lower body, $\mathcal{B}^-$.

The displacement jump is assumed to be additively decomposed into elastic, $\boldsymbol{\delta}^e$, and plastic, $\boldsymbol{\delta}^p$, parts:

$$\boldsymbol{\delta} = \boldsymbol{\delta}^e + \boldsymbol{\delta}^p. \tag{3.1}$$

The power-conjugate traction, $\mathbf{t}$, acting on the interface combines with the rate of change of displacement jump yielding the power per unit area of the interface in the reference configuration, $\mathbf{t} \cdot \dot{\boldsymbol{\delta}}$. This too can be decomposed into

$$\mathbf{t} \cdot \dot{\boldsymbol{\delta}} = \mathbf{t} \cdot \dot{\boldsymbol{\delta}}^e + \mathbf{t} \cdot \dot{\boldsymbol{\delta}}^p. \tag{3.2}$$

3.2 Free Energy of the Interface

A free-energy per unit surface area in the reference configuration is denoted by φ. A purely mechanical theory based on the following local energy imbalance that represents the first two laws of thermodynamics under isothermal conditions is considered, where

$$\dot{\varphi} \leq \mathbf{t} \cdot \dot{\boldsymbol{\delta}}. \tag{3.3}$$

Substituting to account for the elastic and plastic contributions,

$$\dot{\varphi} \leq \mathbf{t} \cdot \dot{\boldsymbol{\delta}}^e + \mathbf{t} \cdot \dot{\boldsymbol{\delta}}^p. \tag{3.4}$$

This field equals the dissipation per unit area, Γ,

$$\Gamma = \mathbf{t} \cdot \dot{\boldsymbol{\delta}}^e + \mathbf{t} \cdot \dot{\boldsymbol{\delta}}^p - \dot{\varphi} \geq 0. \tag{3.5}$$

We now assume that the free-energy, φ, is a function only of the elastic displacement jumps by

$$\varphi = \hat{\varphi}(\boldsymbol{\delta}^e). \tag{3.6}$$

Then, by substituting back into Eq. 3.5, $\mathbf{t}$ is found to be

$$\mathbf{t} = \frac{\partial \hat{\varphi}(\boldsymbol{\delta}^e)}{\partial \boldsymbol{\delta}^e}, \tag{3.7}$$

and the remaining inelastic dissipation is

$$\Gamma = \mathbf{t} \cdot \dot{\boldsymbol{\delta}}^p \geq 0. \tag{3.8}$$

For conditions of small elastic displacement jumps in the interface, we assume a simple quadratic free-energy

$$\varphi = \frac{1}{2}\boldsymbol{\delta}^e \cdot \mathbf{K}\boldsymbol{\delta}^e, \tag{3.9}$$

with $\mathbf{K}$ denoting the interface elastic stiffness tensor. Using Eq. 3.7 and the definition given in Eq. 3.9, we derive

$$\mathbf{t} = \mathbf{K}\boldsymbol{\delta}^e = \mathbf{K}(\boldsymbol{\delta} - \boldsymbol{\delta}^p). \tag{3.10}$$

The interface elastic stiffness tensor is a positive definite tensor. The interface model is taken to be isotropic in the tangential response, thus $\mathbf{K}$ takes the form

$$\mathbf{K} = K_N \mathbf{n} \otimes \mathbf{n} + K_T(\mathbf{1} - \mathbf{n} \otimes \mathbf{n}). \tag{3.11}$$

The normal elastic stiffness is defined $K_N > 0$ and the tangential elastic stiffness is defined $K_T > 0$.

The interface traction $\mathbf{t}$ is additively decomposed into normal and tangential parts, $\mathbf{t}_N$ and $\mathbf{t}_T$, respectively, as

$$\mathbf{t} = \mathbf{t}_N + \mathbf{t}_T, \tag{3.12}$$

where

$$\mathbf{t}_N \equiv (\mathbf{n} \otimes \mathbf{n})\ \mathbf{t} = (\mathbf{t} \cdot \mathbf{n})\ \mathbf{n} \equiv t_N\, \mathbf{n} \tag{3.13}$$

$$\mathbf{t}_T \equiv (\mathbf{1} - \mathbf{n} \otimes \mathbf{n})\ \mathbf{t} = \mathbf{t} - \mathbf{t}_N = \mathbf{t} - t_N\, \mathbf{n}. \tag{3.14}$$

Here, the magnitude of normal traction $\mathbf{t}_N$ is the normal stress t_N and the magnitude of the tangential traction $\mathbf{t}_T$ is the shear stress defined by $\bar{\tau} \equiv \sqrt{\mathbf{t}_T \cdot \mathbf{t}_T}$.

3.3 Yield Surface Definition

The elastic domain in the elastic-plastic model is defined by the interior of the intersection of two convex yield surfaces. The yield functions corresponding to each yield surface are taken as

$$\Phi^{(i)}(\mathbf{t}, s^{(i)}) \leq 0, \qquad i = 1, 2. \tag{3.15}$$

Herein, the index $i = 1$ is defined as the normal mechanism and the index $i = 2$ as a shear mechanism. The scalar internal variable $s^{(1)}$ represents the deformation resistance for the normal mechanism, and $s^{(2)}$ represents the deformation resistance for the shear mechanism. In particular, we consider the following simple specific forms for the yield functions:

$$\Phi^{(1)} = t_N - s^{(1)} \leq 0, \tag{3.16}$$

$$\Phi^{(2)} = \bar{\tau} + \mu t_N - s^{(2)} \leq 0, \tag{3.17}$$

where μ represents a friction coefficient. The surface $\Phi^{(1)} = 0$ denotes the normal yield surface in traction space, while the surface $\Phi^{(2)} = 0$ denotes the shear yield surface in traction space. Figure 3-2 illustrates the yield surface of the normal and shear mechanisms. The outward unit normals to the yield surface at the current point in traction space are defined as

$$\mathbf{n}^{(1)} = \frac{\partial \Phi^{(1)}}{\partial \mathbf{t}} = \mathbf{n}, \qquad \mathbf{n}^{(2)} = \frac{\dfrac{\partial \Phi^{(2)}}{\partial \mathbf{t}}}{\left|\dfrac{\partial \Phi^{(2)}}{\partial \mathbf{t}}\right|} = \frac{1}{\sqrt{1+\mu^2}}\left(\frac{\mathbf{t}_T}{\bar{\tau}} + \mu \mathbf{n}\right). \tag{3.18}$$

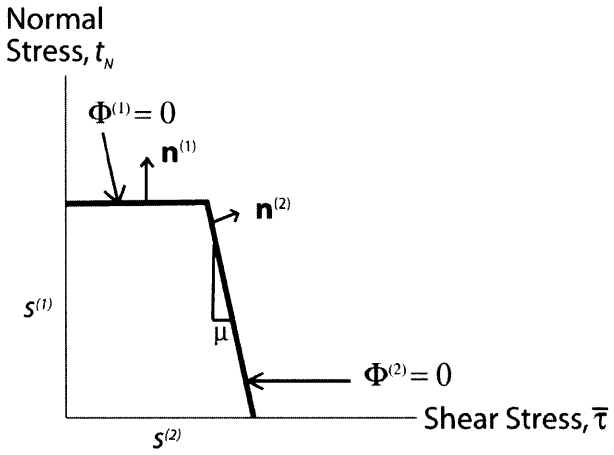

Figure 3-2: Illustration of normal and shear yield surfaces

3.4 Flow Rule

The flow rule is taken as the sum of the contribution from each mechanism

$$\dot{\boldsymbol{\delta}}^p = \sum_{i=1}^{2} \nu^{(i)} \mathbf{m}^{(i)}, \quad \text{with} \quad \mathbf{m}^{(1)} = \mathbf{n}, \qquad \mathbf{m}^{(2)} = \frac{\mathbf{t}_T}{\bar{\tau}}. \tag{3.19}$$

with the inelastic deformation rates $\nu^{(i)} \geq 0$ and $\nu^{(i)}\Phi^{(i)} = 0$. Note that since $\mathbf{m}^{(2)} \neq \mathbf{n}^{(2)}$, we have a non-normal flow rule for the shear response.

During inelastic deformation, an active mechanism must satisfy the consistency condition

$$\nu^{(i)}\dot{\Phi}^{(i)} = 0 \qquad \text{when} \qquad \Phi^{(i)} = 0. \tag{3.20}$$

The consistency condition combines with the yield functions, flow rule, and constitutive relation for $s^{(i)}$ to determine $\nu^{(i)}$, when inelastic deformation occurs.

3.5 Constitutive Equations for Deformation Resistance

We let the equivalent relative plastic displacements for the normal and shear mechanisms be defined by $\gamma^{(1)} \stackrel{\text{def}}{=} \int_0^t \nu^{(1)}(\xi)\, d\xi$ and $\gamma^{(2)} \stackrel{\text{def}}{=} \int_0^t \nu^{(2)}(\xi)\, d\xi$, respectively. The traction-separation behavior of the constitutive interface model is depicted in Figure 3-3. While both the normal and shear mechanisms showed strain hardening characteristics, an elastic perfectly-plastic traction-separation model will be used as a first approach. The interface, in both directions, deforms elastically until it reaches the initial strength values of $s_0{}^{(1)}$ and $s_0{}^{(2)}$. The interface then is perfectly plastic until reaching a critical displacement jump. Once reaching a critical displacement jump, $\gamma_{cr}{}^{(i)}$, the traction decreases linearly until reaching a failure displacement jump, $\gamma_f{}^{(i)}$. (The traction-separation curve in the shear direction assumes a constant value of t_N.)

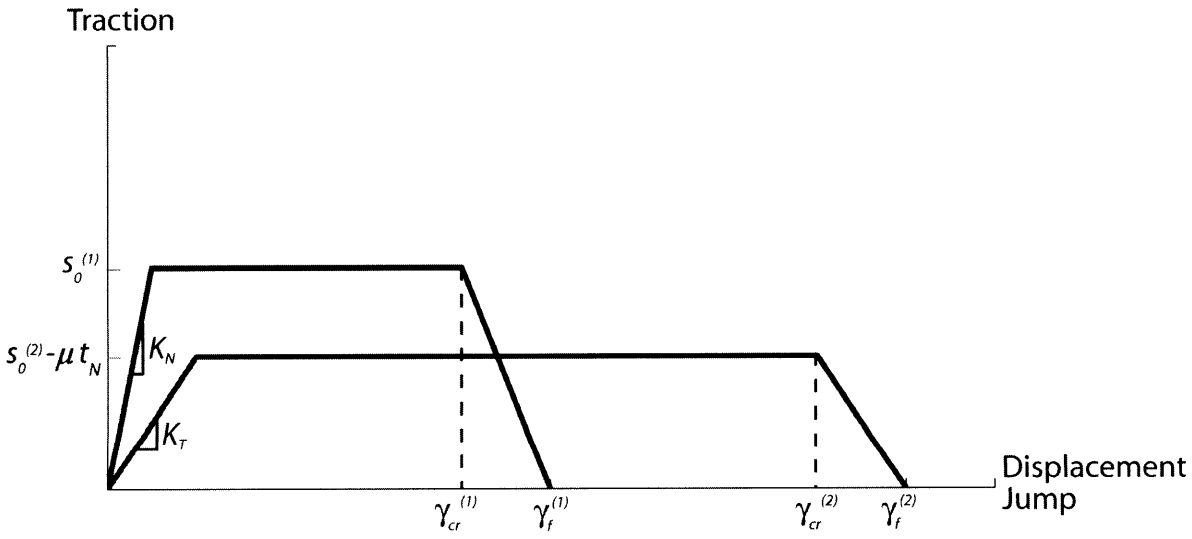

Figure 3-3: Traction-separation behavior for interface under monotonic loading

3.5.1 Rate Independent Combined Normal and Shear Loading

The resistance to deformation is a function of the displacement jump angle, θ_δ, found at the interface equal to

$$\theta_\delta = \arctan\left(\frac{\delta^{(1)}}{\delta^{(2)}}\right) \qquad \text{for } \delta^{(1)} > 0, \qquad \delta^{(2)} > 0. \tag{3.21}$$

Recall, the displacement jump in the normal and shear directions equal

$$\delta^{(1)} = \mathrm{u}^{+(1)} - \mathrm{u}^{-(1)} \tag{3.22}$$

$$\delta^{(2)} = \mathrm{u}^{+(2)} - \mathrm{u}^{-(2)} \tag{3.23}$$

The constitutive relation for rate independent deformation resistances, $s^{(1)}$ and $s^{(2)}$, is shown below as

$$s^{(i)} = \hat{s}^{(i)}\left(\theta_\delta\right), \tag{3.24}$$

$$\text{with} \qquad \hat{s}^{(i)}\left(\theta_\delta\right) = \begin{cases} s_0^{(i)}\left(\theta_\delta\right) & \text{if } \gamma^{(i)} \leq {\gamma_{cr}}^{(i)}, \\ s_0^{(i)}\left(\theta_\delta\right) \dfrac{{\gamma_f}^{(i)} - \gamma^{(i)}}{{\gamma_f}^{(i)} - {\gamma_{cr}}^{(i)}} & \text{if } {\gamma_{cr}}^{(i)} < \gamma^{(i)} \leq {\gamma_f}^{(i)}. \end{cases} \tag{3.25}$$

The material parameters of the model are the normal and tangential stiffness, K_N and K_T, the initial normal and shear strength, ${s_0}^{(1)}$ and ${s_0}^{(2)}$, the normal and shear critical displacement jump, ${\gamma_{cr}}^{(1)}$ and ${\gamma_{cr}}^{(2)}$, and the normal and shear failure displacement jump, ${\gamma_f}^{(1)}$ and ${\gamma_f}^{(2)}$.

Exact forms for the dependence of the initial strength on jump angle, ${s_0}^{(i)}(\theta_\delta)$, and the dependence of the critical displacement jump in the shear mechanism, ${\gamma_{cr}}^{(2)}(\theta_\delta)$, on displacement jump angle are found in Chapter 4.

3.6 Chapter Summary

We have now delineated the constitutive framework for the description of the adhesive interface when subjected to combined normal and shear loading. The next chapter will detail the specific forms found for the constitutive model.

In Chapter 6 a rate dependent constitutive model for adhesive interfaces subjected to combined loading will be outlined.

Chapter 4

Rate Independent Model Calibration

The following chapter details results of the calibration experiments presented in Chapter 2, with the calibration of the rate independent constitutive model presented in Chapter 3. Furthermore, specific forms for quantities dependent on displacement jump and the fit for all calibration experiments are presented in comparison to experimental results.

4.1 Combined Normal and Shear Loading

In order to fit the combined loading model, the following material parameters must be properly calibrated:

- Elastic stiffnesses: K_N and K_T
- Coefficient of friction: μ
- Initial deformation resistances: $s_0^{(1)}(\theta_\delta)$ and $s_0^{(2)}(\theta_\delta)$
- Critical and failure displacement jumps: ${\gamma_{cr}}^{(1)}$, ${\gamma_{cr}}^{(2)}(\theta_\delta)$, ${\gamma_f}^{(1)}$, and ${\gamma_f}^{(2)}(\theta_\delta)$

The normal elastic stiffness, K_N, at the interface is fit to the elastic portion of the traction-separation curve from the adhesive tested in tension referring back to Figure 2-13. The numerical fit for K_N of the interface is 15 GPa/mm. The numerical fit of the tangential elastic stiffness, K_T, of the interface is 5.6 GPa/mm. For this study, the coefficient of friction, μ, at the interface has not been calibrated experimentally and will be assumed to be zero.

As seen in the experimental results presented in Chapter 2, the behavior of shear strength and critical displacement jump decreases as the applied angle increases. Note that while the displacement jump angle is not the same as the applied angle, the trend is nearly identical.

Recall the definition of displacement jump angle:

$$\theta_\delta = \arctan\left(\frac{\delta^{(1)}}{\delta^{(2)}}\right). \tag{4.1}$$

Figure 4-1 shows the experimental shear strength point data for the combined loading experiments as a function of displacement jump angle. The dashed line is the numerical fit found for the data. The specific exponentially decreasing form of the initial resistance to

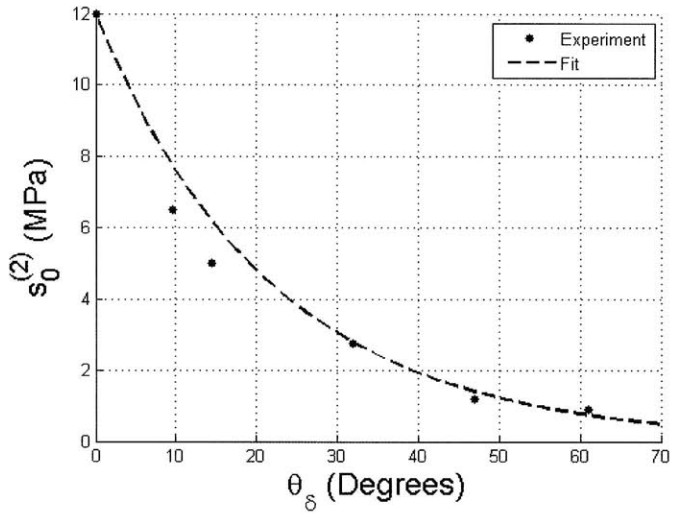

Figure 4-1: Dependence of shear deformation resistance to flow, ${s_0}^{(2)}$, on displacement jump angle

plastic flow in the shear direction, ${s_0}^{(2)}(\theta_\delta)$, is given as:

$$s_0^{(2)}(\theta_\delta) = {s_0}^{(2)}|_{0^\circ} \cdot e^{-\beta\,\theta_\delta} \qquad \text{for} \qquad \frac{\delta^{(1)}}{\delta^{(2)}} > 0.1 \tag{4.2}$$

where ${s_0}^{(2)}|_{0^\circ}$ is the initial resistance of the adhesive tested in simple shear found experimentally to be 12 MPa. The constant $\beta = 0.0457$ is found using a least squares fit to the experimental data.

A plot of the experimental critical shear displacement jump as a function of jump angle is shown in Figure 4-2. The ordinate of this plot is the normalized critical displacement jump where the interface thickness is equal to 0.1 mm.

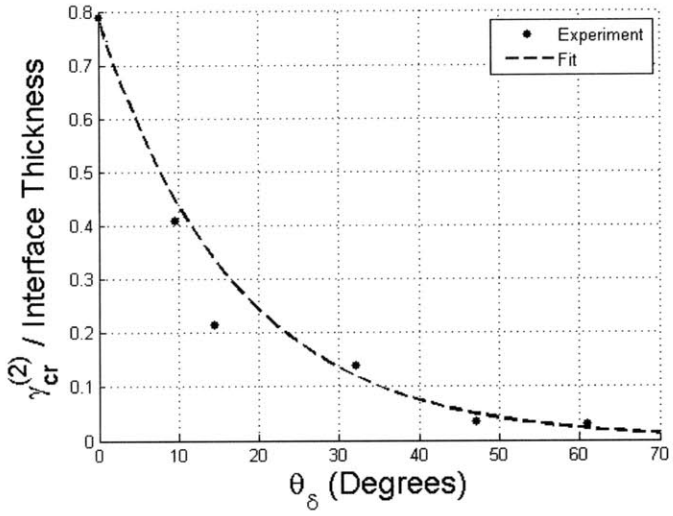

Figure 4-2: Dependence of shear critical displacement jump, ${\gamma_{cr}}^{(2)}$, on displacement jump angle

The specific exponentially decreasing form of the critical shear displacement jump, ${\gamma_{cr}}^{(2)}(\theta_\delta)$ is given as:

$$ {\gamma_{cr}}^{(2)}(\theta_\delta) = {\gamma_{cr}}^{(2)}|_{0^\circ} \cdot e^{-\eta\,\theta_\delta} \qquad \text{for} \qquad \frac{\delta^{(1)}}{\delta^{(2)}} > 0.1 \tag{4.3} $$

where ${\gamma_{cr}}^{(2)}|_{0^\circ}$ is the experimentally found critical displacement jump for the adhesive tested in simple shear. The constants for the fit, shown as a dashed line in Figure 4-2, are: ${\gamma_{cr}}^{(2)}|_{0^\circ} = 0.79$ and a $\eta = 0.0588$ (found with a least squares method). Since experimentally, the simple shear experiments on the adhesive resulted in a normalized critical displacement jump in that direction equal to 0.79 and a normalized failure displacement jump equal to 0.80, the reduction of the failure displacement jump will be assumed to follow the same trend. The specific form for the failure displacement jump in shear due to combined loading is

$$ {\gamma_f}^{(2)}(\theta_\delta) = {\gamma_{cr}}^{(2)}(\theta_\delta) + .01 \qquad \text{for} \qquad \frac{\delta^{(1)}}{\delta^{(2)}} > 0.1. \tag{4.4} $$

The specific form of the initial resistance to deformation in the normal direction, $s_0^{(1)}(\theta_\delta)$ is shown in Eq. 4.5, and a plot of the experimental critical shear displacement jump as a function of jump angle is shown in Figure 4-2. The ordinate of this plot is the initial deformation resistance in the normal direction. The dashed line in the figure represents the fit of the data equal to the specific logarithmic form shown in Eq. 4.5.

$$ s_0^{(1)}(\theta_\delta) = a \cdot \ln(\theta_\delta) + c \qquad \text{for} \qquad \frac{\delta^{(1)}}{\delta^{(2)}} > 0.1 \tag{4.5} $$

The constants for the fit are found from least squares fit analysis to be: $a = 2.9414$ and $c = 8.7835$.

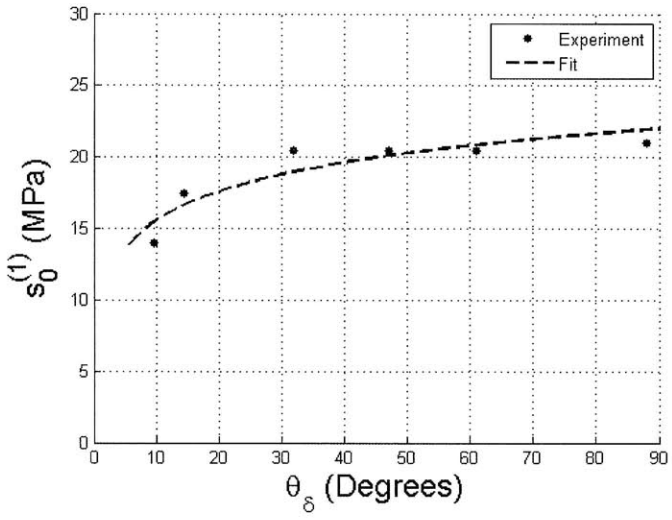

Figure 4-3: Dependence of normal deformation resistance to flow, ${s_0}^{(1)}$, on displacement jump angle

The normal critical displacement jump ${\gamma_{cr}}^{(1)}$ did not show any strong dependence on displacement jump angle and is constant when subjected to combined loading. Therefore, the calibrated values are ${\gamma_{cr}}^{(1)} = 0.27$ and ${\gamma_f}^{(1)} = 0.35$ taken from the pure tension experiment.

4.2 Numerical Simulations

The rate independent constitutive model is implemented using a USER INTERFACE subroutine (VUINTER) within the finite-element computer program ABAQUS/Explicit Version 6.8.1[10]. A finite element model of plane strain CPE4R elements is created to model the calibration experiments performed at a variety of angles and rates. The geometry is created using ABAQUS CAE Version 6.8.1 and separate upper and lower blocks (68 mm x 5 mm) are created and meshed. The 4480 finite element model mesh, with a plane strain thickness of 8 mm, can be seen in Figure 4-4.

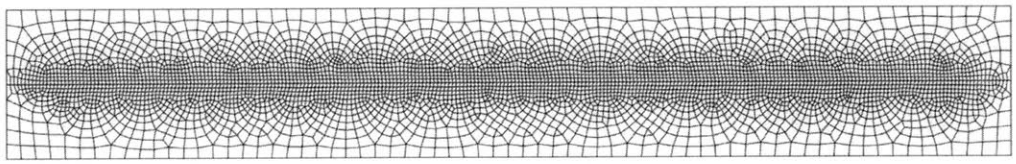

Figure 4-4: Finite element mesh of calibration experiment

The 6061-T6 Aluminum material is modeled as rate independent with isotropic elastic-plastic properties. This is achieved with ABAQUS's built in implementation of J_2-flow theory of plasticity. The material properties of the 6061-T6 aluminum used are shown in Table 4.1. The plastic behavior of the aluminum is tailored to the true stress-plastic strain curve shown in Figure 4-5.

Table 4.1: 6061-T6 aluminum material properties

Property	Value
Density	2.79 x 10^{-9} Mg/mm^3
Young's Modulus	62.50 GPa
Poisson's Ratio	0.33
Initial Yield Strength	300 GPa

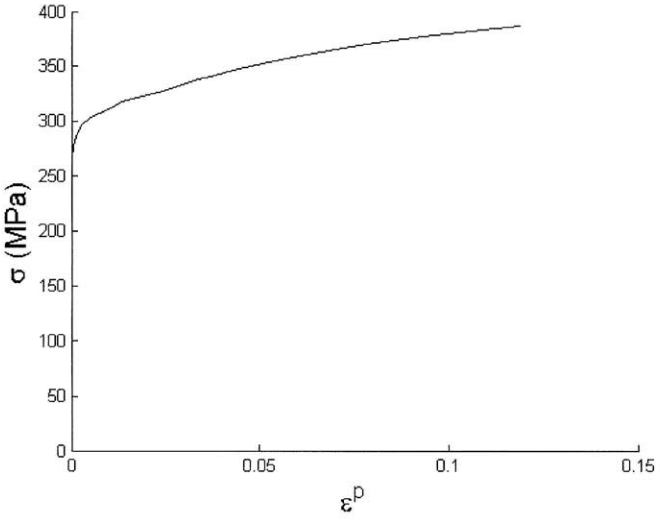

Figure 4-5: True stress-true plastic strain curve for 6061-T6 aluminum

The contact pair of surfaces is required to be defined in the finite element model. The bottom surface of the upper block is selected as the slave surface and the top surface of the bottom block is selected as the master surface for the contact pair specifications.

A magnified view of the elements compromising the interface is shown in Figure 4-6. The effectiveness of the VUINTER is dependent on the fineness of mesh along the contact surfaces, as well as the alignment of the top contact surface nodes and the bottom contact surface nodes at the interface. In other words, it is not ideal to have a node on the top block along the interface offset in the tangential direction in any way.

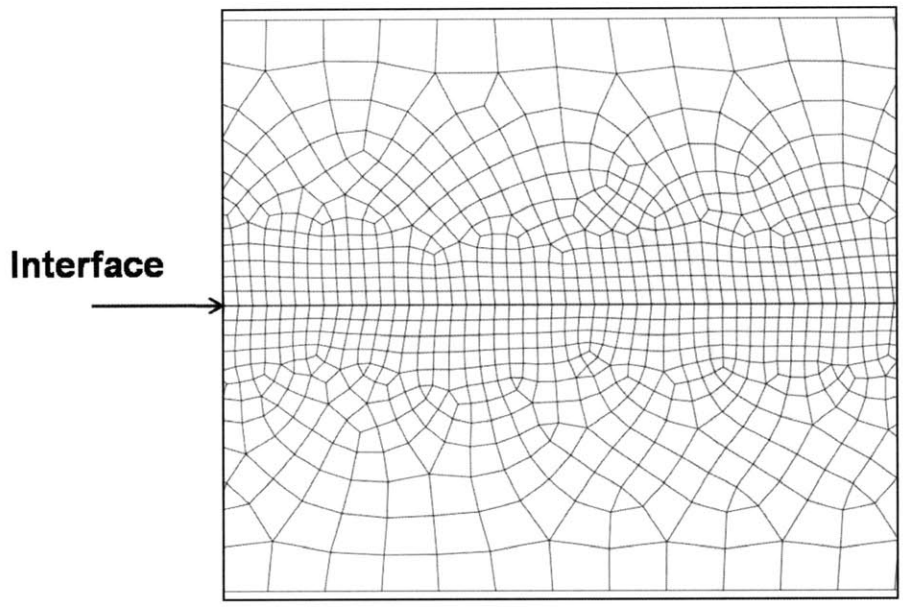

Figure 4-6: Detail of interface

For the calibration simulations, the boundary conditions are prescribed to be identical to the experiment. The top nodes of the upper block are restricted in the horizontal direction but move vertically. The bottom nodes of the lower block move horizontally and are restricted in the vertical direction.

4.3 Combined Loading Calibration Results

The simulations for the combined loading, using the VUINTER subroutine, are simulated to fit the data presented in Chapter 2. Since the calibration experiments are under monotonic loading, the user subroutine calculated the displacement jump angle only once at the very beginning of the first time step. The VUINTER has the built in variable *rDisp* which is an array containing the relative positions between the two surfaces [10]. The interfacial constitutive behavior for the normal and shear directions has been applied to the two surfaces. The combined loading constitutive behavior is induced if the ratio of $\frac{\delta^{(1)}}{\delta^{(2)}} > 0.1$ and if the normalized minimum values of $\delta^{(1)}$ (1e-6) and $\delta^{(2)}$ (1e-4) are met. In the shear direction, a minimum shear stress of 0.1 MPa was specified once the displacement jump reached the value of critical displacement, which can be seen in some plots.

Figures 4-7 and 4-8 are the fit of the model to the normal traction-separation and shear traction-separation curves. Notice, the elastic-perfectly plastic model in the normal direction has an initial deformation resistance, ${s_o}^{(1)}$, equal to 21 MPa. The critical displacement jump is equal to 0.027 mm and failure displacement jump is 0.035 mm. The elastic-perfectly plastic model in the shear direction has an initial deformation resistance, ${s_o}^{(2)}$, equal to 12 MPa,

and the critical displacement jump is equal to 0.079 mm and failure displacement jump is 0.08 mm.

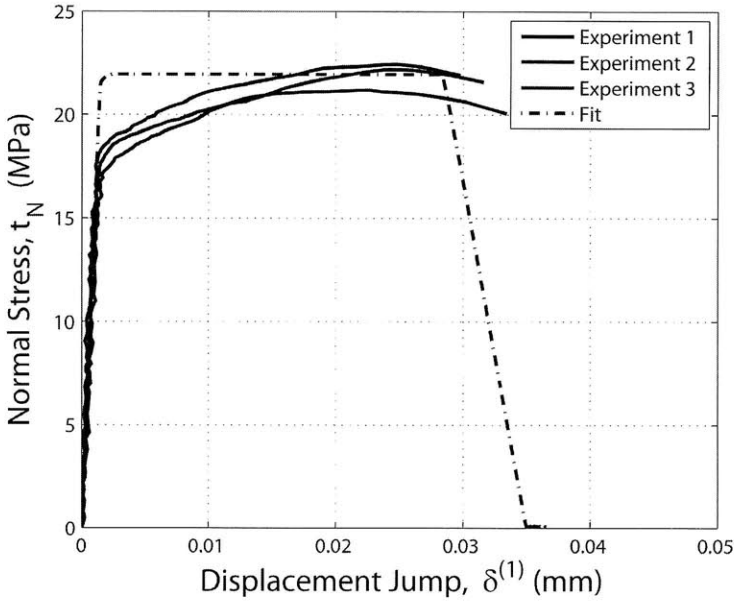

Figure 4-7: Fit of traction-separation behavior of adhesive tested in normal direction

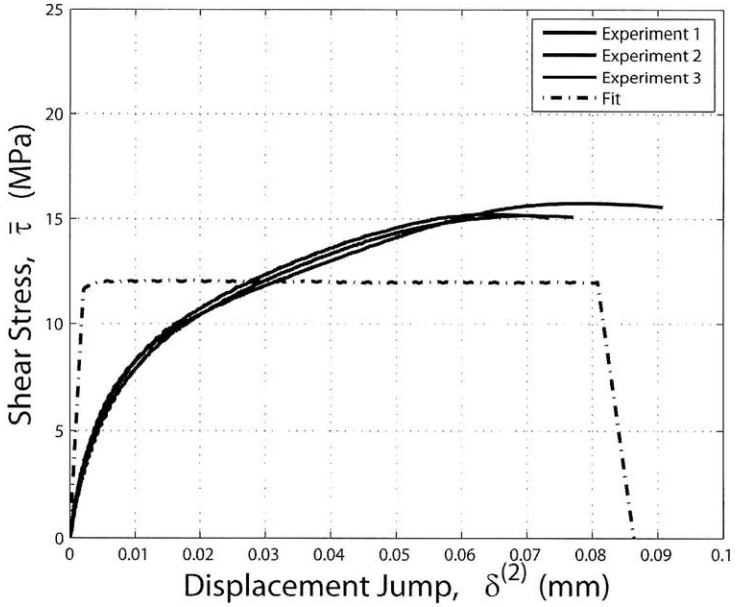

Figure 4-8: Fit of traction-separation behavior of adhesive tested in shear direction

The results of the calibrated fit of the model to all the combined loading applied angles tested, 7.0°, 10.6°, 22.0°, 34.9°, and 50.4°, are shown in Figures 4-9, 4-10, 4-11, 4-12, and 4-13.

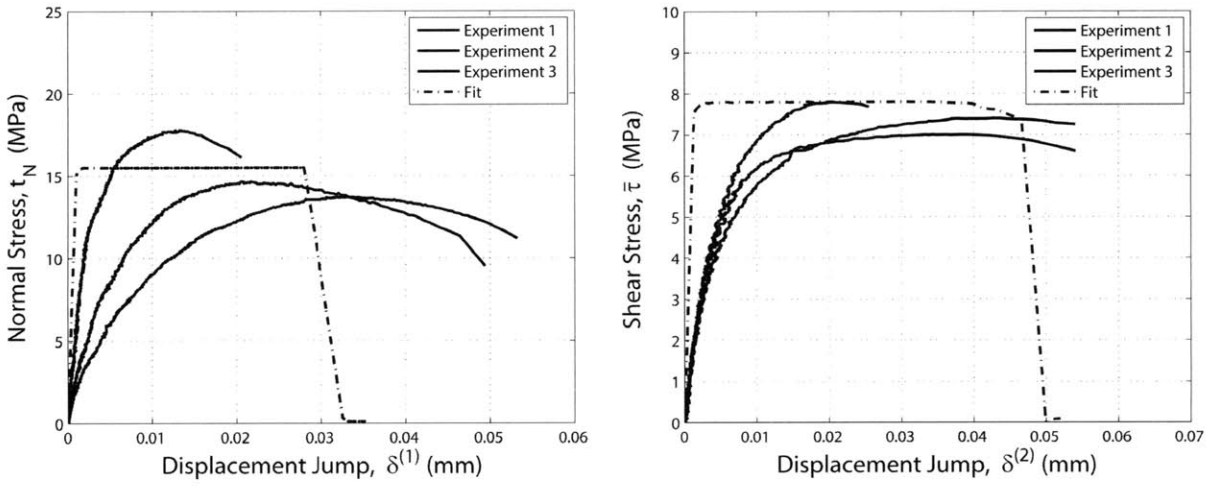

Figure 4-9: Fit of traction-separation behavior of adhesive tested at 7.0° (a) normal and (b) shear

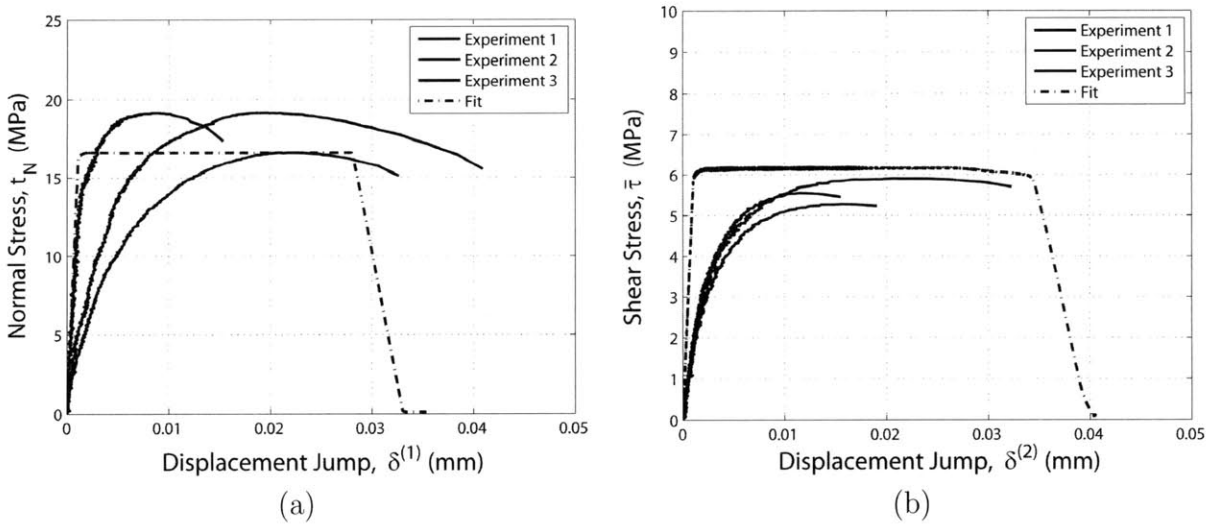

Figure 4-10: Fit of traction-separation behavior of adhesive tested at 10.6° (a) normal and (b) shear

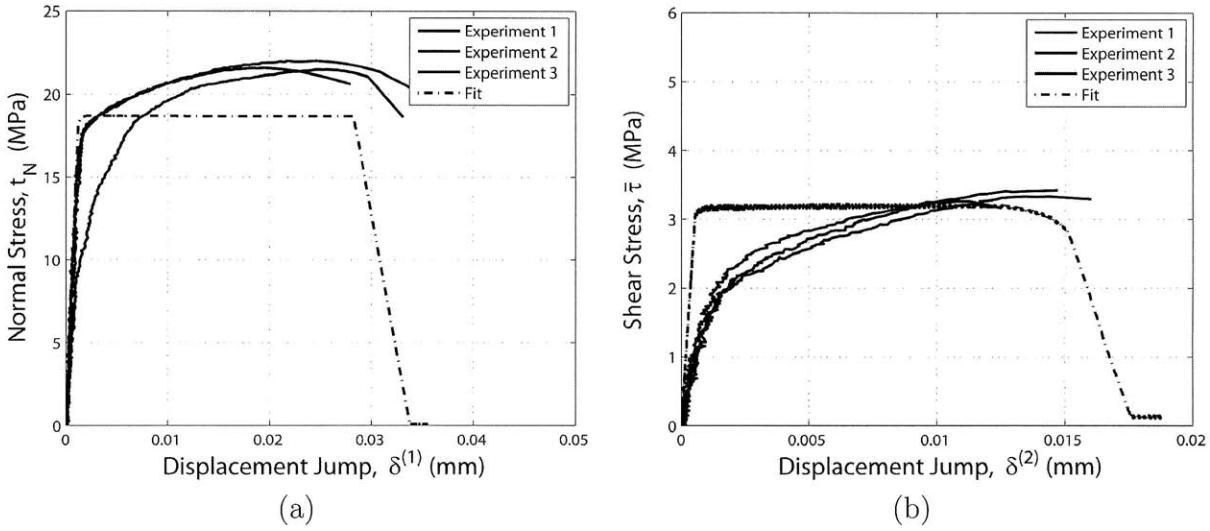

Figure 4-11: Fit of traction-separation behavior of adhesive tested at 22.0° (a) normal and (b) shear

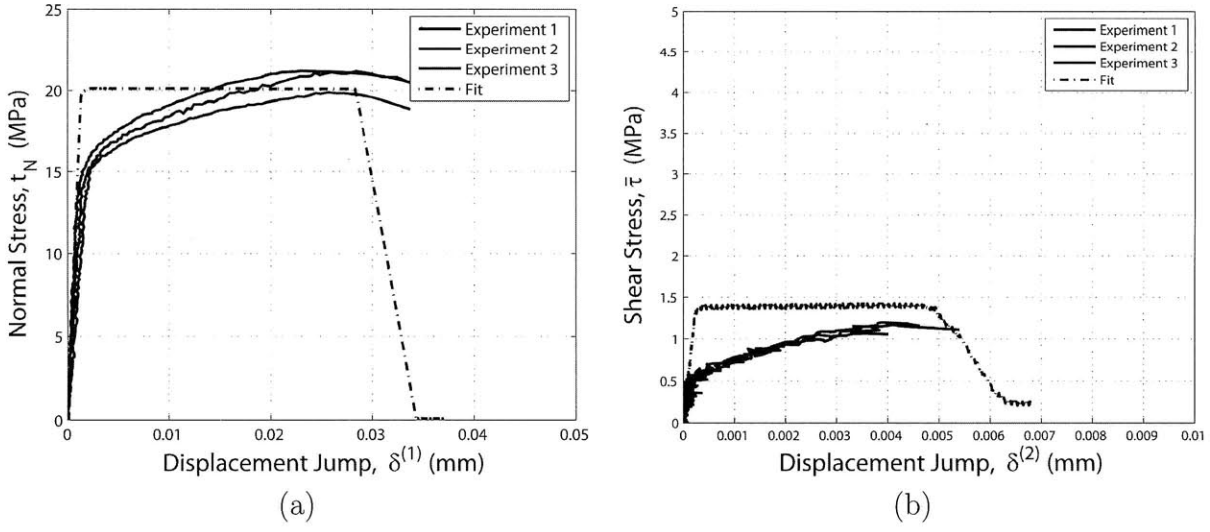

Figure 4-12: Fit of traction-separation behavior of adhesive tested at 34.9° (a) normal and (b) shear

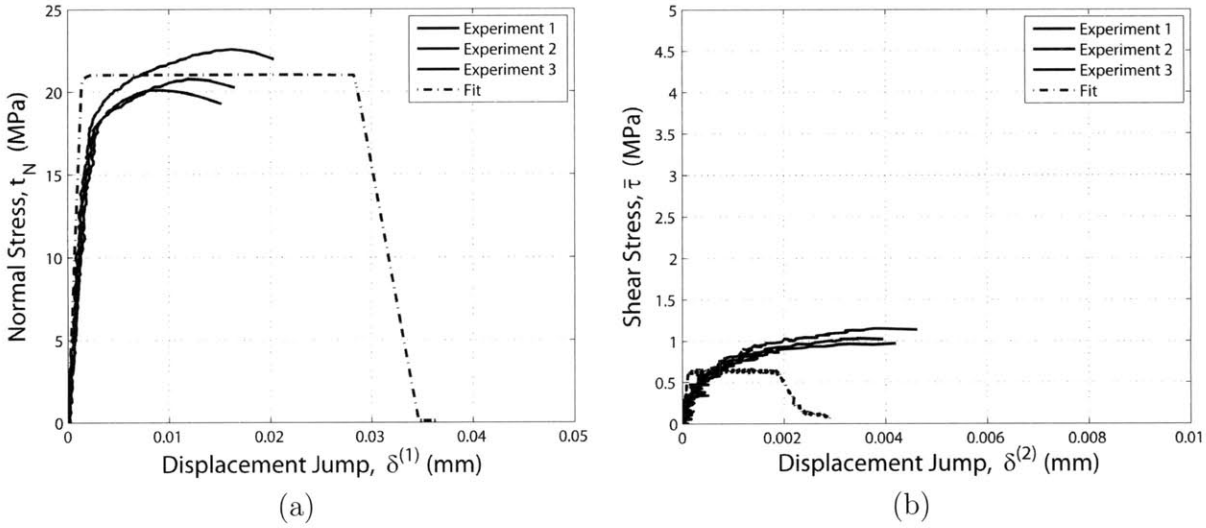

Figure 4-13: Fit of traction-separation behavior of adhesive tested at 50.4° (a) normal and (b) shear

As shown, the numerically implemented constitutive model predicts the experimentally found normal and shear traction-separation results fairly well. Notice also, we are able to fairly well fit the initial strength of the adhesive and the critical and failure displacement jumps, thus fairly well capturing the area under the traction-separation curve or toughness. The limitations of an elastic-perfectly plastic model are apparent in the inability to capture the strain hardening and softening seen in the experiments.

4.4 Chapter Summary

The rate independent constitutive model for the adhesive interface has been calibrated to the combined normal and shear loading experiments performed. This constitutive model has been implemented into a VUINTER user subroutine in ABAQUS/Explicit, and it can now be applied to other geometries exhibiting combined loading behaviors.

Chapter 5

Rate Independent Model Application

In order to explore the reach of the constitutive model, validation experiments and simulations are performed for two different geometries. First, two curvilinear blocks are bonded together and tested at two different angles. Second, a small scale notched four point bend geometry is tested at a single rate. Numerical simulations of both experiments are performed and the results are discussed below.

5.1 Curvilinear Block Geometry

The bonded curvilinear block geometry examined can be seen in a final prepared specimen form in Figure 5-1, and the dimensions of one half of the geometry are shown in Figure 5-2. As can be seen, the chosen geometry conveniently allows it to be tested in the biaxial testing apparatus used for the calibration experiments.

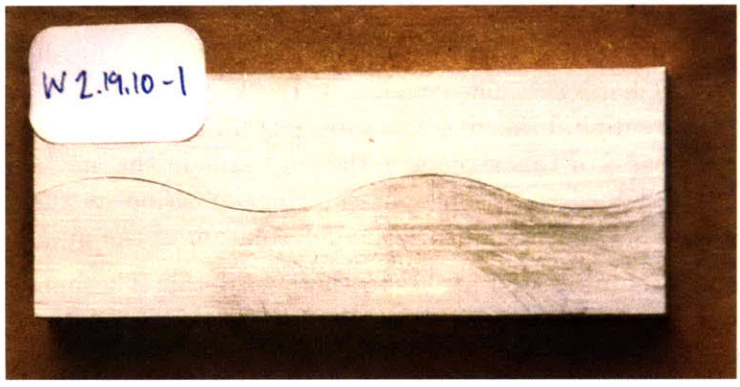

Figure 5-1: Prepared curvilinear block specimen

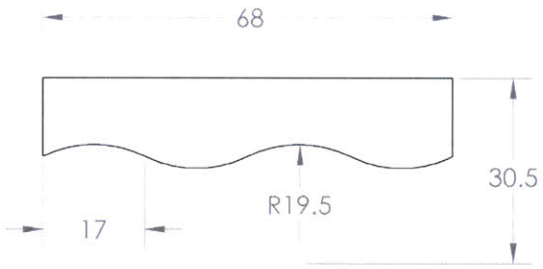

Figure 5-2: Curvilinear block geometry, thickness = 8 mm (all dimensions in mm)

5.1.1 Experiment

The curvilinear block geometry is precision cut from bare 6061-T6 Aluminum with dimensions given in Figure 5-2. As described in Chapter 2, the aluminum adherends are prepared first by hand sanding the curved surface to be bonded with 240 grit emery paper. The adherends are rinsed with water and dried. Length and width measurements are taken with a digital caliper and recorded. The adherends are then cleaned with acetone soaked high absorbency, low particle generating, composite clean room wipes, until they wipe clean. Finally, isopropyl alcohol is used to wipe all sides of the adherends.

In order to establish the chosen bond thickness of 0.1 mm, wire of that diameter is chosen for insertion into the bond. Two wires are wiped with isopropyl alcohol and then taped in place approximately 8 mm from each end of the lower adherend.

The Hysol®EA 9361 adhesive is prepared, applied, cured, and finished identically to the procedure described in Chapter 2. The curvilinear block specimens are then prepared identically for usage with the digital image correlation system by spray painting the same black on white speckled pattern. For this geometry, the gage area in the machine is approximately 5.1 mm x 68 mm. The DIC is positioned in the same position as that described for the calibration experiments in order to capture the deformation of the middle of the specimen.

The curvilinear blocks are tested at 90° to the horizontal. The bottom block is held in displacement and the upper block is displaced. Displacement in the vertical direction will test the areas of the block that are not perpendicular to the axis of loading, thus inducing an applied angle at the interface. This experiment is completed for a rate of 0.53 x 10^{-3} mm/s. Figure 5-3 depicts the 90° curvilinear block experiment. Here, gray area represents the part of the specimen held by the biaxial grips.

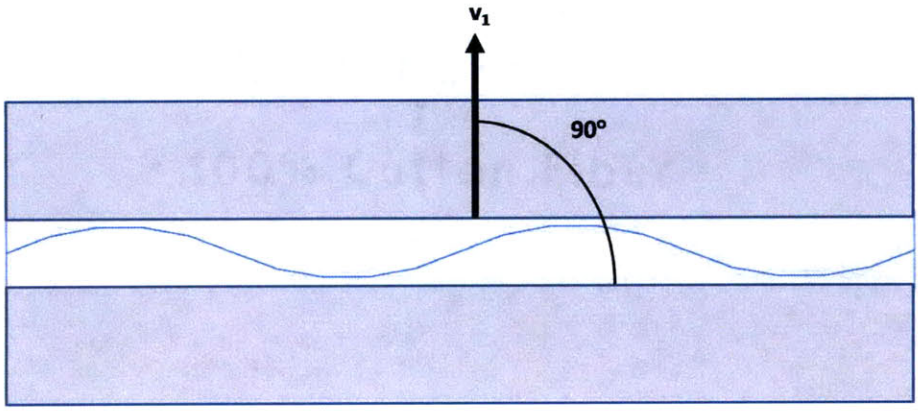

Figure 5-3: Diagram of curvilinear block experiment at 90°

The curvilinear blocks are also tested at an applied angle of 35° to the horizontal as seen in Figure 5-4. This applied angle provides for some additional combination loading angles through the bond line as it curves. This experiment is completed for the rate of 0.65 x 10^{-3} mm/s.

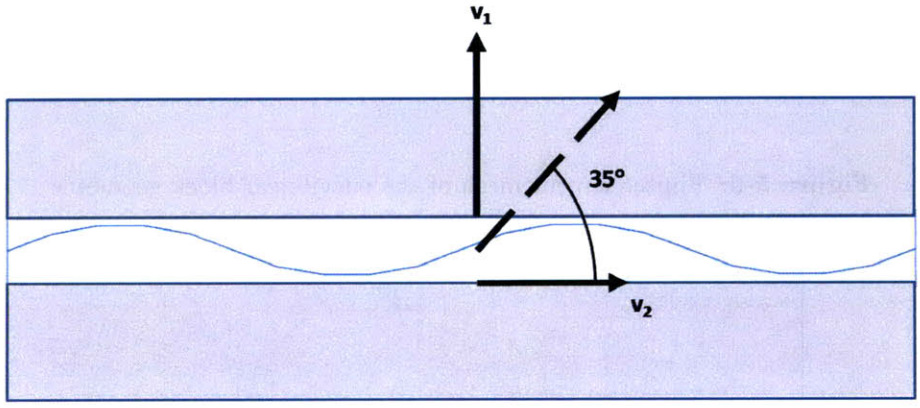

Figure 5-4: Diagram of curvilinear block experiment at 35°

The experimental displacement data presented in the following section is taken with the DIC system and is on the center of the curvilinear block geometry shown in Figure 5-5. This figure shows a drawn white outline of where the interface falls and two points on the upper and lower adherend that are very close to the adhesive. The vertical displacement jump of the center of the experimental is $u_y{}^{+} - u_y{}^{-}$ and the horizontal displacement at the center of the experimental is $u_x{}^{-} - u_x{}^{+}$.

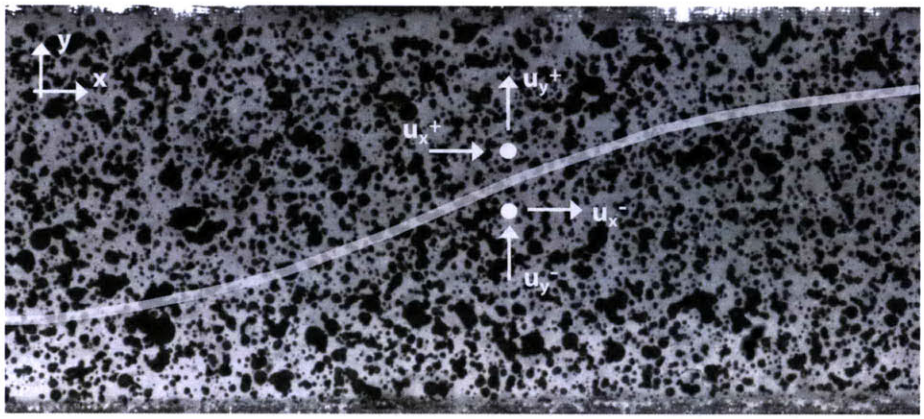

Figure 5-5: Detail of location of displacement jump calculation location

5.1.2 Simulation and Prediction

The curvilinear wave geometry is meshed into a 4008 CPE4R finite element model. The mesh of the wave geometry can be seen in Figure 5-6, and a detailed view is shown in Figure 5-7.

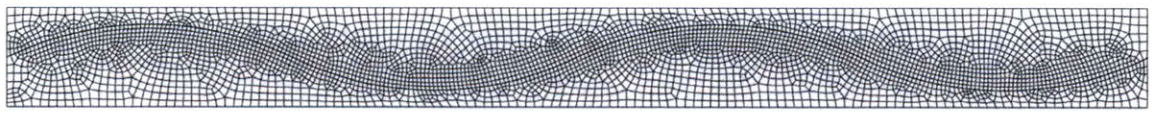

Figure 5-6: Finite element mesh of the curvilinear block geometry

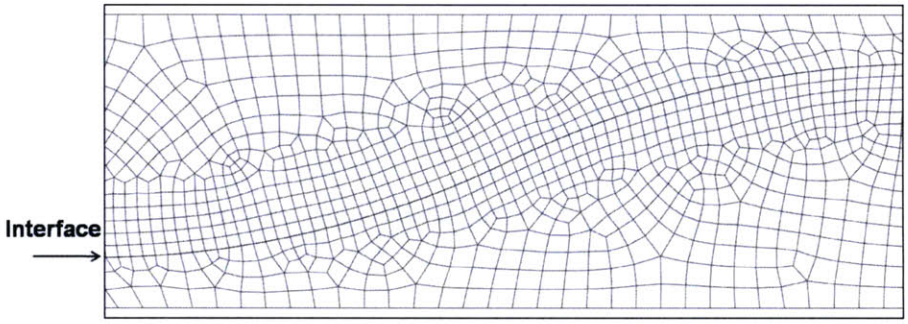

Figure 5-7: Detail view of meshed interface

For the 90° from horizontal applied angle simulation, the bottom nodes of the lower adherend are fixed in position in both directions. The top nodes of the upper adherend are

prescribed a velocity equal to that found at the upper grip of the experiment. For the 35° from horizontal applied angle simulation, the bottom nodes of the lower adherend are given a velocity equal to that applied at the lower grip during the experiment. The top nodes of the upper adherend are given a velocity equal to the experimentally found velocity at the upper grip. Each node in the simulation will have a different calculated displacement jump angle, unlike the calibration simulations of the butt joint specimens.

A photo taken by the digital image correlation system at the beginning of the 90° applied angle experiment and at the failure of the adhesive interface are shown in Figure 5-8 (a) and Figure 5-8 (b). The experimental load-displacement curve of the curvilinear block geometry loaded at a 90° applied angle at the rate of 0.53 x 10^{-3} mm/s is shown in Figure 5-9. The vertical load measured in kN is plotted as a function of the vertical displacement jump at the center of the specimen, and the prediction made by the numerical simulation is also shown in Figure 5-9. Notice the ability of the model to predict the load carried in the vertical direction. The critical and failure displacement jumps for the biaxial butt joints tested in the normal direction were found to be 0.027 mm and 0.035 mm respectively. Here we can see, because the geometry has a large amount of area that is solely loaded in the normal direction, the failure occurs at about the same location.

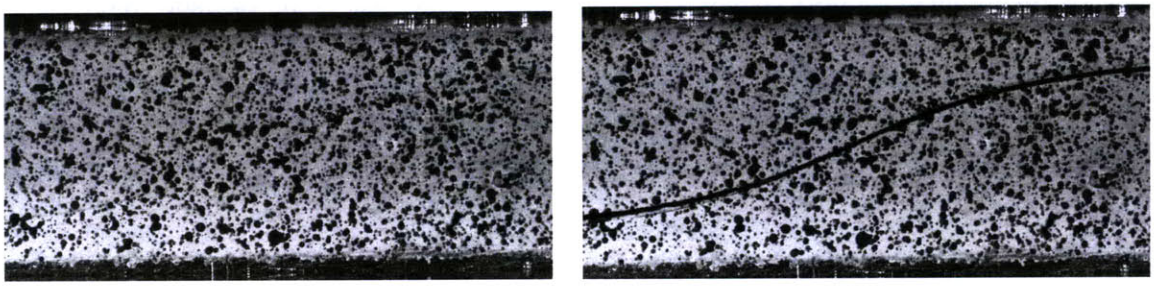

(a) (b)

Figure 5-8: DIC Photo taken of 90° loaded curvilinear blocks (a) before testing (b) at failure

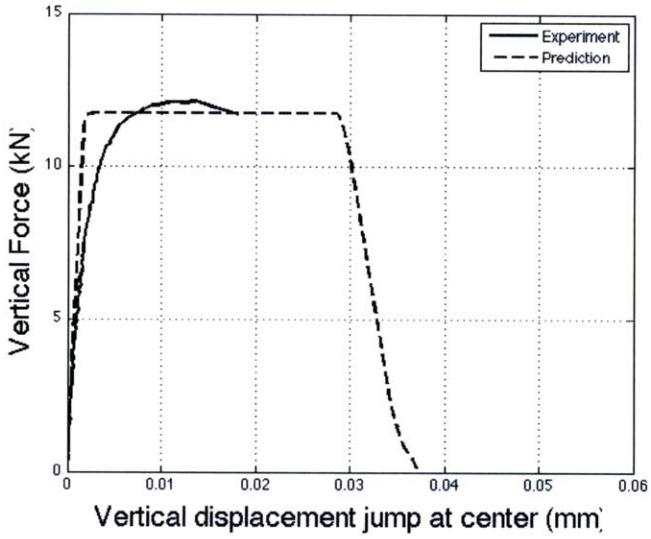

Figure 5-9: Prediction of 90° loaded curvilinear blocks at 0.53 x 10^{-3} mm/s

A photo taken by the digital image correlation system at the beginning of the 35° applied angle experiment and at the failure of the adhesive interface is shown in Figure 5-10. The experimental vertical load-vertical displacement jump plot for the curvilinear geometry tested at an applied angle of 35° can be seen in Figure 5-11(a), and the finite element prediction is overlaid. The strength of the interface is well predicted at about 11 kN until a critical value of displacement jump is reached. The peaks and valleys in the specimen have a displacement jump angle approximately equal to 45° resulting in a decreased critical and failure displacement jump in the shear direction at those nodes. The load decreases down until the nodes along the interface that produce smaller displacement jump angles reach a critical and failure displacement jump in shear.

The experimental horizontal load-horizontal displacement jump plot for the curvilinear geometry tested at an applied angle of 35° is shown in Figure 5-11 (b). Notice the numerical simulation over-predicts the horizontal load carried, which is due to a small under-prediction of displacement jump angle at the interface at the peak and valleys of the geometry. Due to the nature of the exponential function, this predicts a higher strength than what was seen during the experiment.

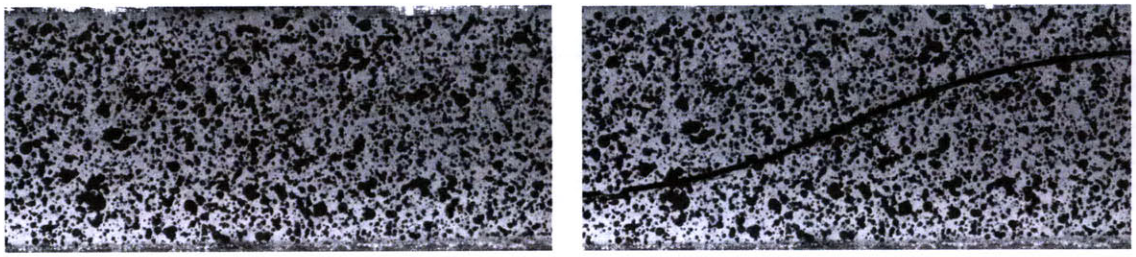

(a) (b)

Figure 5-10: DIC Photo taken of 35° loaded curvilinear blocks (a) before testing (b) at failure

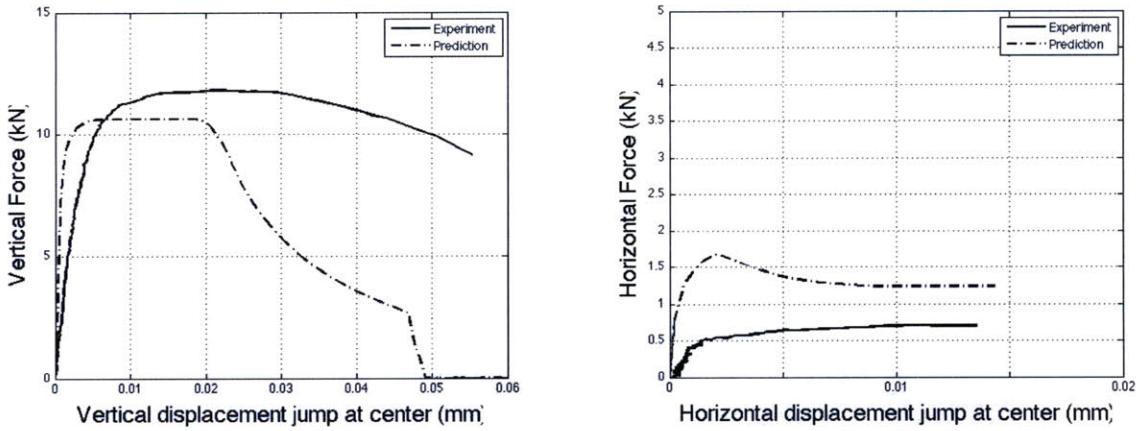

(a) (b)

Figure 5-11: Prediction of 35° loaded curvilinear blocks at 0.65 x 10^{-3} mm/s (a) vertical and (b) horizontal

We can calculate the magnitude of load by taking the sum of squares of the load in the vertical direction and the load in the horizontal direction and the magnitude of the displacement jump can be calculated in the same way. The experimental load magnitude versus displacement jump magnitude is plotted against the prediction of the numerical simulation in Figure 5-12.

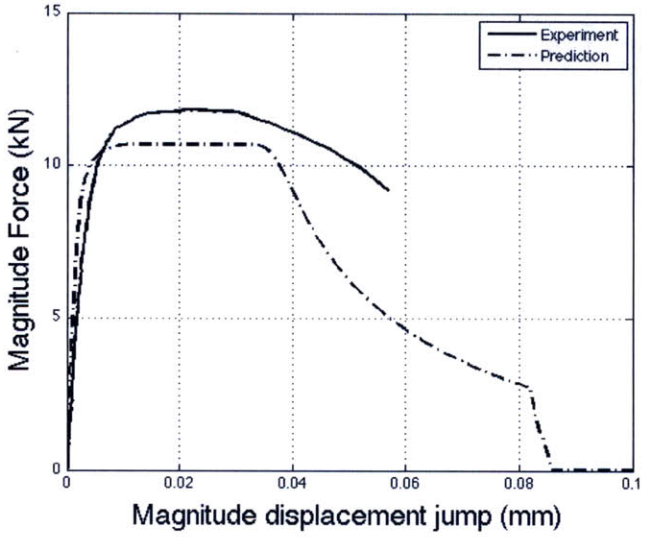

Figure 5-12: Magnitude prediction of 34.9° loaded curvilinear blocks a 0.65 x 10^{-3} mm/s

5.2 Four Point Bend

The second chosen application of the interface model is a small scale notched four point bend experiment, and a photo of a prepared bonded specimen is shown in Figure 5-13. The following sections contain details on the experiment, results, and numerical predictions.

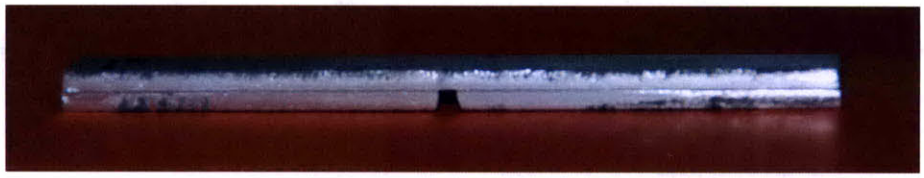

Figure 5-13: Four point bend bonded specimen

5.2.1 Experiment

The specimen of the notched four point bend geometry is comprised of three aluminum adherends: an upper strip of 60 mm x 8 mm x 1.5 mm and two lower strips approximately 29.5 mm x 8 mm x 1.5 mm. A 1 mm x 8 mm notch is left in the center of the assembly, as can be seen in the diagram of the specimen shown in Figure 5-14.

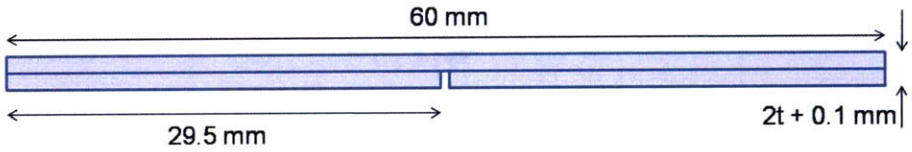

Figure 5-14: Geometry of four point bend experiment specimen; t = 1.5 mm and depth = 8 mm

The bare 6061-T6 aluminum adherends are water jet cut from a 1.5 mm thick plate. The aluminum adherends are prepared first by hand sanding the bonding surfaces with 240 grit emery paper in a random manner. The adherends are rinsed with water and dried. Length, width, and thickness measurements are taken with a digital caliper and micrometer and recorded. The adherends are then cleaned with acetone soaked high absorbency, low particle generating, composite clean room wipes, until they wipe clean. Finally, isopropyl alcohol is used to wipe all sides of the adherends.

The Hysol®EA 9361 adhesive is prepared (Chapter 2) and applied to the bonding surfaces of the three adherends. In order to establish the bond thickness of 0.1 mm, wires of that diameter are chosen for insertion into the bond. Four wires are wiped with isopropyl alcohol and then positioned in place approximately 5 mm from each end of the 29.5 mm long lower adherends. The 60 mm long adherend is laid epoxy up and the two 29.5 mm wet adherends with wires are laid in place using tweezers. Some light loading and hand alignment is done to squeeze out excess epoxy. The wet assembly is then placed into the steel machinist clamps, heat cured, and finished identically to the processes described in Chapter 2. The notched four point bend specimen is then prepared identically for usage with the digital image correlation system by spray painting the same black on white speckled pattern on one exposed side.

The notched four point bend experiment is executed on a Zwick single column testing machine with a 2.5 kN load cell. The control software used for the experiment is testXpert II (V2.01). Two bottom low-friction rollers support the specimen from below while two upper rollers are used to apply a downward displacement to the specimen. A diagram of the four point bend experiment can be seen in Figure 5-15. The two bottom rollers are 50 mm apart and the two upper rollers are 25 mm apart.

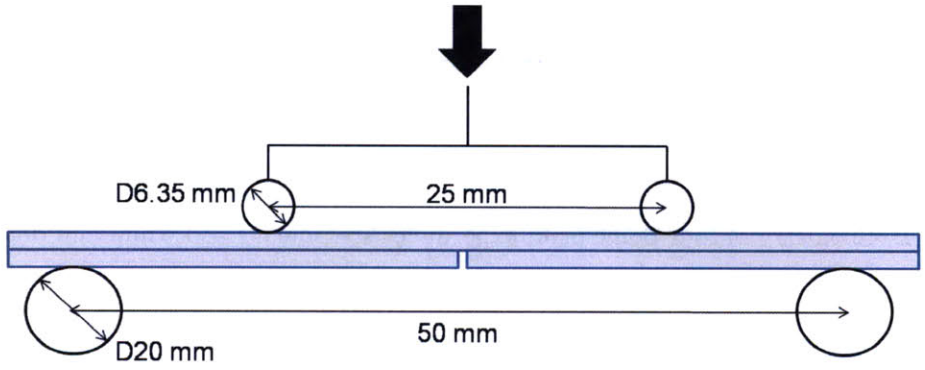

Figure 5-15: Geometry of four point bend experiment

The experiment is displacement controlled and the top rollers are displaced at a rate of 0.833 x 10^{-2} mm/s, while the specimen is free in the depth and length coordinates. The image capturing camera is positioned approximately 0.5 m away from the specimen and 2 frames a second were taken.

As seen in Figure 5-16, the four point bend specimen is placed on top of the bottom rollers with the crosshead lowered to position the top rollers immediately above it. A photo of the specimen deformed in the four point bend bending geometry is shown in Figure 5-17. The results of the experiment are shown in the following section.

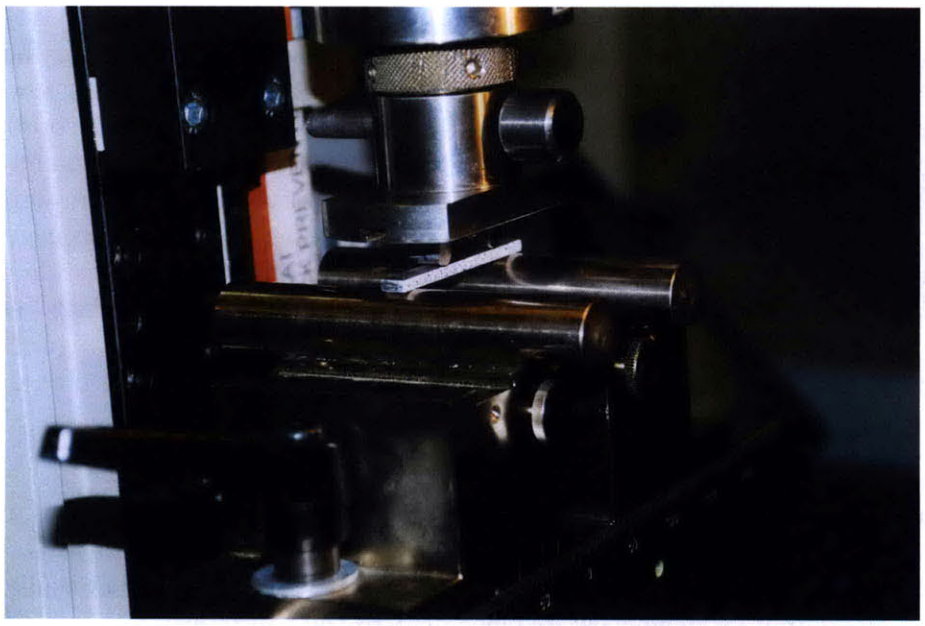

Figure 5-16: Four point bend specimen in testing apparatus prior to experiment

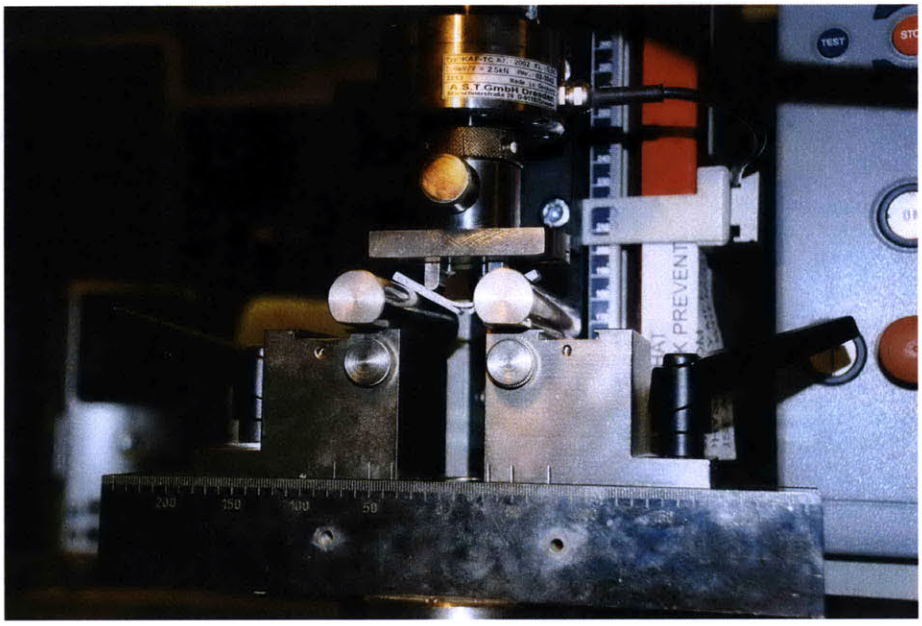

Figure 5-17: Four point bend specimen post experiment

5.2.2 Simulation and Prediction

A half section of the notched four point bend geometry is simulated in the finite element model because of symmetry of the experiment. The two dimensional half geometry is meshed with 1764 ABAQUS CPS4R elements, which are shown in Figure 5-18. Due to the small scale of this experiment and because the in-plane dimension is 8 mm in comparison to the 3.6 mm thickness and 60 mm length, plane stress elements are chosen to better model the behavior of the specimen. A detailed view of the mesh at the interface of the four point bend geometry can be seen in Figure 5-19. Here the upper adherend interface surface is defined as the master surface in the contact pair specification.

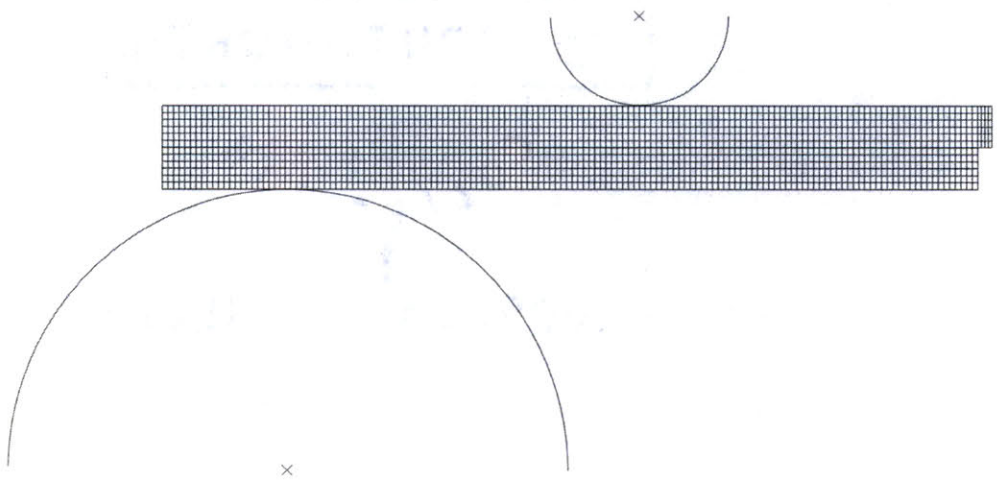

Figure 5-18: Finite element mesh of four point bend experiment

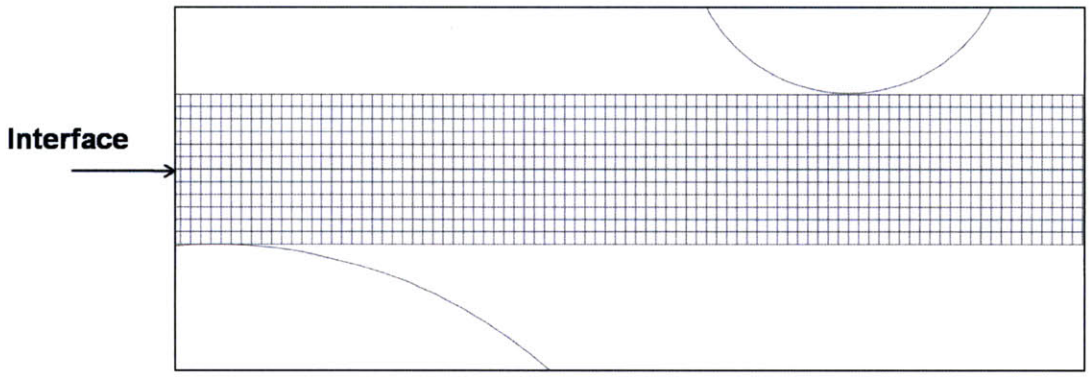

Figure 5-19: Detail of meshed interface

For simplicity, the top and bottom rollers are modeled as frictionless analytical rigid bodies. The bottom roller is fixed in position and the top roller will move down at a velocity equal to the experiment (0.833 x 10^{-2} mm/s).

The displacement of a node on the lower adherend interface 0.2 mm from the notch is tracked through the simulation. This location is identical to that used to gather the experimental displacement data presented. The vertical load found at the bottom roller as a function of the displacement of the lower adherend is plotted in Figure 5-20. Because of symmetry, twice the vertical reaction force found on the bottom roller is used.

The resulting finite element load versus displacement plot is compared to the experiment load versus displacement plot in Figure 5-20. The experimental data shows the bottom

adherend separating from the top adherend at about a vertical displacement of 2 mm and a load of approximately 155 N, which is observed as a slight dip in the plot. The model correctly predicts the separation of the bottom adherend occurring at about 150 N, while slightly under-predicting the vertical displacement that occurs before it reaches this strength. This is primarily due to the model being an elastic-perfectly plastic model. If the hardening of the adhesive is taken into account, it's quite possible that the model would more closely predict the experimental results.

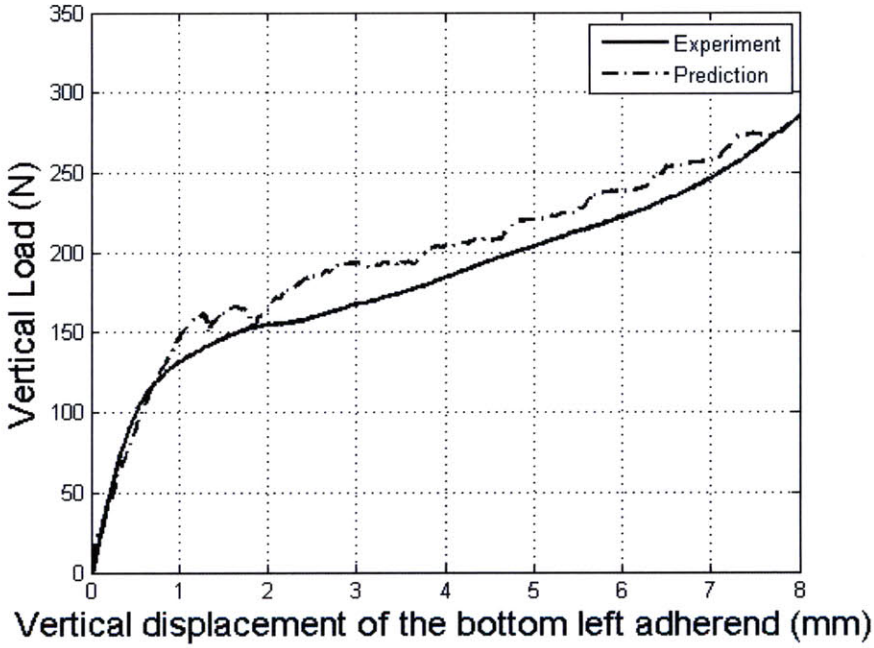

Figure 5-20: Vertical load as a function of vertical displacement for four point bend geometry

The numerical prediction of deformed shape of the half model at the displacement of 8 mm in the bottom adherend is shown in Figure 5-21. A comparison of the deformed shape of the mirrored finite element model is shown in comparison to that of the experiment in Figure 5-22. One can see, the constitutive model is able to make a good prediction of the deformed shape of the specimen.

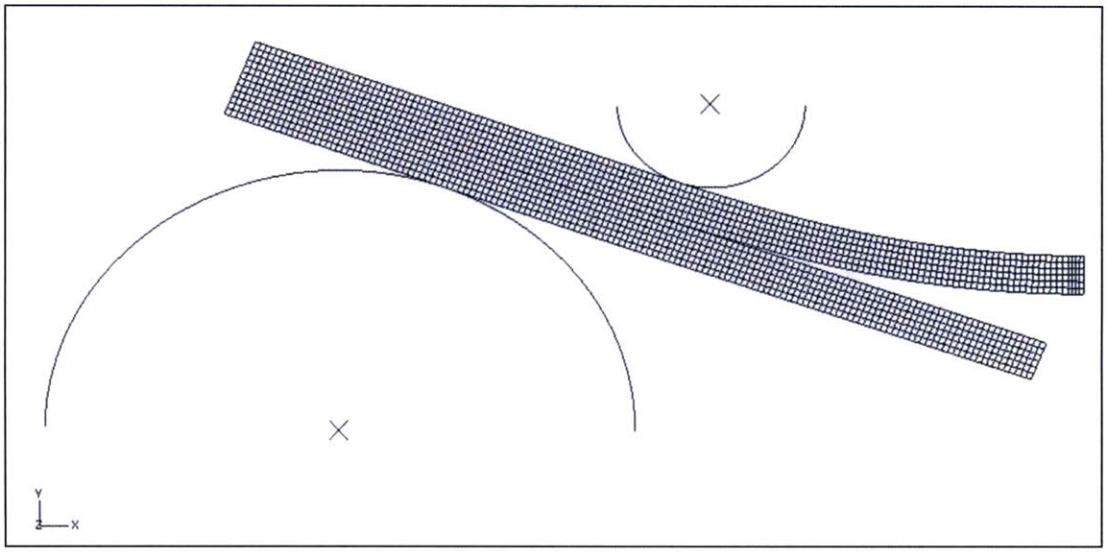

Figure 5-21: Deformed half model

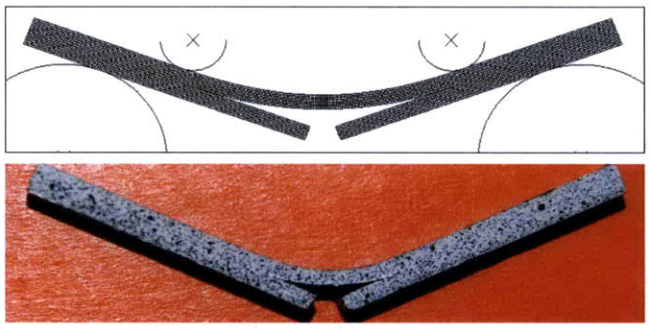

(a)

(b)

Figure 5-22: Deformation of notched four point bend (a) finite element model and (b) experiment

5.3 Chapter Summary

The constitutive model presented in Chapter 3 for a rate independent elastic-plastic model of an adhesive interface subjected to combined normal and shear loading has been successfully used to predict the behavior of the adhesive interface for different geometries. We are able to capture some of the major features of the load-displacement behavior of a curvilinear geometry tested at both a 90° applied angle and a 35° applied angle. Furthermore, we are able to accurately predict the load of initial separation of the adhesive interface in a notched four point bend geometry and get a good qualitative match of deformed shape of the experiment.

Chapter 6

Rate Dependent Interface Constitutive Model

In addition to the rate independent constitutive model presented in Chapter 3, a rate dependent model can be postulated. The following chapter details a rate dependent interface constitutive model for adhesive joints subjected to combined normal and shear loading.

6.1 Interface Definitions

As in the rate independent theory, our adhesive system is comprised of two bodies $\mathcal{B}^+$ and $\mathcal{B}^-$ separated by an interface $\mathcal{I}$ illustrated in Figure 6-1.

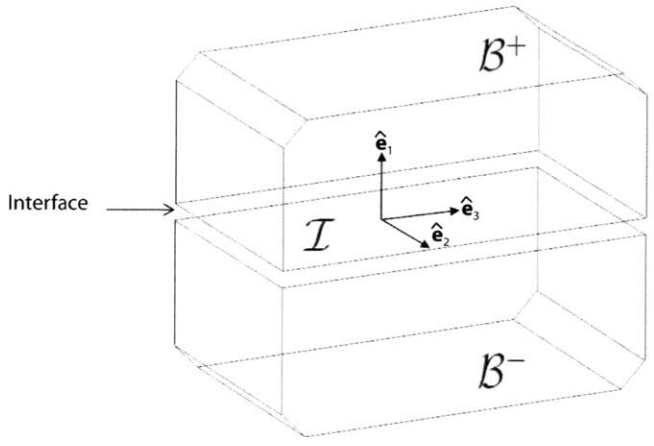

Figure 6-1: Illustration of adhesive system

Let $\{\hat{\mathbf{e}}_1, \hat{\mathbf{e}}_2, \hat{\mathbf{e}}_3\}$ be an orthonormal triad, with $\hat{\mathbf{e}}_1$ aligned with the normal $\mathbf{n}$ to the interface, and $\{\hat{\mathbf{e}}_2, \hat{\mathbf{e}}_3\}$ in the tangent plane at the point of the interface under consideration.

At the point under consideration, we let $\boldsymbol{\delta} = \mathbf{u}^+ - \mathbf{u}^-$ denote the displacement jump across the interface as the difference between the displacement of a point on the interface of the upper body, $\mathcal{B}^+$, and a point on the interface of the lower body, $\mathcal{B}^-$.

The displacement jump is assumed to be additively decomposed into elastic, $\boldsymbol{\delta}^e$, and plastic, $\boldsymbol{\delta}^p$, parts:

$$\boldsymbol{\delta} = \boldsymbol{\delta}^e + \boldsymbol{\delta}^p. \tag{6.1}$$

The power-conjugate traction, $\mathbf{t}$, acting on the interface combines with the rate of change of displacement jump yielding the power per unit area of the interface in the reference configuration, $\mathbf{t} \cdot \dot{\boldsymbol{\delta}}$. This too can be decomposed into

$$\mathbf{t} \cdot \dot{\boldsymbol{\delta}} = \mathbf{t} \cdot \dot{\boldsymbol{\delta}}^e + \mathbf{t} \cdot \dot{\boldsymbol{\delta}}^p. \tag{6.2}$$

6.2 Free Energy of the Interface

A free-energy per unit surface area in the reference configuration is denoted by φ. A purely mechanical theory based on the following local energy imbalance that represents the first two laws of thermodynamics under isothermal conditions is considered, where

$$\dot{\varphi} \leq \mathbf{t} \cdot \dot{\boldsymbol{\delta}}. \tag{6.3}$$

Substituting to account for the elastic and plastic contributions,

$$\dot{\varphi} \leq \mathbf{t} \cdot \dot{\boldsymbol{\delta}}^e + \mathbf{t} \cdot \dot{\boldsymbol{\delta}}^p. \tag{6.4}$$

This field equals the dissipation per unit area, Γ,

$$\Gamma = \mathbf{t} \cdot \dot{\boldsymbol{\delta}}^e + \mathbf{t} \cdot \dot{\boldsymbol{\delta}}^p - \dot{\varphi} \geq 0. \tag{6.5}$$

We now assume that the free-energy, φ, is a function only of the elastic displacement jumps by

$$\varphi = \hat{\varphi}(\boldsymbol{\delta}^e). \tag{6.6}$$

Then, by substituting back into Eq. 6.5, $\mathbf{t}$ is found to be

$$\mathbf{t} = \frac{\partial \hat{\varphi}(\boldsymbol{\delta}^e)}{\partial \boldsymbol{\delta}^e}, \tag{6.7}$$

and the remaining inelastic dissipation is

$$\Gamma = \mathbf{t} \cdot \dot{\boldsymbol{\delta}}^p \geq 0. \tag{6.8}$$

For conditions of small elastic displacement jumps in the interface, we assume a simple quadratic free-energy

$$\varphi = \frac{1}{2}\boldsymbol{\delta}^e \cdot \mathbf{K}\boldsymbol{\delta}^e, \tag{6.9}$$

with $\mathbf{K}$ denoting the interface elastic stiffness tensor. Using Eq. 6.7 and the definition given in Eq. 6.9, we derive

$$\mathbf{t} = \mathbf{K}\boldsymbol{\delta}^e = \mathbf{K}(\boldsymbol{\delta} - \boldsymbol{\delta}^p). \tag{6.10}$$

The interface elastic stiffness tensor is a positive definite tensor. The interface model is taken to be isotropic in the tangential response, thus $\mathbf{K}$ takes the form

$$\mathbf{K} = K_N \mathbf{n} \otimes \mathbf{n} + K_T(\mathbf{1} - \mathbf{n} \otimes \mathbf{n}). \tag{6.11}$$

The normal elastic stiffness is defined $K_N > 0$ and the tangential elastic stiffness is defined $K_T > 0$.

The interface traction $\mathbf{t}$ is additively decomposed into normal and tangential parts, $\mathbf{t}_N$ and $\mathbf{t}_T$, respectively, as

$$\mathbf{t} = \mathbf{t}_N + \mathbf{t}_T, \tag{6.12}$$

where

$$\mathbf{t}_N \equiv (\mathbf{n} \otimes \mathbf{n})\ \mathbf{t} = (\mathbf{t} \cdot \mathbf{n})\ \mathbf{n} \equiv t_N\, \mathbf{n} \tag{6.13}$$

$$\mathbf{t}_T \equiv (\mathbf{1} - \mathbf{n} \otimes \mathbf{n})\ \mathbf{t} = \mathbf{t} - \mathbf{t}_N = \mathbf{t} - t_N\, \mathbf{n}. \tag{6.14}$$

Here, the magnitude of normal traction $\mathbf{t}_N$ is the normal stress t_N and the magnitude of the tangential traction $\mathbf{t}_T$ is the shear stress defined by $\bar{\tau} \equiv \sqrt{\mathbf{t}_T \cdot \mathbf{t}_T}$.

6.3 Flow Rule

The quantity $\boldsymbol{\delta}^p$ evolves according to a flow rule, which is taken to represent the sum of the contribution from both the normal and shear mechanisms. Herein, the index $i = 1$ is defined as the normal mechanism and the index $i = 2$ as a shear mechanism. The flow rule is

$$\dot{\boldsymbol{\delta}}^p = \sum_{i=1}^{2} \nu^{(i)} \mathbf{m}^{(i)}, \qquad \nu^{(i)} \geq 0, \quad \text{with} \tag{6.15}$$

$$\mathbf{m}^{(1)} = \mathbf{n}, \qquad \nu^{(1)} = {\nu_0}^{(1)} \left\{ \frac{< t_N >}{s^{(1)}} \right\}^{\frac{1}{m^{(1)}}}, \tag{6.16}$$

$$\mathbf{m}^{(2)} = \frac{\mathbf{t}_T}{\bar{\tau}}, \qquad \nu^{(2)} = {\nu_0}^{(2)} \left\{ \frac{\bar{\tau}}{s^{(2)} - \mu t_N} \right\}^{\frac{1}{m^{(2)}}}, \tag{6.17}$$

where $< x >$ denotes the bracket function

$$< x >= \begin{cases} 0 & \text{if } x \leq 0, \\ x & \text{if } x > 0 \end{cases} \tag{6.18}$$

and inelastic rate of deformation, $\nu^{(i)}$. The scalar internal variable $s^{(1)}$ represents the deformation resistance for the normal mechanism, and $s^{(2)}$ represents the deformation resistance for the shear mechanism. As seen in the rate independent theory, the scalar variable μ represents a friction coefficient for the shear mechanism. The parameter ${\nu_0}^{(i)}$ represents a reference inelastic relative displacement rate, and the parameter $0 < m^{(i)} \leq 1$ represents a strain rate sensitivity. The limit $m \rightarrow 0$ corresponds to the rate independent limit, and $m^{(i)} \rightarrow 1$ to the linearly viscous limit.

6.4 Constitutive Equations for Deformation Resistance

We let the equivalent relative plastic displacements for the normal and shear mechanisms be defined by $\gamma^{(1)} \stackrel{\text{def}}{=} \int_0^t \nu^{(1)}(\xi)\, d\xi$ and $\gamma^{(2)} \stackrel{\text{def}}{=} \int_0^t \nu^{(2)}(\xi)\, d\xi$, respectively. The traction-separation behavior of the constitutive interface model is depicted in Figure 6-2. The interface, in both directions, deforms elastically until it reaches the initial strength values of ${s_0}^{(1)}$ and ${s_0}^{(2)}$. While both the normal and shear mechanisms showed strain hardening characteristics, an elastic perfectly-plastic traction-separation model will be used as a first approach. The interface is perfectly plastic until reaching a critical displacement jump. Once reaching a critical displacement jump, ${\gamma_{cr}}^{(i)}$, the traction decreases linearly until reaching a failure displacement jump, ${\gamma_f}^{(i)}$. (The traction-separation curve in the shear direction assumes a constant value of t_N.)

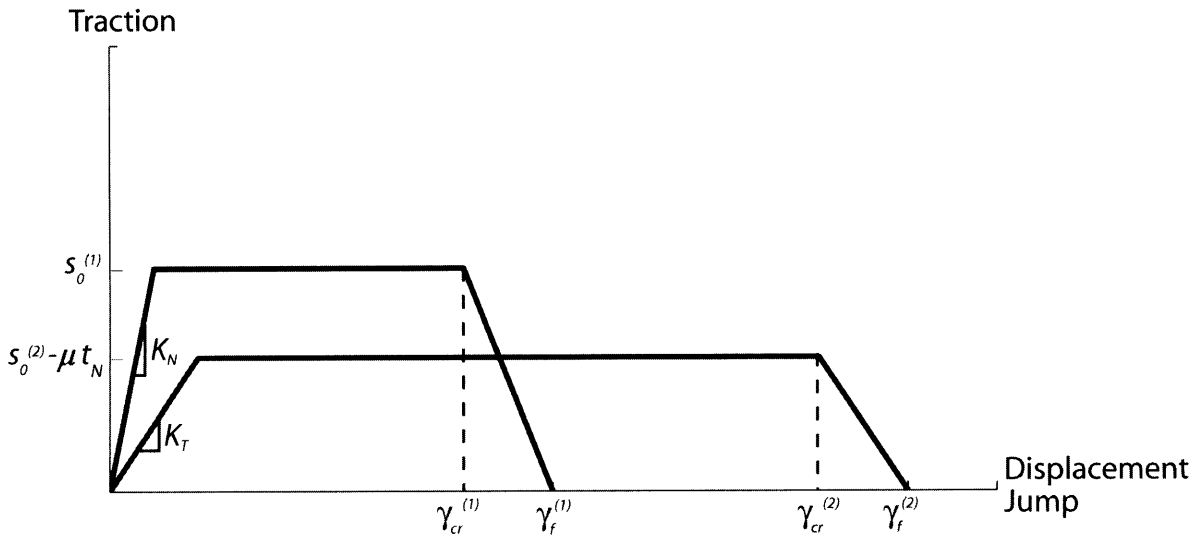

Figure 6-2: Traction-separation behavior for interface under monotonic loading

6.4.1 Rate Dependent Combined Normal and Shear Loading

As seen in the rate independent model, the initial resistance to deformation is a function of the displacement jump angle, θ_δ, found at the interface equal to

$$\theta_\delta = \arctan\left(\frac{\delta^{(1)}}{\delta^{(2)}}\right) \qquad \text{for } \delta^{(1)} > 0, \qquad \delta^{(2)} > 0. \tag{6.19}$$

The constitutive equation for the rate dependent deformation resistance, $s^{(i)}$, for both mechanisms is the same as the rate independent theory.

$$s^{(i)} = \hat{s}^{(i)}\left(\theta_\delta\right), \tag{6.20}$$

$$\text{with} \qquad \hat{s}^{(i)}\left(\theta_\delta\right) = \begin{cases} s_0^{(i)}\left(\theta_\delta\right) & \text{if } \gamma^{(i)} \le {\gamma_{cr}}^{(i)}, \\ s_0^{(i)}\left(\theta_\delta\right) \dfrac{{\gamma_f}^{(i)} - \gamma^{(i)}}{{\gamma_f}^{(i)} - {\gamma_{cr}}^{(i)}} & \text{if } {\gamma_{cr}}^{(i)} < \gamma^{(i)} \le {\gamma_f}^{(i)}. \end{cases} \tag{6.21}$$

The material parameters of the model are the normal and tangential stiffness, K_N and K_T, the initial normal and shear strength, ${s_0}^{(1)}$ and ${s_0}^{(2)}$, the normal and shear critical displacement jump, ${\gamma_{cr}}^{(1)}$ and ${\gamma_{cr}}^{(2)}$, and the normal and shear failure displacement jump, ${\gamma_f}^{(1)}$ and ${\gamma_f}^{(2)}$.

Chapter 4 detailed the exact forms for the dependence of the initial strength on jump angle, ${s_0}^{(i)}(\theta_\delta)$, and the dependence of the critical displacement jump in the shear mechanism, ${\gamma_{cr}}^{(2)}(\theta_\delta)$, on displacement jump angle.

The material parameters for the rate dependent model of each mechanism are the reference inelastic strain rate $\nu_0^{(i)} > 0$ and the rate sensitivity parameter, $m^{(i)} > 0$. Exact material parameters found for this study and the strain rate dependence of the critical displacement jump in the normal mechanism, ${\gamma_{cr}}^{(1)}(\nu^{(1)})$, are detailed in Chapter 7.

6.5 Chapter Summary

We have now delineated the constitutive framework for the description of the adhesive interface when subjected to combined normal and shear loading, while also accounting for rate dependency. The next chapter will detail the specific forms found for the rate dependent constitutive model.

Chapter 7

Rate Dependent Model Calibration

The following chapter details the calibration of the rate dependent constitutive model for adhesive interfaces subjected to combined normal and shear loading. The material parameters dependent on displacement jump angle are identical to the rate independent model and are presented in Chapter 4. The specific forms for quantities dependent on inelastic strain rate are presented, and the calibrated fit is presented in comparison to experimental results.

7.1 Rate Dependent Parameter Calibration and Results

As discussed in Chapter 6, the power law model is used to account for the rate dependent behavior of the adhesive. If we invert Eq. 6.16 and Eq. 6.17 and assume $\mu = 0$, the equations for stress in the rate dependent model are:

$$t_N = s^{(1)}(\theta_\delta) \left\{ \frac{\nu^{(1)}}{\nu_0{}^{(1)}} \right\}^{m^{(1)}}, \tag{7.1}$$

$$\bar{\tau} = s^{(2)}(\theta_\delta) \left\{ \frac{\nu^{(2)}}{\nu_0{}^{(2)}} \right\}^{m^{(2)}}. \tag{7.2}$$

where $\nu_0^{(i)}$ is a reference strain rate greater than zero, $m^{(i)}$ is the rate sensitivity parameter greater than zero, and the form of $s^{(i)}(\theta_\delta)$ is shown in Eq. 6.21. Recall from the experimental results presented in Chapter 2 that the normal critical displacement jump was seen to have

a dependence on strain rate in addition, a power law model is used to capture this behavior:

$$\gamma_{cr}{}^{(1)}(\nu^{(1)}) = \gamma_{cr}{}^{(1)}|_{90^\circ} \left\{ \frac{\nu^{(1)}}{\nu_0^{(1)}} \right\}^{q^{(1)}}, \tag{7.3}$$

where $\gamma_{cr}{}^{(1)}|_{90^\circ} = 0.27$ is the critical displacement jump for the adhesive tested in the normal direction. The failure displacement jump for the adhesive tested in tension is 0.35, consequently, the normal failure displacement jump is set to follow

$$\gamma_f{}^{(1)}(\nu^{(1)}) = \gamma_{cr}{}^{(1)}(\nu^{(1)}) + 0.08 \tag{7.4}$$

The rate dependent parameters calibrated for the normal response of the interface are found in Table 7.1 and those for the shear response are found in Table 7.2.

Table 7.1: Normal rate dependent properties of adhesive interface

Property	Value
$\nu_0^{(1)}$	0.00196
$m^{(1)}$	0.0902
$q^{(1)}$	0.1739

Table 7.2: Shear rate dependent properties of adhesive interface

Property	Value
$\nu_0^{(2)}$	0.00198
$m^{(2)}$	0.0996

The fit of the rate dependent parameters described in Section 7.1 against the experimental results can be seen for the adhesive loaded in the normal direction in Figure 7-1 and for the adhesive loaded in the shear direction in Figure 7-2. We are able to fairly well fit the initial strength of the adhesive and the critical and failure displacement jumps.

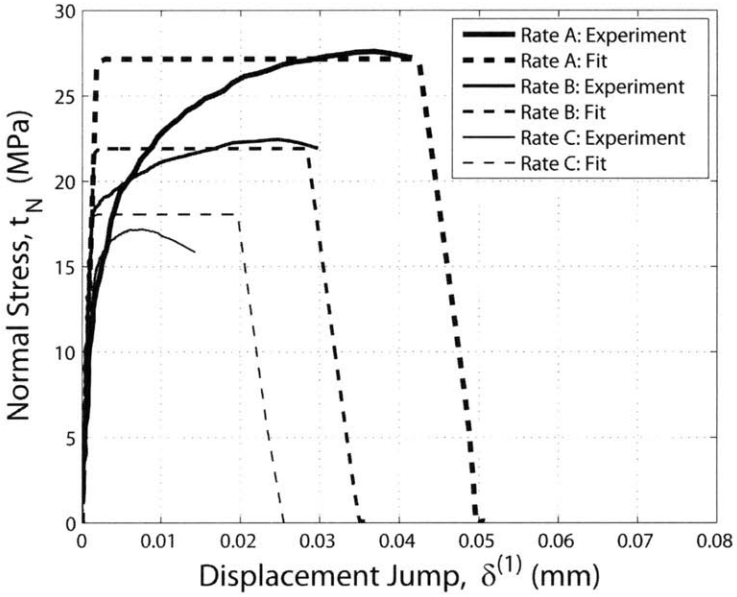

Figure 7-1: Fit of traction-separation behavior of adhesive tested in normal direction. Rate A = 0.571 x 10^{-2}, Rate B = 0.527 x 10^{-3}, Rate C = 0.584 x 10^{-4}

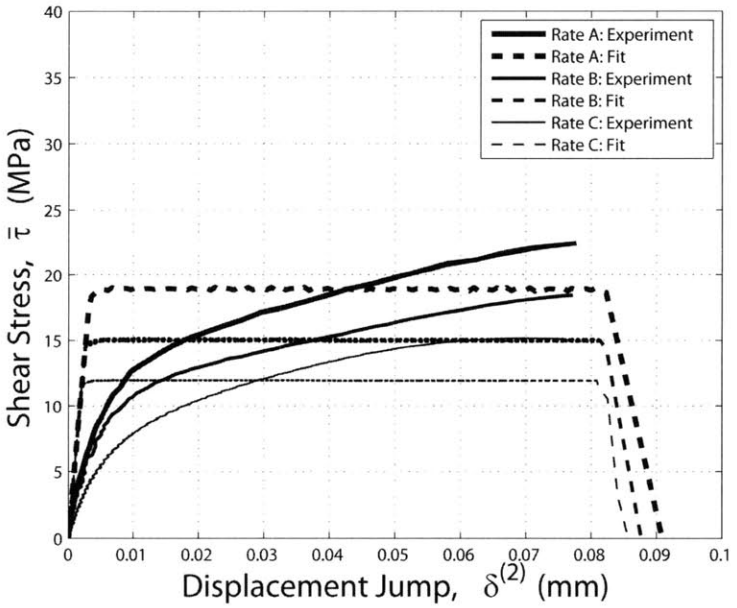

Figure 7-2: Fit of traction-separation behavior of adhesive tested in shear direction. Rate A = 0.717 x 10^{-1}, Rate B = 0.698 x 10^{-2}, Rate C = 0.754 x 10^{-3}

7.2 Chapter Summary

The rate dependent constitutive model for the adhesive interface has been calibrated to the combined normal and shear loading experiments and the rate dependent experiments that have been performed. However, the numerical implementation of the rate dependent constitutive model and further validation experiments testing the robustness of the model still need to be carried out.

Chapter 8

Concluding Remarks

The current study has detailed a successful comprehensive series of biaxial experiments performed under combined loading conditions. An elastic-plastic interface constitutive model that accounts for combined normal and shear loading at the interface has been developed and implemented. Numerical implementation of the constitutive model was accomplished through the user subroutine, VUINTER, of the commercially available finite element code ABAQUS/Explicit. The fit using the numerical implementation of the constitutive model has been tuned to the experimental results of the combined loading tests performed on butt joint specimens, and applications of the constitutive model were explored through two geometries with good results. The macroscopic load versus displacement jump of bonded curvilinear blocks subjected to two different applied loading angles has been successfully predicted. The predictions come fairly close to experimental results, with differences being in a slight under-prediction in displacement jump angle at the interface which leads to an over-prediction in the horizontal load seen during experimentation. Also, the load-displacement results of a notched four point bend specimen under a constant displacement rate has been well predicted. For this case, the load at which the crack is initiated is well predicted, with a slight under-prediction of the displacement at which it occurs.

Furthermore, a rate dependent elastic-plastic interface constitutive model for combined normal and shear loading has been presented. The material parameters of the power law model chosen have been found for the experiments performed on the adhesive interface tested in the normal and shear directions at various rates.

8.1 Future Work

The next step in the current study would be to successfully develop the time-integration procedure and numerically implement the rate dependent constitutive model. Additional validation experiments should also be performed to test the robustness of the model. Cur-

rently it is assumed that the rate dependent combined loading behavior of the adhesive interface can be calibrated using the two pure mechanisms. This could be confirmed by testing the same butt joint specimen in the biaxial testing apparatus for a combined normal and shear loading case at a different displacement rate than the calibrated experiments already performed.

The comprehensive combined loading experiments were to initially test the adhesive interface at the nominal angles discussed in Chapter 2. During the data reduction of the calibration experiments, it was observed that the applied loading angle at the grips deviated from the nominally applied angle programmed into the biaxial testing apparatus controller. This resulted in the actual applied angles ranging from 7.0° to 50.4°, instead of the intended 10° to 60°. Additional applied angles between 60° and 90° should be investigated to complete a thoroughly exhaustive analysis.

A current limitation of the model is in its application to monotonic loading conditions. Only constantly applied displacement rates have been used for the calibration and validation experiments. Consequently, the current numerical implementation has been designed to calculate the displacement jump angle only once at the beginning of the explicit time integration. Modifications can be made to the numerical implementation to allow for dynamic macro level displacement rates, and the displacement jump angle could be calculated throughout.

Additionally, the current calibrated constitutive model assumes a frictional coefficient of zero. Separate combined compressive and shear experiments should be performed on the adhesive interface to see what role the coefficient of friction plays.

The current model also assumes an elastic-perfectly plastic adhesive interface. The constitutive model could be modified to include strain rate hardening and softening parameters similar to those presented by Su et al. [5]. If more detailed inelastic behavior is included in the model, the predictions would likely improve.

Finally, the model could be applied to other interesting combined normal and shear loading experimental geometries. For example, an ASTM standard test exists for Mixed Mode I-Mode II interlaminar fracture toughness and details a testing approach called Mixed Mode Bending (MMB) that could be applied to aluminum/adhesive/aluminum systems [11].

Appendix A

Literature Review

The elastic-plastic constitutive model of the current study presented in Chapter 3 draws from the cohesive zone model for elastic-plastic fracture mechanics. The following appendix briefly summarizes the cohesive zone model and its origins in Dugdale's strip yield model, an elastic fracture problem. The appendix then details three applications of the model in the area of numerical and experimental studies of adhesive interfaces. Mathematical characters and definitions in this appendix mimic those used by the original authors of the works cited.

A.1 Cohesive Zone Model

The following section is a short introduction and summary of the cohesive zone model. It is a summary of the presentation on the subject by Zehnder [12] and Hutchinson [13].

A.1.1 Strip Yield Model

The elastic fracture problem of failure seen in thin metal sheets was originally modeled by Dugdale [2] in 1960 with his coined strip yield model. Here the model can be applied to ductile fracture and it helps to highlight the limitations of small scale yielding [12]. The strip yield model asks one to consider a finite crack of size $2a$ in tension.

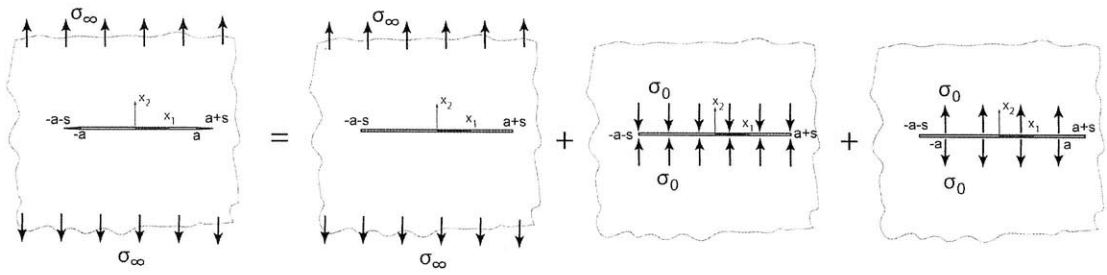

Figure A-1: Crack of length $2a$ in infinite plate with tensile loading of $\sigma_{22}=\sigma_\infty$ and strip yield zone with yield stress σ_0 of length s at each crack tip. Yield zone problem can be solved by superposition of the solutions of the three problems. [12]

The material is assumed to deform plastically along the length of the crack in very thin zones of length s. The stress is governed by the uniaxial yield stress σ_0 of the material within the zones s.

The length of the yield zones (s) are determined to be finite which will lead to the determination of the stress fields and "crack opening displacement" or COD. This problem is treated as one of superposition of three problems (see Figure A-1):

(i) a crack loaded in tension of length $2(a+s)$

(ii) a crack with closing tractions σ_0 of length $2(a+s)$

(iii) a crack with opening tractions over $|x_1| < a$

The stress intensity factor is set to zero and the value of s is solved for. The total stress intensity factor is $K_I = K_I^{(i)} + K_I^{(ii)} + K_I^{(iii)}$ where

$$K_I^{(i)} = \sigma_\infty \sqrt{\pi\,(a+s)} \tag{A.1}$$

$$K_I^{(ii)} = -\sigma_0 \sqrt{\pi\,(a+s)} \tag{A.2}$$

$$K_I^{(iii)} = 2\sigma_0 \sqrt{\frac{a+s}{\pi}} \sin^{-1} \frac{a}{a+s} \tag{A.3}$$

The resulting length s of the yield zone is found to be

$$s = a \sec\left(\frac{\pi\sigma_\infty}{2\sigma_0}\right) - a \tag{A.4}$$

This leads to the stress field ahead of the crack tip as shown in Figure A-2. Tension experiments in thin sheets of steel with edge and internal center cracks were performed by Dugdale [14] and a very good match was found between the results and the predicted theoretical value of s, as shown in Figure A-3.

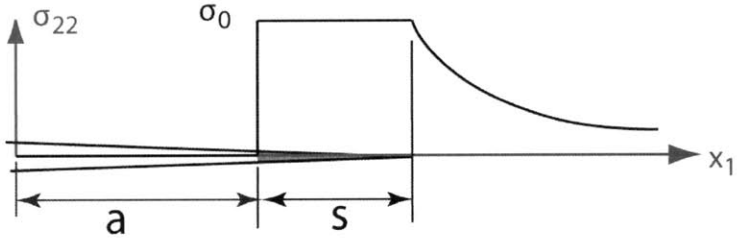

Figure A-2: Stress ahead of the crack tip is finite due to strip yield zone. [12],[2]

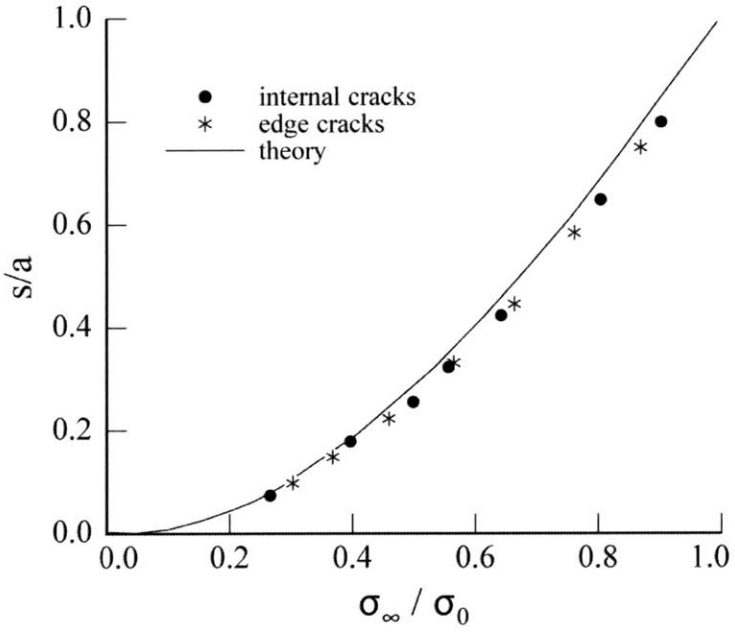

Figure A-3: Dugdale's experimental results for steel sheets showing normalized plastic zone length versus applied tension stress [12]

The crack opening displacements are found with superposition. The displacement solution for problem (i) plus (ii) is found from the Westergaard [15] approach using complex variables to describe the stress for mode-I:

$$u_2^{(i+ii)}\left(x_1, 0^{(+)}\right) = (\sigma_\infty - \sigma_0)\,\frac{\kappa+1}{4\mu}\sqrt{(a+s)^2 - x_1^2} \tag{A.5}$$

The displacement solution for problem (iii) is found by using the general solution for internal crack with applied tractions with $p_2 = \sigma_0$ for $|x_1| < a$ and $z = x_1$,

$$\phi' = \frac{1}{\pi\sqrt{z^2 - (a+s)^2}} \int_{-a}^{a} \sigma_0 \frac{\sqrt{(a+s)^2 - t^2}}{z - t} dt \tag{A.6}$$

$$2\mu u_2 = \frac{\kappa + 1}{2} \mathrm{Im}\phi \tag{A.7}$$

$$u_2^{(iii)}\left(x_1, 0^{(+)}\right) = \frac{\kappa+1}{4\mu}\frac{\sigma_0}{\pi}\mathrm{Im}\int_{a+s}^{x_1} \frac{1}{\sqrt{z^2 - (a+s)^2}} \int_{-a}^{a} \frac{\sqrt{(a+s)^2 - t^2}}{z - t} dt\, dz \tag{A.8}$$

Using Eq. A.1.1 and integrating the equation above, the total crack mouth displacement[13] is found to be

$$\delta_T \equiv u_2\left(a, 0^{(+)}\right) - u_2\left(a, 0^{(-)}\right) = \frac{8}{\pi}\frac{\sigma_0}{E} a \ln\left[\sec\frac{\pi\sigma_\infty}{2\sigma_0}\right] \tag{A.9}$$

The J-integral can be calculated by recalling that $J = \int_\Gamma \left(W n_1 - t_i u_{i,1}\right) d\Gamma$. The integration contour, Γ, can be shrunk down to the yield zone as shown in Figure A-4, where on $\Gamma^{(+)}$ $n_1 = 0$, $n_2 = 1$, $t_1 = 0$, $t_2 = \sigma_0$ and $d\Gamma = -dx_1$ [12]. On $\Gamma^{(-)}$ $n_1 = 0$, $n_2 = -1$, $t_1 = 0$, $t_2 = -\sigma_0$ and $d\Gamma = dx_1$. The term $t_i u_{i,1}$ in the J integral becomes $\pm\sigma_0 u_{2,1}$ and $W n_1$ is zero resulting in

$$J = \int_a^{a+s} \sigma_0 u_{2,1}^{(-)}(x_1)\, dx_1 + \int_{a+s}^{a} -\sigma_0 u_{2,1}^{(+)}(x_1)\,(-dx_1) \tag{A.10}$$

$$= \sigma_0\left[u_2^{(-)}(a+s) - u_2^{(-)}(a) + u_2^{(+)}(a) - u_2^{(+)}(a+s)\right] \tag{A.11}$$

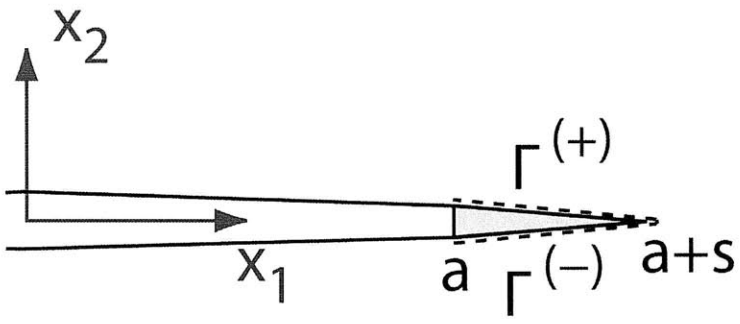

Figure A-4: Path Γ for J contour integral for strip yield zone problem [12]

Setting the terms of $u_2(a+s) = 0$, $u_2^{(+)}(a) = {}^{\delta_T}/_2$ and $u_2^{(-)}(a) = -{}^{\delta_T}/_2$, and making use of Eq. A.9 the J-integral simplifies to

$$J = \sigma_0 \delta_T \tag{A.12}$$

$$J = \frac{8}{\pi}\frac{\sigma_0^2}{E} a \ln\left[\sec\frac{\pi\sigma_\infty}{2\sigma_0}\right] \tag{A.13}$$

We can determine when small scale yielding applies by solving the full solution for when $s \ll a$ and using $K_I = \sigma_\infty\sqrt{\pi a}$

$$s \approx a\frac{\pi^2}{8}\left(\frac{\sigma_\infty}{\sigma_0}\right)^2 = \left(\frac{K_I}{\sigma_0}\right)^2\frac{\pi}{8} \tag{A.14}$$

$$\delta_T \approx \frac{a\sigma_\infty^2\pi}{E\sigma_0} \tag{A.15}$$

$$J = \sigma_0\delta_T \approx \frac{a\pi\sigma_\infty}{E} = \frac{K_I^2}{E} \tag{A.16}$$

We can clearly see from Equation A.16 that the relationship between J and K_I for small scale yielding, when $s \ll a$, is the same as the small scale yielding result in the purely elastic case for plane stress where $G = J = {}^{K_I^2}/_E$.

The small scale yielding case is valid in comparison to the full solution when the size of the plastic zone s is less than approximately 20% of the crack length a.

A.1.2 Cohesive Zone Model

The cohesive zone model pioneered by Barenblatt [1] is a modified Dugdale [2] strip yield model in which the stresses in the yield zone ahead of the crack are not just a constant value but are a function of the displacement across the yield zone. A description of the model can be found in Zehnder [12] and a summary of the derivation is shown below. The key parameters of the cohesive zone model are the cohesive strength *(peak stress)*, $\hat{\sigma}$, and the energy Γ_0.

A generalized mode-I traction-separation law for the cohesive zone model is shown in Figure A-5. The displacement across the crack, assuming tension in the x_2 direction is $\delta \equiv u_2^+ - u_2^-$ and the critical displacement at failure is δ_C. The maximum cohesive strength is $\hat{\sigma}$. The energy is the area under the traction-separation curve:

$$\Gamma_0 = \int_0^{\delta_C} \sigma(\delta)\, d\delta \tag{A.17}$$

A schematic of the contour Γ can be seen in Figure A-6 [12]. The calculated J-integral for the cohesive zone model, on the contour Γ when $n_1 = 0$ is

$$J = -\int_{\Gamma} t_i \frac{\partial u_i}{\partial x_1} d\Gamma \tag{A.18}$$

$$= -\int_{c.z.} \sigma(\delta) \frac{\partial \delta}{\partial x_1} dx_1 = -\int_{c.z.} \frac{\partial}{\partial x_1} \left[\int_0^{\delta} \sigma(\delta)\, d\delta \right] dx_1 \tag{A.19}$$

$$= \int_0^{\delta_T} \sigma(\delta)\, d\delta \tag{A.20}$$

The crack opening at the crack tip is δ_T and if loaded to fracture, $\delta_T = \delta_C$, resulting in

$$J = \int_0^{\delta_C} \sigma(\delta)\, d\delta = \Gamma_0 \tag{A.21}$$

The area under the traction-separation curve is the energy required to propagate the crack, sometimes called toughness or the work of separation per unit area.

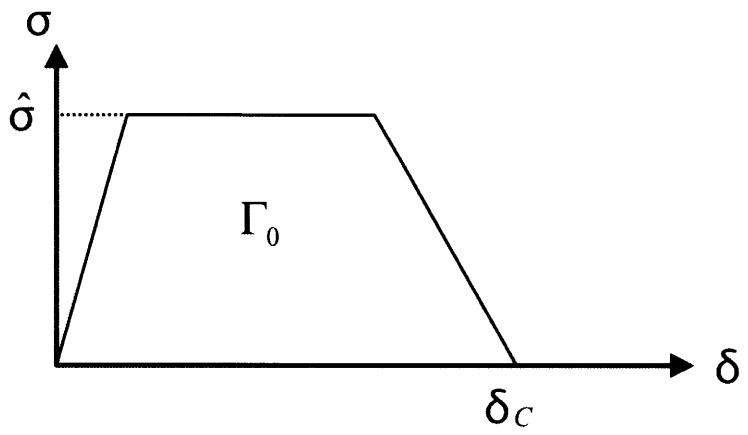

Figure A-5: The nonlinear traction-separation law ahead of the crack. [12]

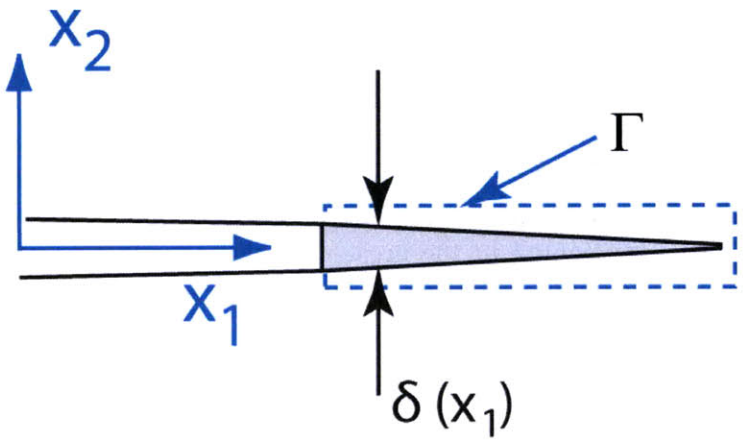

Figure A-6: Traction-separation boundary. [12]

If the cohesive zone model is used for an elastic-plastic material, the fracture energy flux is the total of the energy release rate and the dissipation in the plastic zone at the crack tip. The energy of elastic-plastic crack growth comes from the energy of plastic dissipation in the plastic zone. Normally Γ_0 (energy absorbed by the local failure) is small in comparison to the energy dissipated by plastic deformation. The cohesive energy and strength control dictate the extent of plastic deformation and thus control the fracture energy. The sum of the cohesive energy and the dissipation of plastic energy, $\mathbf{\Phi}_p$, totals the fracture energy. This can be seen in Figure A-7, where

$$G_{ss} = \Gamma_0 \qquad \hat{\sigma} \leq \eta\sigma_0 \tag{A.22}$$

$$G_{ss} = \Gamma_0 + r_p\mathbf{\Phi_p} \qquad \hat{\sigma} \geq \eta\sigma_0 \tag{A.23}$$

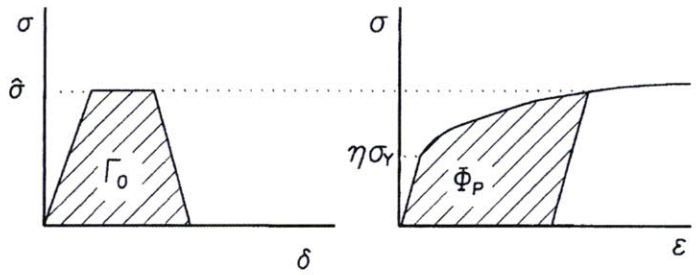

Figure A-7: The energy dissipated during crack growth is modeled as the sum of the cohesive energy, Γ_0 and the work of plastic deformation, $r_p\mathbf{\Phi_p}$[16]

A.2 Applications of the Cohesive Zone Model: Adhesive Interfaces

This section contains a review of some recent research in the area of numerical analysis and experimentation involving the application of the cohesive zone model to the interface mechanics problem of adhesive interfaces. The review is to illustrate the very wide variety of problems being investigated in the area, as well as illustrating some numerical and experimental challenges involving the cohesive zone model and adhesive interfaces.

A.2.1 Tvergaard and Hutchinson: On the toughness of ductile adhesive joints

Numerical analysis using the cohesive zone model is detailed by Tvergaard and Hutchinson [4]. Here their work applies the embedded fracture zone model to the mode-I fracture of an adhesive joint, continuing work from 1994 [3]. They investigate an elastic-plastic adhesive layer joining two elastic substrates[4]. The model is applied to investigate the influence the elastic mismatch between the adhesive and the substrates has on the joint toughness, as well as determining the influence that any residual stress might have on joint toughness. The following is a summary of their contribution.

The traction-separation law for the interface defines δ_n and δ_t as the normal and tangential components of the relative displacement of the crack faces across the interface. Tvergaard and Hutchinson's definition of this relation is seen in Figure A-8, and a potential from which the tractions are derived is defined as:

$$\Phi\left(\delta_n, \delta_t\right) = \delta_n^c \int_0^{\lambda} \sigma\left(\lambda'\right) d\lambda' \tag{A.24}$$

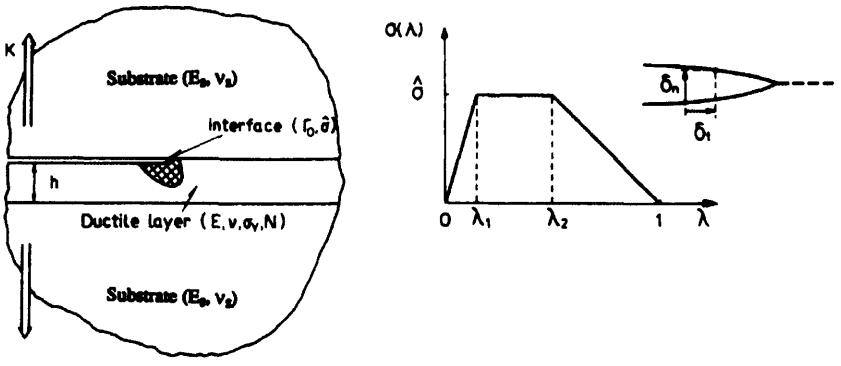

Figure A-8: Geometry of system and traction-separation law for the interface [4]

	Young's Modulus	Poisson's ratio
Adhesive	E	ν
Substrates	E_s	ν_s

Table A.1: Elastic properties of adhesive and substrates

The normal and tangential components of traction acting on the interface are defined as

$$T_n = \frac{\partial \Phi}{\partial \delta_n} = \frac{\sigma(\lambda)}{\lambda} \frac{\delta_n}{\delta_n^c} \tag{A.25}$$

$$T_t = \frac{\partial \Phi}{\partial \delta_t} = \frac{\sigma(\lambda)}{\lambda} \frac{\delta_t}{\delta_t^c} \frac{\delta_n^c}{\delta_t^c}, \tag{A.26}$$

where the single non-dimensional separation measure is $\lambda = \sqrt{\left(\delta_n/\delta_n^c\right)^2 + \left(\delta_t/\delta_t^c\right)^2}$. The critical values of displacement components are δ_n^c and δ_t^c. As mentioned in Section A.1.2, Tvergaard and Hutchinson identify the two most important parameters governing the fracture process of their model as Γ_0 and $\hat{\sigma}$. The work of the fracture process Γ_0 for the separation function $\sigma(\lambda)$ is

$$\Gamma_0 = \frac{1}{2}\hat{\sigma}\delta_n^c \left[1 - \lambda_1 + \lambda_2\right]. \tag{A.27}$$

Tvergaard and Hutchinson assume an isotropic ductile interface (adhesive) with thickness h and two identical and isotropic elastic substrates with properties seen in Table A.1.

The unloaded layer is assumed to have an equibiaxial residual stress state, σ_R, in the direction parallel to the plane of the layer. This residual stress influences the onset of yield when the joint is loaded. The plastic behavior of the adhesive layer material is ruled by the J_2 flow theory and it is given a true stress-true strain relationship as follows:

$$\epsilon = \sigma/E \qquad \text{for } \sigma \leq \sigma_Y \tag{A.28}$$

$$,\epsilon = (\sigma_Y/E)\left(\sigma/\sigma_Y\right)^{1/N} \qquad \text{for } \sigma > \sigma_Y, \tag{A.29}$$

where σ_Y is defined as the tensile yield stress and N is the strain hardening exponent.

Tvergaard and Hutchinson take the asymptotic crack problem shown in Figure A-8 to be semi-infinite and loaded remotely by the symmetric mode I stress field with amplitude K, the stress intensity factor. Therefor, the relationship between the energy release rate G and the stress intensity factor K for mode I, plane strain crack in an elastic solid is given by:

$$G = \frac{(1 - \nu_s^2)}{E_s} K^2. \tag{A.30}$$

Here G is interpreted as the remote or applied energy release rate.

The material length quantity R_0 for mixed mode interface fracture is defined as [17]:

$$R_0 = \frac{2}{3\pi\left(1-\beta^2\right)}\left[\frac{\left(1-\nu^2\right)}{E}+\frac{\left(1-\nu_s^2\right)}{E_s}\right]^{-1}\frac{\Gamma_0}{\sigma_Y^2}, \tag{A.31}$$

with the second Dundurs elastic mismatch parameter β given by

$$\beta = \frac{1}{2}\frac{\mu\left(1-2\nu_s\right)-\mu_s\left(1-2\nu\right)}{\mu\left(1-\nu_s\right)+\mu_s\left(1-\nu\right)}. \tag{A.32}$$

Here shear moduli are μ and μ_s. The quantity R_0 is described as an estimate of the size of the plastic zone of the interface crack when $\Gamma = \Gamma_0$ and the interface thickness $h \gg R_0$.

Next, the model is used to compute the history of the crack growth resistance Γ as a function of crack advance, Δa, as dependent on the system parameters. The steady-state toughness, Γ_{ss}, is defined as the asymptote characterizing the steady-state condition wherein the crack advances under constant Γ, typically several times R_0. The non-dimensional relationship between Γ_{ss} and other model parameters is:

$$\frac{\Gamma_{ss}}{\Gamma_0} = F\left(\frac{\hat{\sigma}}{\sigma_Y}, N, \frac{h}{R_0}, \frac{E_s}{E}, \frac{\sigma_R}{\sigma_Y}\right). \tag{A.33}$$

The parameters shown in Equation A.33 are primarily investigated, except N which is fixed at 0.1 in all computations corresponding to strain hardening.

Finally, a finite element model is created to investigate the dependence of Γ on the model parameters. The numeric specifics can be found in great detail in [3, 4], but are summarized below:

- The displacements in the 1 and 2 directions along the interface between the lower substrate and the layer are set equal to each other.
- The tractions along the interface between the lower substrate and the layer are set equal and opposite to each other in the 1 and 2 directions.
- The displacements and tractions along the upper interface are specified by the traction-separation law described above.
- Elastic-plastic deformations in the layer take place following a finite strain generalization of J_2 flow theory.

Tvergaard and Hutchinson draw the following qualitative results from their study. To summarize:

1. As $\hat{\sigma}/\sigma_Y$ increases, normalized steady-state toughness Γ_{ss}/Γ_0 increases if all other parameters are held fixed
2. If the adhesive layer is thin ($h/R_0 \ll 1$), plastic deformation of the layer does not enhance toughness ($\Gamma_{ss} \cong \Gamma_0$)

3. If the adhesive layer is larger than the plastic zone ($^{h}/_{R_0} \gg 1$) the interaction of the plastic zone with the substrate on the other side of the uncracked interface becomes negligible and $^{\Gamma_{ss}}/_{\Gamma_0}$ becomes independent of h

4. Toughness is increased with increasing ratios of $^{E_s}/_{E}$, seen in Figure A-9.

5. The residual stress in the layer lower the joint toughness if σ_R is in tension and raise the toughness if σ_R is in compression. The residual stress can raise or lower the additional effective stress needed to cause yield.

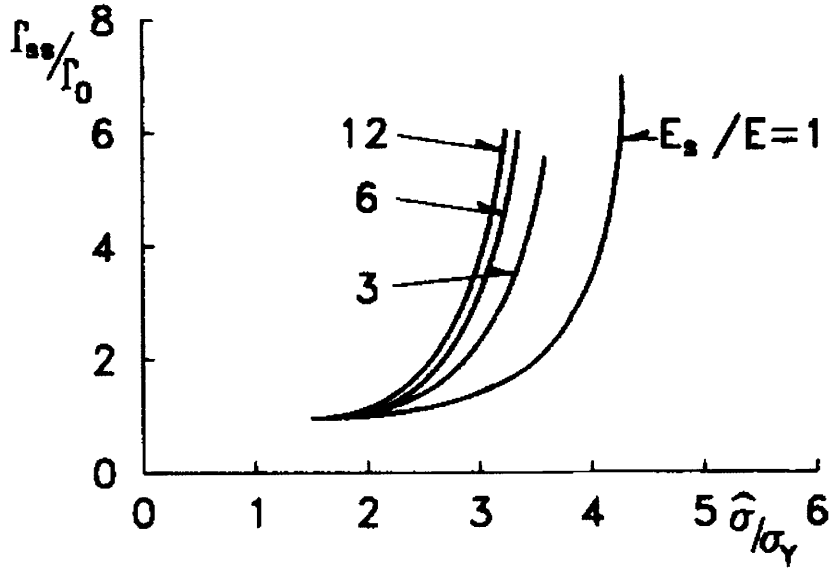

Figure A-9: Dependence of steady-state toughness of the joint on $\hat{\sigma}/\sigma_Y$ for various E_s/E, all for the limit of large h/R_0 for which the layer thickness exceed the height of the plastic zone. [4]

Tvergaard and Hutchinson also determine that the peak interface stress $\hat{\sigma}$ occurs at a distance ahead of the tip due to the constraint the elastic substrates have on the adhesive layer. This peak interface stress causes debonding to occur ahead of the crack tip and unconnected to the crack tip.

Tvergaard and Hutchinson Summary

The work completed by Tvergaard and Hutchinson investigates an elastic-plastic adhesive joint with a fracture process governed by a traction-separation law (the cohesive zone mode). They successfully investigate the effects that layer thickness, layer-substrate modulus mismatch, and layer initial residual stresses have on the steady-state toughness Γ_{ss}.

A.2.2 Sun et al: Ductile-brittle transitions in the fracture of plastically deforming, adhesively bonded structures

Sun, Thouless, Waas, Schroeder, and Zavattieri have published research on ductile-brittle transitions in the fracture of plastically deforming, adhesively bonded structures [18, 19]. This research group at the University of Michigan and General Motors has a primary interest to better understand the fracture process of adhesively bonded structures for applications in the automobile industry. The plastic deformation of automobile structural joints is required to ensure high levels of energy absorption in a crash. Consequently, characterizing the behavior of such joints under various loading rates is of high importance. The following is a summary of their experimental [18] and numerical [19] work on this topic.

Experiments

Sun et al. begin their studies with a paper detailing the experimental work done to determine ductile-brittle transitions in the fracture of plastically-deforming, adhesively-bonded structures [18]. Their primary interest is to delineate a methodology to determine mode I cohesive parameters over a wide range of loading rates. The following tests were completed on a plastically-deforming structure of steel sheets and adhesive.

1. Double Cantilever Beam (DCB) under displacement control
2. Wedge geometry under displacement control
3. Wedge geometry loaded under impact

Two modes of failure were observed:

1. Quasi-static crack growth—a balance between applied energy release rate and the energy dissipated by the crack growth and any plastic deformation
2. Dynamic crack growth—crack growth that occurs when the energy available for crack growth surpasses the energy associated with new crack surface creation and plastic deformation. This can take the form of the crack becoming unstable and advancing dynamically.

One property of dynamic crack growth is what is termed "stick-slip" fracture, where cracks propagate sporadically under steady loading conditions.

Separate tension tests on steel adherends and the neat rubber toughened, one part epoxy-based adhesive, were performed. The tests were performed at various nominal strain rates to characterize constitutive properties of the materials.

DCB tests were performed on the geometry shown in Figure A-10, and details of the test can be found in [18]. The displacement controlled tests were performed at various nominal strain rates, and as seen in Figure A-10b, plastic deformation of the steel arms was observed. Failure of the DCB specimens was due to quasi-static crack growth along the interface or

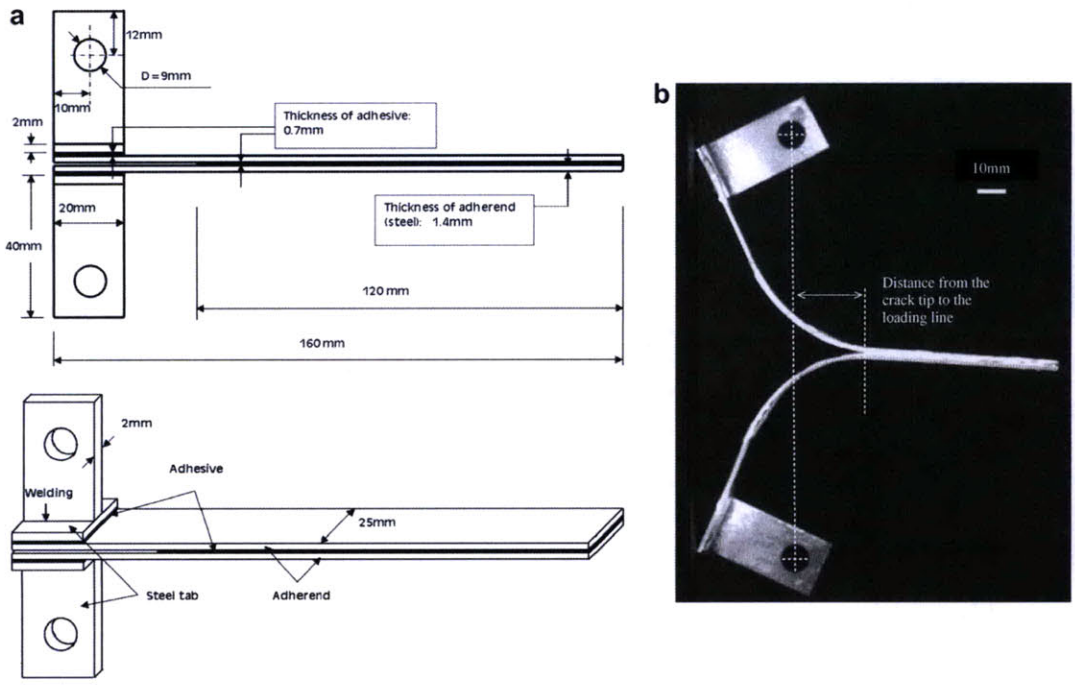

Figure A-10: (a) DCB specimen geometry (b) Deformed DCB specimen [18]

by "stick-slip" behavior where the quasi-static crack growth was sporadically interrupted by dynamic crack failure. Sun et al. were unable to determine a clear critical loading rate that could be associated with the transition from one failure to the other, but they were able to see that transitions to dynamic fracture were less likely at lower loading rates.

Figures A-11a and A-11b are the load-displacement curves for the quasi-static crack growth and the "stick-slip" behavior. From Figure A-11a, it can be seen that for the quasi-static crack growth the loads are fairly constant and independent of strain rate. The quasi-static crack growth data also indicates that loading rate has a negligible effect on the toughness of the bond. Sun et al. were also able to see a linear relationship between crack length and crosshead displacement.

From Figure A-11b, severe drops in the load correspond to a region of dynamic failure. The load curves for this behavior also show a gradual drop in peak load which can be associated with a decrease in plastic deformation due to dynamic fracture. This causes an increase in the distance between the crack tip and the loading line, resulting in a lower load required for quasi-static crack growth. In addition, optical micrographs were taken showing clear differences in quasi-static and dynamic crack growth in the adhesive itself, shown in Figures A-12a and A-12b.

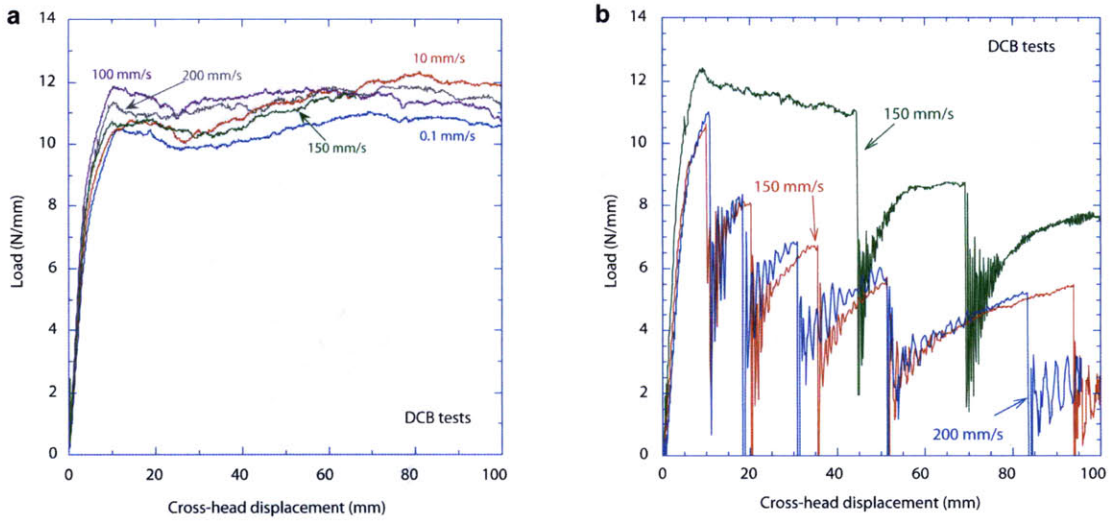

Figure A-11: (a) DCB quasi-static crack growth load displacement curve (b) DCB dynamic crack growth load displacement curve [18]

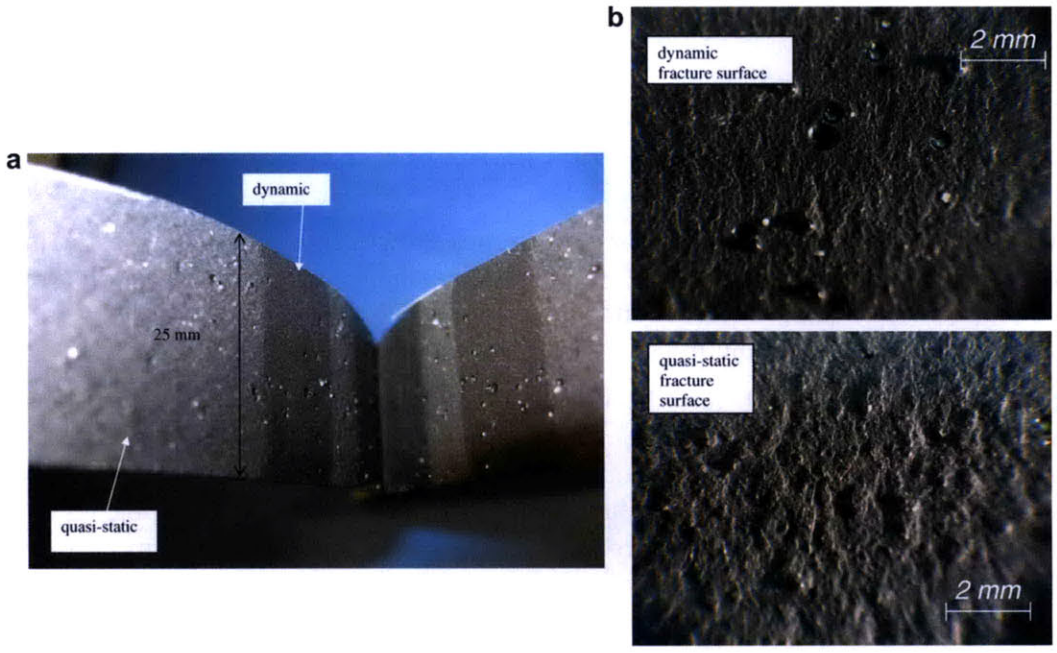

Figure A-12: Optical micrographs of specimen showing (a) quasi-static and dynamic fracture surfaces. (b) Higher-resolution optical micrographs showing smooth dynamic fracture surface and rough quasi-static fracture surface. [18]

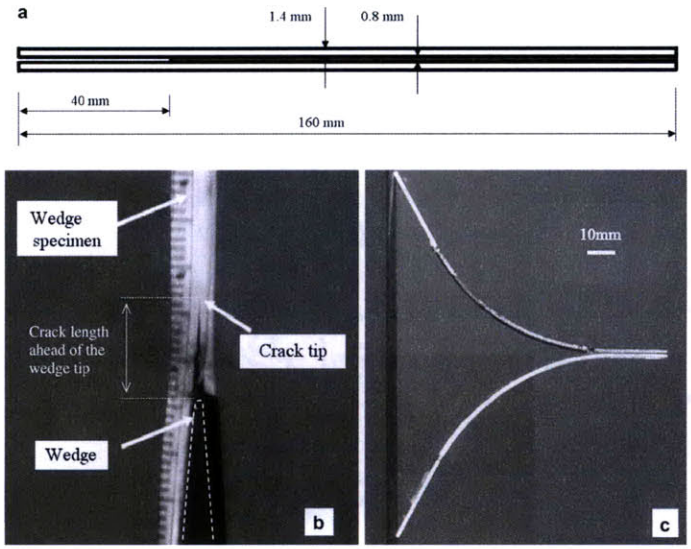

Figure A-13: (a) Displacement controlled wedge test specimen geometry. (b) Wedge test experimental configuration (c)Deformed wedge test specimen (80 mm/s) [18]

Wedge tests under displacement control

The findings of the DCB were replicated in wedge tests under displacement control indicating the behavior is characteristic of the steel/adhesive specimen and not the test geometry. Figure A-13 details the wedge geometry. The wedge tests were displacement controlled and tested at the same rates the DCB tests were conducted. Again, quasi-static crack growth was seen as well as transitions to dynamic crack growth.

Wedge tests under impact

Sun et al. also performed drop-tower tests to achieve higher crack velocities of the same specimen seen in Figure A-13. The behavior of "stick-slip" was observed in all the tests, except one. A plot of the crack extension as a function of time is shown in Figure A-14. In addition, measurements of the distance between the crack tip and the wedge tip were consistent with the data from the displacement controlled wedge tests. Sun et al. conclude that this further proves rate effects for the quasi-static crack growth are negligible.

Sun et al. conclude that the fracture of the adhesive joint occurs in a quasi-static fashion, or toughened mode, and a dynamic fashion, or untoughened mode. The quasi-static crack growth appears to be independent of crack velocity over a large range up to 1000 mm/s. Rate effects in the system are found in the transition from quasi-static crack growth to dynamic fracture.

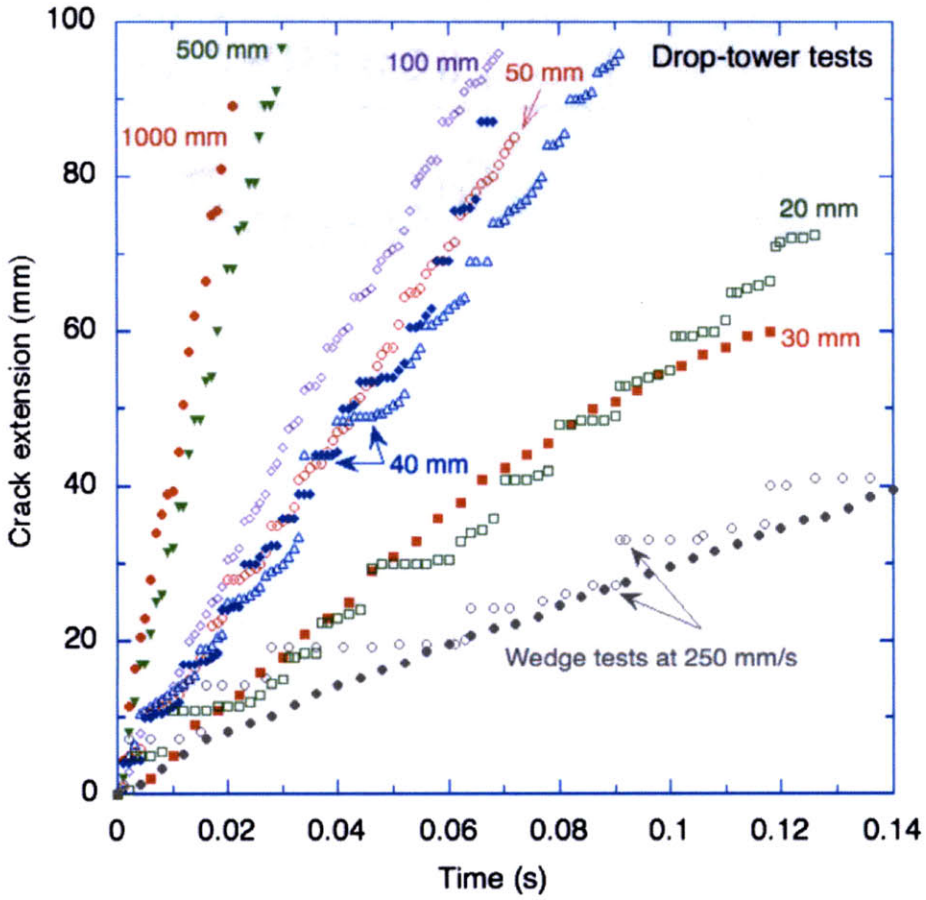

Figure A-14: Wedge test crack extension as a function of time.[18]

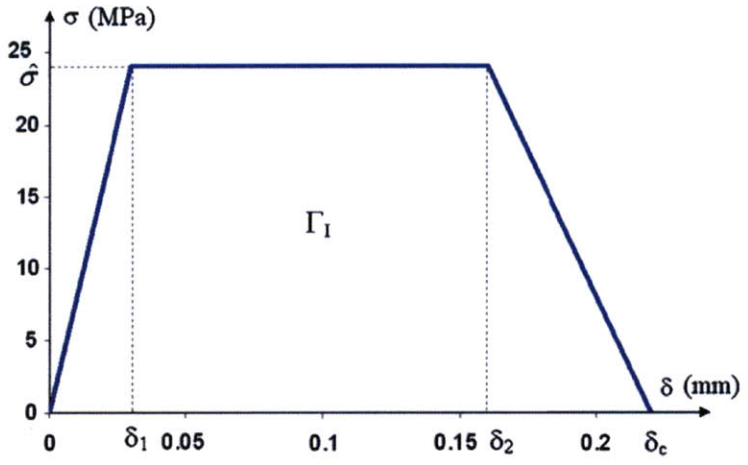

Figure A-15: Mode-1 traction-separation law for quasi-static fracture of adhesive [19]

Numerical Studies

Sun et al detail a methodology to determine mode-I cohesive parameters of a large range of loading rates in a follow-on paper [19]. Specifically, they use data from their companion paper to determine the cohesive parameters for the quasi-static crack growth and the dynamic crack growth, and they are able to use the results of wedge tests as independent verification. The following is a summary of this work [19].

The traction-separation law for the adhesive layer implemented in the numerical studies by Sun et al. is shown in Figure A-15. This model is derived from previous work completed by this same research group [20, 21]. The cohesive strength, the maximum tractions on the interface, is $\hat{\sigma}$ and the energy dissipated within the adhesive layer, the toughness of the joint, is Γ_1. The shape is to be a reasonable approximation of the elastic-plastic adhesive, with the initial slope established by the neat material testing described in the companion paper [18]. The cohesive strength and toughness were determined by comparing the numerical and experimental. Sun et al. complete a sensitivity analysis for each test geometry to ensure independent determination of each parameter.

Quasi-static fracture parameters

The 2-D finite element analysis of the DCB geometry was performed using ABAQUS/Standard and details are shown in Figure A-16. The adhesive is modeled with cohesive elements (UEL elements in ABAQUS). Sun et al. investigated different values of cohesive strength and toughness for the traction-separation law and compared the numerical results to the experimental data for the quasi-static crack growth seen in the DCB and found the geometry to be "relatively insensitive" to the cohesive strength. This can be seen in Figure A-17. Sun et al. also determined that they can not draw the conclusion that this relative insensitivity

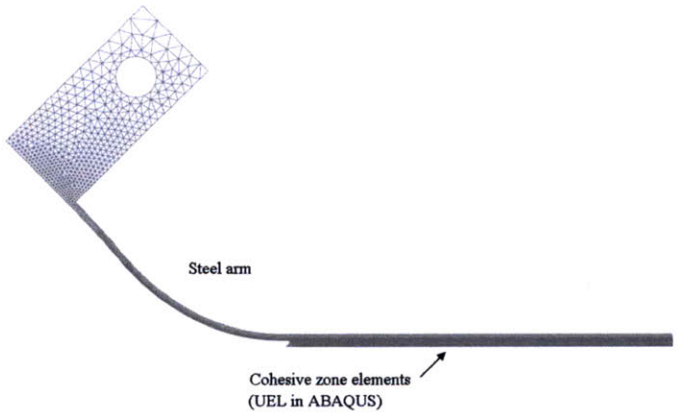

Figure A-16: Configuration of the DCB geometry used for the numerical simulations. [19]

to cohesive strength can be assumed to apply to all geometries, therefore more experiments are required.

Consequently, a geometry was designed numerically to be more sensitive to cohesive strength, as seen in Figure A-18. Tensile experiments were performed and a rate-independent maximum load was found. Cohesive-zone analysis was performed and a range of cohesive parameters that adequately fits the experiment were found and are shown in Figure A-17. In addition, the value of cohesive strength found from the tensile test shown in Figure A-18 was compared to the values of cohesive strength performed on the bulk material. Sun et al. found that the bulk material would have predicted a much larger cohesive strength than what was found in the tensile tests. The cohesive-zone model for the toughness and cohesive strength values shown in Figure A-17 were used to predict the crack length found in the DCB test for the quasi-static crack growth. This agreement can be seen in Figure A-19.

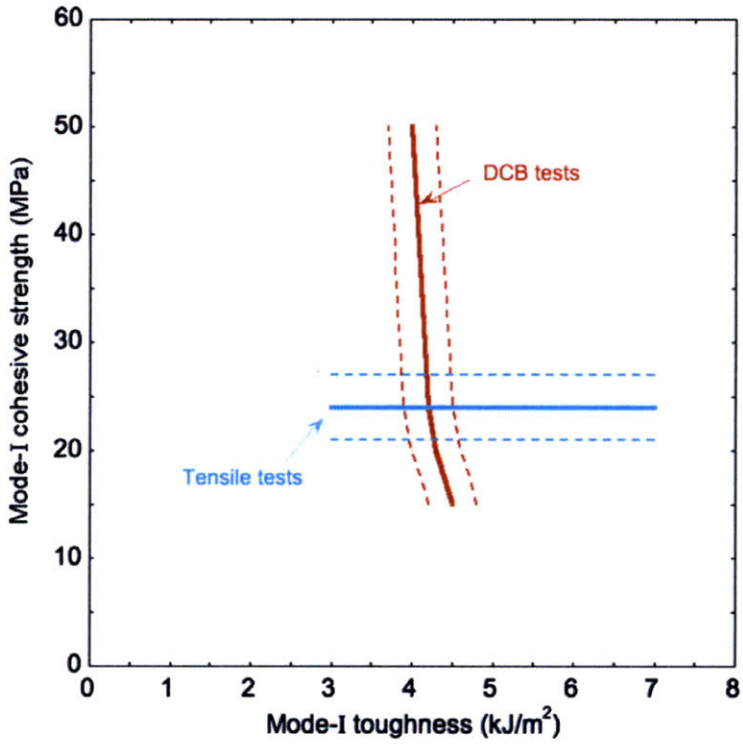

Figure A-17: A plot showing the ranges of values for the mode-1 toughness and normal cohesive strength values that give an acceptable agreement between the numerical and experimental results for the DCB geometry and tensile test geometry. [19]

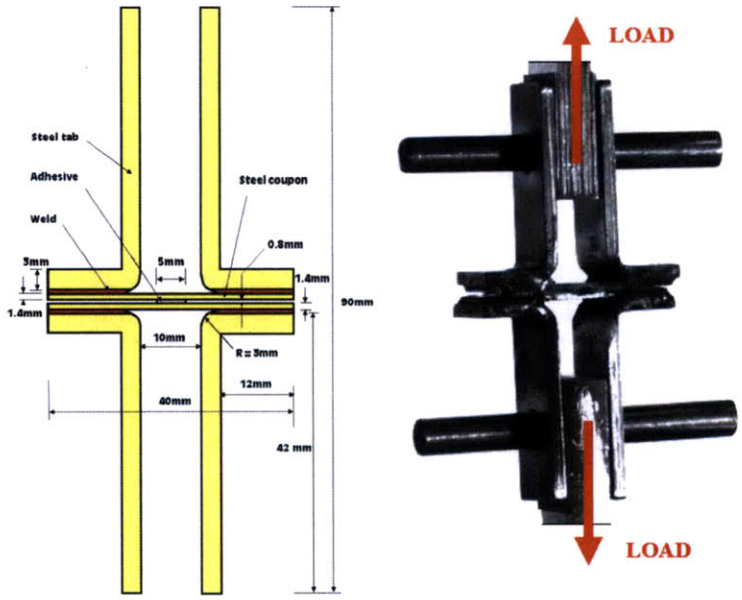

Figure A-18: Configuration of the tensile test specimen used to evaluate the cohesive strength of the adhesive system. [19]

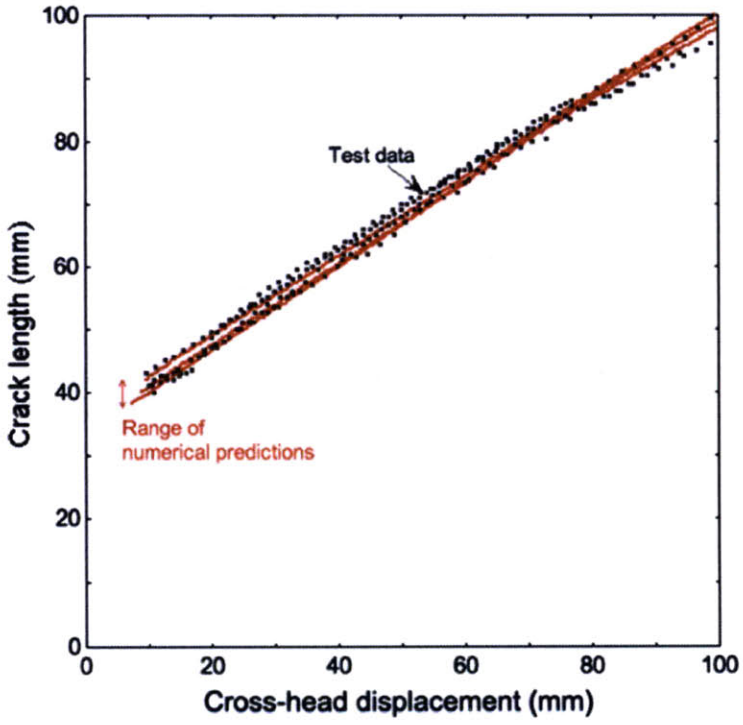

Figure A-19: Experimental crack length vs. crosshead displacement: fit of numerical data to test for the quasi-static crack growth of the DCB. [19]

Dynamic fracture parameters

Sun et al. modified the finite element model of the DCB geometries to contain two zones, a brittle cohesive zone and a tough cohesive zone, each with their own traction-separation law, shown in Figure A-20. The brittle cohesive zone was assumed to have the same cohesive strength as the tough cohesive zone, but to have unknown toughness. The toughness of the brittle elements was numerically determined by matching length of regions of dynamic crack growth to experiments.

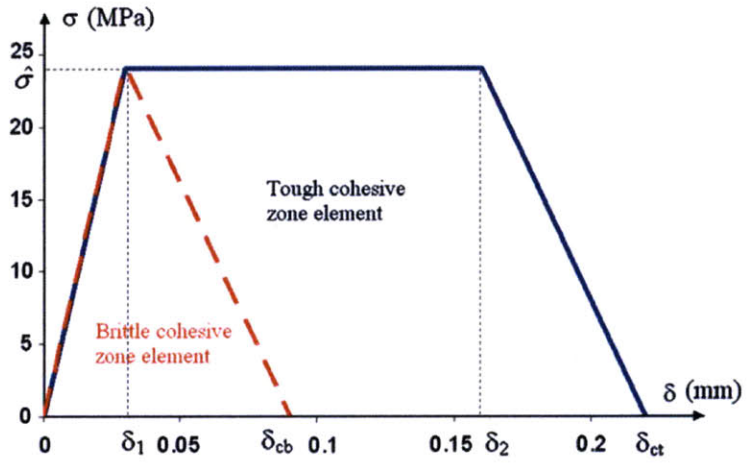

Figure A-20: A comparison between the two traction-separation laws used for quasi-static and dynamic fracture.[19]

Wedge tests

The independent numerical investigation was to take the determined cohesive parameters described above and try to predict the behavior seen in the wedge tests. Sun et al. were able to predict the steel arm curvature that was found experimentally as well as to determine the extension of the crack length ahead of the wedge.

Sun et al. Summary

In their two studies, Sun et al. make contributions to the determination of cohesive zone parameters of cohesive strength and toughness for a variety of loading rates numerically [19] and experimentally [18]. They were also able to apply the cohesive zone model for quasi-static crack growth, or toughened behavior, as well as modify their traction-separation model to take into account the stochastic behavior of the dynamic crack growth or brittle fracture.

A.2.3 Su, Wei, Anand: An elastic-plastic interface constitutive model: application to adhesive joints

Narrowing down on works directly influencing the current study, Su, Wei, and Anand present a continuum-level phenomenological interface constitutive model accounting for elastic and inelastic separation-slide deformations at the interface prior to failure of the adhesive bond in [5]. Su et al. successfully implement their constitutive theory with ABAQUS/Explicit by writing a USER INTERFACE subroutine. Using calibration experiments for an aluminum and polymeric adhesive system, they predict the load-displacement behavior of three types of validation experiments fairly well.

Constitutive model

The interface constitutive model laid out by Su et al. is briefly summarized below. They begin by denoting the displacement jump across the cohesive surface, $\boldsymbol{\delta}$, and the power-conjugate traction, $\mathbf{t}$, such that $\mathbf{t} \cdot \dot{\boldsymbol{\delta}}$ gives the power per unit area of the interface in the reference configuration. They assume the displacement jump can be additively decomposed into elastic and plastic parts, $\boldsymbol{\delta} = \boldsymbol{\delta}^e + \boldsymbol{\delta}^p$, and consequently, $\mathbf{t} \cdot \dot{\boldsymbol{\delta}} = \mathbf{t} \cdot \dot{\boldsymbol{\delta}}^e + \mathbf{t} \cdot \dot{\boldsymbol{\delta}}^p$. They define a free-energy per unit surface area in the reference configuration as φ, given by

$$\varphi = \hat{\varphi}(\boldsymbol{\delta}^e) = \frac{1}{2}\boldsymbol{\delta}^e \cdot \mathbf{K}\boldsymbol{\delta}^e, \tag{A.34}$$

where the interface elastic stiffness tensor is denoted $\mathbf{K}$. The power-conjugate traction is separated into normal and tangential parts, $\mathbf{t} = \mathbf{t}_N + \mathbf{t}_T$ and is equal to $\dfrac{\partial \hat{\varphi}(\boldsymbol{\delta}^e)}{\partial \boldsymbol{\delta}^e}$.

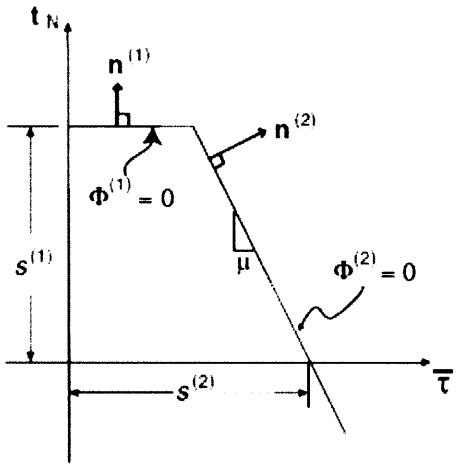

Figure A-21: Yield surfaces schematic for normal and shear mechanisms. [5]

Two yield surfaces, one normal, $\Phi^{(1)}$ and one shear, $\Phi^{(2)}$, are defined in Figure A-21. Here, the yield functions are equal to

$$\Phi^{(1)} = t_N - s^{(1)} \leq 0, \qquad \Phi^{(2)} = \bar{\tau} + \mu t_N - s^{(2)} \leq 0, \tag{A.35}$$

where the deformation resistance for the normal mechanism is $s^{(1)}$ and the deformation resistance for the shear mechanism is $s^{(2)}$. Also, the normal stress at the interface is defined as $t_N = |\mathbf{t}_N|$, the shear stress as $\bar{\tau} = |\mathbf{t}_T|$, and the coefficient of friction is denoted as μ. The outward unit normals to the two yield surfaces are:

$$\mathbf{n}^{(1)} = \frac{\partial \Phi^{(1)}}{\partial \mathbf{t}} = \mathbf{n}, \qquad \mathbf{n}^{(2)} = \frac{\partial \Phi^{(2)}}{\partial \mathbf{t}} = \frac{1}{\sqrt{1+\mu^2}}\left(\frac{\mathbf{t}_T}{\bar{\tau}} + \mu \mathbf{n}\right) \tag{A.36}$$

Su et al. take the flow rule to be equal to the sum of the contribution of each mechanism

$$\dot{\boldsymbol{\delta}}^p = \sum_{i=1}^{2} \nu^{(i)} \mathbf{m}^{(i)}, \qquad \nu^{(i)} \geq 0, \qquad \nu^{(i)} \Phi^{(i)} = 0, \quad \text{with} \tag{A.37}$$

$$\mathbf{m}^{(1)} = \mathbf{n}, \qquad \mathbf{m}^{(2)} = \frac{\mathbf{t}_T}{\bar{\tau}}. \tag{A.38}$$

The variable $s^{(i)}$ evolves according to Eq. A.39 with $h^{(ij)}$ representing the hardening/softening moduli.

$$\dot{s}^{(i)} = \sum_{j=1}^{2} h^{(ij)} \nu^{(j)}, \tag{A.39}$$

Additionally, the consistency condition of $\nu^{(i)} \dot{\Phi}^{(i)} = 0$ when $\Phi^{(i)} = 0$ with the above results serves to provide a system of linear equations for the determination of the inelastic deformation rates, $\nu^{(i)}$. Su et al. begin the delineation of their specific evolution equations with the definition of the equivalent relative plastic displacement of the individual mechanisms to be equal to $\gamma^{(i)} \stackrel{\text{def}}{=} \int_0^t \nu^{(i)}(\xi)\, d\xi$. An equivalent relative plastic displacement is then defined as

$$\bar{\gamma} \stackrel{\text{def}}{=} \sqrt{(\gamma^{(1)})^2 + \alpha\, (\gamma^{(2)})^2}, \tag{A.40}$$

where α represents a coupling parameter between the normal and shear mechanisms. Su et al. go on to define the functional form of strain hardening moduli in Eq. A.39 until a critical value of displacement jump, $\bar{\gamma}_c$. Once this critical equivalent displacement jump is reached, the softening response begins.

$$\dot{s}^{(i)} = \sum_{j=1}^{2} h^{(ij)} \nu^{(i)} = \begin{cases} h_0 \left(1 - \frac{s^{(i)}}{s^{*(i)}}\right)^{a^{(i)}} \dot{\bar{\gamma}} & \text{for } \bar{\gamma} \leq \bar{\gamma}_c \\ -h_{soft}^{(i)} \dot{\bar{\gamma}} & \text{for } \bar{\gamma}_c < \bar{\gamma} \leq \bar{\gamma}_{fail}, \end{cases}$$

The parameters of h_0, $s^{*(i)}$, $a^{(i)}$, h_{soft}, $\bar{\gamma}_c$, and $\bar{\gamma}_{fail}$ are all determined from calibration experiments of a butt joint in tension, a double shear specimen, and an L-shaped peel experiment to calibrate the strain softening response of the adhesive.

Implementation

The traction-separation results of the butt tension testing, the double-shear experiments, and the L-peel experiment are shown in Figure A-22. The results of the calibrated implemented constitutive model in ABAQUS/EXPLICIT through the USER SUBROUTINE are plotted along with the experimental results.

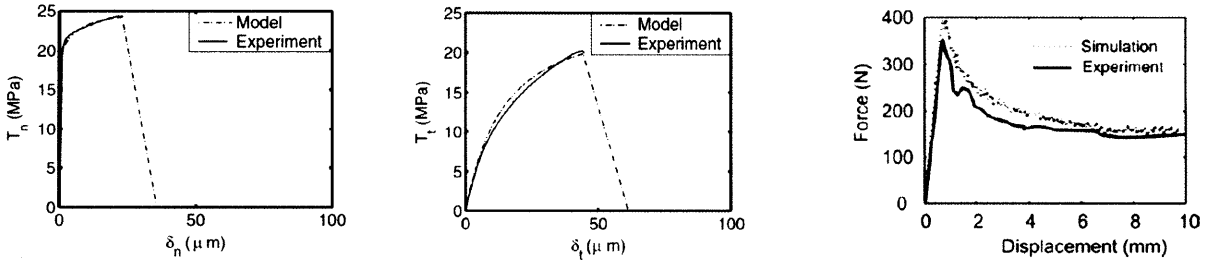

Figure A-22: Calibration Experiments (a) Traction-separation curve in the normal direction found from butt-joint specimen (b)Traction-separation curve in the shear direction found from double-lap shear specimen (c) Force versus displacement curve for the L-peel specimen [5]

Recall, the authors define an equivalent relative plastic displacement by Eq. A.40. From the calibration experimental results in Figures A-22 (a) and (b), the critical displacement jump in the normal mechanism is equal to 22 microns and the critical displacement jump in the shear mechanism is 44 microns. Su et al. set the critical equivalent displacement jump, $\bar{\gamma}_c$, equal to the smallest failure displacement jump of the interface in either direction, in this case 22 microns. Thus, the value of α, the coupling parameter, is calibrated to be 0.25. With a calibrated and implemented model, the geometry of other adhesive experiments can be predicted.

The experimental and simulation results for a T-peel experiment, a notched four point bend experiment, and a lap-shear experiment can be found in more detail in [5]. Su et al. are able to make good predictions of the experimentally measured load-displacement behavior of the adhesive for all three geometries. An example result for the T-Peel geometry is shown in Figure A-23.

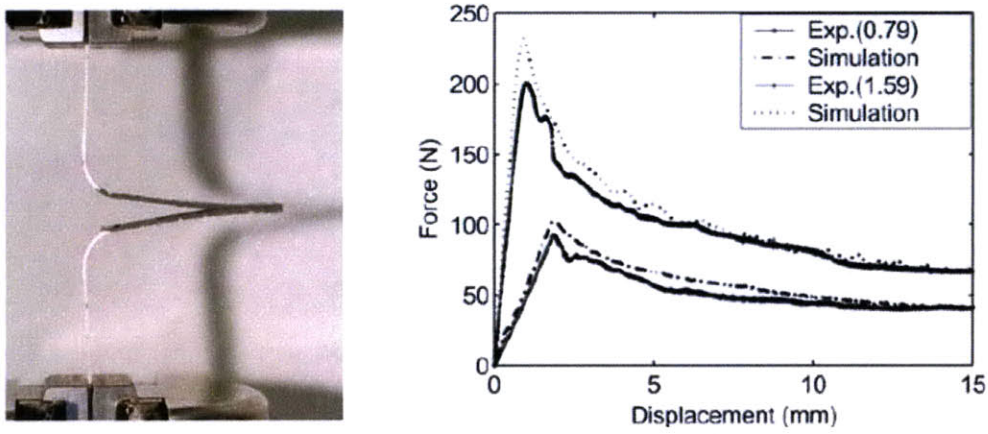

(a) (b)

Figure A-23: T-Peel Experiment (a)Photo of deformed experimental geometry and (b)Load-displacement curve for two different adherend thicknesses [5]

Su et al. Summary

Su et al. successfully implement their developed continuum-level phenomenological interface constitutive model accounting for elastic and inelastic separation-sliding deformation in an adhesive interface. They are able to calibrate their model with a set of experiments and are then able to predict fairly well the load-displacement behavior of the adhesive/adherend system when applied to three validation experiments. This work is unique in developing an interface constitutive model that allows for inelasticity in the adhesive prior to failure and that incorporates not only mode I, or normal separation of an adhesive, but also sliding, or shearing, of the interface in some form.

A.3 Appendix Summary

Three applications of the cohesive zone model used to capture inelastic deformation of the adhesive layer in an interface system have been described. Tvergaard and Hutchinson's work helps to distinguish important properties of the two governing parameters of the model: cohesive strength and fracture toughness [4]. The research of Sun et al. exemplifies some of the difficulties in designing test geometries that will allow for the independent determination of these cohesive parameters, as well as working to capture any rate effects an elastic-plastic adhesive system might have [18, 19]. Su et al. have worked to develop an interface constitutive model that allows for inelasticity at the interface prior to failure, as well as capturing mode-I and mode-II effects [5].

Bibliography

[1] G. I. Barenblatt. The formation of equilibrium cracks during brittle fracture: general ideas and hypotheses, axially symmetric cracks. *Applied Mathematics and Mechanics*, 23:622–636, 1959.

[2] D. S. Dugdale. Yielding of steel sheets containing slits. *Journal of the Mechanics and Physics of Solids*, 8:100–104, 1960.

[3] V. Tvergaard and J. W. Hutchinson. Toughness of an interface along a thin ductile layer joining elastic solids. *Philosophical Magazine A*, 70:641–656, 1994.

[4] V. Tvergaard and J. W. Hutchinson. On the toughness of ductile adhesive joints. *Journal of the Mechanics and Physics of Solids*, 44:789–800, 1996.

[5] C. Su, Y. J. Wei, and L. Anand. An elasti-plastic interface constitutive model: application to adhesive joints. *International Journal of Plasticity*, 20:2063–2081, 2004.

[6] Loctite Corporation, Loctite Aerospace. *Hysol Surface Preparation Guide.* Bay Point, CA.

[7] Standard guide for preparation of metal surfaces for adhesive bonding. *ASTM D 2651-01*, pages 1–6, 2008.

[8] Henkel Corporation, Aerospace Group. *Hysol®for (R) EA 9361: Epoxy Paste Adhesive.* Bay Point, CA.

[9] D. Mohr and M. Oswald. A new experimental technique for the multi-axial testing of advanced high strength steel sheets. *Experimental Mechanics*, 48:65–77, 2008.

[10] ABAQUS, Inc. *ABAQUS Reference Manuals.* Pawtucket, RI, 2006.

[11] Standard test method for mixed mode i-mode ii interlaminar fracture toughness of unidirectional fiber reinforced polymer matrix composites. *ASTM D 6671-06*, pages 1–13, 2006.

[12] A. T. Zehnder. *Lecture Notes on Fracture Mechanics.* Cornell University, Department of Theoretical and Applied Mechanics, 2008.

[13] J. W. Hutchinson. *A Course on Nonlinear Fracture Mechanics.* The Technical University of Denmark, Department of Solid Mechanics, 1979.

[14] N. Choupani. Mixed-mode cohesive fracture of adhesive joints: Experimental and numerical studies. *Engineering Fracture Mechanics*, 75:4363–4382, 2008.

[15] H. M. Westergaard. Bearing pressures and cracks. *Journal of Applied Mechanics*, 61: A49–A53, 1939.

[16] A. T. Zehnder and C. Y. Hui. A simple model relating crack growth resistance to fracture process parameters in elastic-plastic solids. *Scripta Materialia*, 42:1001–1005, 2000.

[17] V. Tvergaard and J. W. Hutchinson. The influence of plasticity on mixed mode interface toughness. *Journal of the Mechanics and Physics of Solids*, 41:1119–1135, 1993.

[18] C. Sun, M. D. Thouless, A. M. Waas, J. A. Schroeder, and P. D. Zavattieri. Ductile-brittle transitions in the fracture of plastically-deforming, adhesively-bonded structures. part i: Experimental studies. *International Journal of Solids and Structures*, 45:3059–3073, 2008.

[19] C. Sun, M. D. Thouless, A. M. Waas, J. A. Schroeder, and P. D. Zavattieri. Ductile-brittle transitions in the fracture of plastically-deforming, adhesively-bonded structures. part ii: Numerical studies. *International Journal of Solids and Structures*, 45:4725–4738, 2008.

[20] S. Li, M. D. Thouless, A. M. Waas, J. A. Schroeder, and P. D. Zavattieri. Use of mode-i cohesive-zone models to describe the fracture of an adhesively-bonded polymer-matrix composite. *Composites Science and Technology*, 65(2):281–293, 2005.

[21] Q. D. Yang, M. D. Thouless, and S. M. Ward. Numerical simulations of adhesively bonded beams failing with extensive plastic deformation. *Journal of the Mechanics and Physics of Solids*, 47:1337–1353, 1999.